Universidade do Minho
Escola de Engenharia

Nguyen Quoc Tuan

Effects of substituting ytterbium for scandium on the microstructure and properties of Al-Sc and Al-Mg-Sc alloys

Outubro de 2014

Universidade do Minho
Escola de Engenharia

Nguyen Quoc Tuan

Effects of substituting ytterbium for scandium on the microstructure and properties of Al-Sc and Al-Mg-Sc alloys

Tese de Doutoramento
Programa Doutoral em Engenharia de Materiais

Trabalho efectuado sob a orientação da
Professora Ana Maria Pires Pinto

e co-orientação do
Professor Luís Augusto Marques Sousa Rocha

Outubro de 2014

STATEMENT OF INTEGRITY

I hereby declare having conducted my thesis with integrity. I confirm that I have not used plagiarism or any form of falsification of results in the process of the thesis elaboration.

I further declare that I have fully acknowledged the Code of Ethical Conduct of the University of Minho.

University of Minho, Guimarães, 29th October 2014

Full name: Nguyen Quoc Tuan

Signature: _____

Acknowledgments

This research have been carried out during my Ph.D program at Centre for Mechanical and Materials Technologies (CT2M), Department of Mechanical Engineering, University of Minho, Guimaraes, Portugal. There are many people who I would like to thank for their assistance in this thesis research. First and foremost, I would like to express my sincere gratitude and warm regards to my advisors Prof. Ana Maria Pinto and Prof. Luis Rocha for giving me opportunity to complete the Ph.D degree at their laboratory. Their important and helpful advice, support and guidance allowed me to learn a lot from their great scientific skills.

Special thanks to Prof. Joaquim Barbosa and Dr. Hélder Puga for their advices during my research and their support in casting experiment. I am grateful to Dr. Fatih Toptan and Alexandra Alves for their assistance during corrosion study. Many thanks to Dr. Edith Ariza for the assistance in SEM analysis and Miguel Abreu for the assistance in heat treatment experiment. I am also thankful to Prof. Augusto Lopes (University of Aveiro) for help me in TEM analysis. I would like to thank other colleagues, staff, and friend for their friendship, useful discussions and supports during the time I studying and living here.

I would like to express my warmly grateful to my family, my parents, and my girlfriend for their love, support, encouragement, and always standing by me during my Ph.D work.

Finally, this research would not have been performed without the support of the BRIDGING THE GAP Erasmus Mundus project funded by the European Commission program Erasmus Mundus External Cooperation Windows - Lot 12.

BRIDGINGtheGAP

Erasmus Mundus External Cooperation Window For Lot 12

EMECW L12 MOBILITY GRANT AWARD CONTRACT BTG_575

Grant agreement n 2009/1661-001 001ECW

Abstract

Effects of substituting ytterbium for scandium on the microstructure and properties of Al-Sc and Al-Mg-Sc alloys

Aluminium alloys are widely applied in aircraft, automobile, marine and other engineering structures. The reason for this large application is due to a wide range of properties including low density, corrosion resistance and high strength to weight ratio.

Al(Sc) alloys represent a new class of potential alloys for high performance structural applications. The superior mechanical properties of these alloys are due to the formation of a high density of elastically-hard Al_3Sc ($L1_2$ structure) precipitates which remain fully coherent with the α–Al matrix at elevated temperatures leading the Sc–containing Al alloys a good mechanical strength, hot cracking resistance and weld strength.

The excellent properties obtained from the combination of solid-solution hardening and precipitation hardening in Al–Mg–Sc alloys make these alloys very attractive to automotive, aerospace, and structural applications. However, the Sc high cost limits the applications and the addition of cheaper alloying elements that substitutes partially Sc are not only desirable but crucial.

In order to reduce the cost of Sc–containing Al alloys and maintain their mechanical properties, the microstructure and mechanical properties of Al–Sc–Yb and Al–Mg–Sc–Yb alloys in comparison with Al–Sc and Al–Mg–Sc alloys were studied. The aging behaviour, precipitate morphologies, precipitate coarsening, precipitation hardening and corrosion behaviour of these alloys were investigated.

Transmission electron microscopy (TEM) and high-resolution TEM were used to understand the precipitation evolution. The results showed the similarity of microstructure, hardness and aging behaviour of Al–0.24Sc–0.07Yb alloy in comparison with Al–0.28Sc alloy and Al–4 wt% Mg–0.3 wt% Sc alloy with Al–4 wt% Mg–0.24 wt% Sc–0.06 wt% Yb alloy. The approximately spheroidal Al_3Sc and $Al_3(Sc,Yb)$ precipitates were uniformly distributed throughout the α–Al matrix. The precipitates remain fully coherent with α–Al matrix even after aging at high temperature for long time.

In another aspect, the grain refinement in Al–Mg–Sc alloys with and without ultrasonic treatment at various pouring temperatures was investigated and understood. The average grain size of Al–Mg–Sc alloy remarkably decreases by increasing the content of Mg or by adding 0.3 wt% of Sc. The pouring temperature has a strong effect on the microstructure of Al–1Mg–0.3Sc alloy. Lower pouring temperature leads to smaller grain size and more homogeneous microstructure. Ultrasonic vibration proved to be a

potential grain refinement technique of Al–1Mg–0.3Sc. Significant grain refinement was obtained by applying ultrasonic treatment within the temperature range from 700 to 740 °C.

The corrosion behaviour of Al–Sc, Al–Sc–Yb, Al–Mg, Al–Mg–Sc and Al–Mg–Sc–Yb alloys in 3.5 wt% of NaCl solution was investigated by immersion and potentiodynamic polarisation analysis in order to understand the effect of Sc, Yb, and heat treatment on the localized corrosion and electrochemical behaviour. The presence of Fe–containing intermetallic phases promote the pitting corrosion. Yb has strong effect on the polarization behaviour of Al–Sc alloys. The addition of Yb decreases the corrosion tendency and improves the pitting corrosion resistance of Al–Sc alloy. The presence of a high density of fully coherent nano–sized Al_3Sc or $Al_3(Sc,Yb)$ precipitates in heat treated alloy enhances the passivity of these alloys. The addition of Sc and Yb to Al–4Mg alloy decrease the susceptibility to corrosion of the heat treated alloys. More stable passive plateau and less susceptibility to pitting corrosion was observed in the polarization curves of Al–4Mg–0.3Sc and Al–4Mg–0.24Sc–0.06Yb alloys after heat treatment.

Resumo

Efeito da substituição parcial do escândio por itérbio na microestrutura e propriedades de ligas Al-Sc e Al-Mg-Sc

A baixa densidade, elevada resistência à corrosão e a elevada resistência específica são algumas das propriedades que suportam a utilização das ligas de alumínio em todas as áreas industriais, com particular destaque para a indústria dos transportes.

As ligas de alumínio com adição de escândio apresentam um elevado potencial para aplicações estruturais de elevados desempenho. As excelentes propriedades destas ligas resultam da precipitação de nanopartículas Al_3Sc finamente dispersas na matriz e que se mantêm coerentes com a matriz até temperaturas relativamente elevadas.

O efeito combinado do endurecimento por solução sólida e por precipitação, resultante da adição de Sc às ligas Al-Mg alarga o campo da aplicação destas ligas, nomeadamente à indústria dos transportes. No entanto o elevado custo do escândio tem limitado a aplicação destas ligas, pelo que a substituição parcial Sc por outros elementos de liga de menor custo é crucial para o desenvolvimento destes materiais.

Tendo em vista a redução do custo das ligas com Sc, mas mantendo o mesmo nível de propriedades, o presente trabalho incidiu no estudo do efeito da substituição parcial do Sc pelo Yb em ligas Al–Sc e Al–Mg–Sc.

Assim foi feito um estudo comparativo entre ligas Al–Sc e Al–Mg–Sc, com ligas Al–Sc–Yb e Al–Mg–Sc–Yb respetivamente, nomeadamente no que diz respeito à cinética de envelhecimento, tamanho, natureza e distribuição dos precipitados, cinética de coalescimento dos precipitados bem como no grau de endurecimento por precipitação e na resistência à corrosão das ligas.

A evolução da microestrutura resultante de diferentes condições de envelhecimento foi avaliada através de Microscopia Eletrónica de Transmissão (TEM) e Microscopia Eletrónica de Transmissão de Alta Resolução e o grau de endurecimento foi avaliado através de ensaios de dureza Vickers. Os resultados mostram que a substituição parcial de Sc por Yb não induz alterações significativas no comportamento das ligas. Comparando as ligas Al–0.28Sc e Al–0.24Sc–0.07Yb por um lado e as ligas Al–4Mg–0.3Sc e Al–4Mg–0.24Sc–0.06Yb por outro verifica-se uma grande semelhança tanto a nível de microestrutura como de dureza e cinética de envelhecimento. O endurecimento resulta formação de precipitados Al_3Sc e $Al_3(Sc,Yb)$ coerentes, fina e uniformemente dispersos na matriz α–Al. Os precipitados mantêm a coerência com a matriz mesmo após envelhecimento prolongado a temperaturas elevadas.

Neste trabalho foi ainda estudado o efeito do tratamento por ultra-sons na estrutura de vazamento. Os

resultados mostram que os ultra-sons originam uma afinação significativa do grão. Verificou-se também que com o aumento do teor em Mg, a adição de Sc e a diminuição da temperatura de vazamento têm um efeito significativo na estrutura de vazamento.

O comportamento à corrosão das ligas Al–Sc, Al–Sc–Yb, Al–Mg, Al–Mg–Sc and Al–Mg–Sc–Yb numa solução de NaCl (3.5% wt.) foi estudado através de ensaios de imersão e de polarização potenciodinâmica, tendo sido avaliado o efeito da adição de Sc e Yb bem como do tratamento térmico no comportamento eletroquímico e corrosão localizada. A presença de fases intermetálicas ricas em Fe promove a corrosão por picada. A adição de Yb às ligas de Al-Sc diminui a tendência para a corrosão e melhora a resistência à corrosão por picada. A elevada presença de nano-precipitados coerentes de Al_3Sc ou $Al_3(Sc,Yb)$ na liga tratada termicamente promove a passivação dessas ligas. A adição de Sc e Yb à liga Al–4Mg envelhecida diminui a suscetibilidade à corrosão nas ligas Al–4Mg–0.3Sc e Al–4Mg–0.24Sc–0.006Yb. Nas curvas de polarização potenciodinâmicas das ligas Al–4Mg–0.3Sc e Al–4Mg–0.24Sc–0.06Yb foi observado um patamar de passivação mais estável e uma menor suscetibilidade à corrosão por picada após o tratamento térmico das ligas.

Table of Contents

List of Symbols and Acronyms

FCC	Face-center cubic
REMs	Rare-earth metals
TEM	Transmission electron microscopy
HRTEM	High resolution transmission electron microscopy
SEM	Scanning electron microscopy
EDS	Energy dispersive spectrometer
APT	Atom-probe tomography
LSW theory	Lifshitz-Slyozov-Wagner theory
APB	Anti-phase-boundary energy
WR/A	Warm rolled and aged
WR/CR/A	Warm rolled/cold rolled and aged
ECAP	Equal channel angular pressing
Ep	Pitting potential
GRF	Growth-restricting factor GRF
Epp	Protection potential
SCE	Saturated calomel electrode
OCP	Open circuit potential
FFT	Fast Fourier transform
PSDs	Precipitates size distributions
$< \boldsymbol{R(t)} >$	Average precipitate radius at the onset of quasi-stationary coarsening at time t
$< \boldsymbol{R(t_0)} >$	Average precipitate radius at the onset of quasi-stationary coarsening at time t_0
$\boldsymbol{K_{KV}}$	Coarsening rate constants for $< R(t) >$
$\Delta \boldsymbol{C_i^{\alpha}(t)}$	Denotes supersaturation that is the difference between the concentration of i^{th} component in the matrix
$< \boldsymbol{C_i^{\alpha}(t)} >$	Composition of the i^{th} component in the matrix
$< \boldsymbol{C_i^{\alpha}(t \to \infty)} >$	Solid-solubility of the i^{th} component in the matrix
$\boldsymbol{K_{i,KV}^{\alpha}}$	Coarsening rate constants for $\Delta C_i^{\alpha}(t)$
$\mathbf{N_v(t)}$	Precipitate density at the onset of quasi-stationary coarsening at time t
$\mathbf{N_v(t_0)}$	Precipitate density at the onset of quasi-stationary coarsening at time t_0
$\boldsymbol{V_v}$	Equilibrium volume fraction of precipitates
$\boldsymbol{\alpha}$	The matrix phases

$\mathbf{B}$	The precipitate phases
$\mathbf{V_m}$	Molar volume of the precipitate
$\mathbf{\Sigma}$	Isotropic interfacial free energy
$\mathbf{R}$	The ideal gas constant
$\mathbf{D_i}$	The diffusion coefficient of the i^{th} component
C_i^{β}	The composition of the i^{th} component in the precipitate phase.
$\mathbf{k_i}$	The distribution coefficient of the i^{th} species between the matrix and precipitate phases that is defined by C_i^{β}/C_i^{α}
$\mathbf{k_{exp}}$	The experimentally determined coarsening rate constant
$\mathbf{L}$	The relative contribution of the elastic strain and interfacial energies
$\mathbf{E}$	Precipitate–matrix lattice parameter mismatch
$\mathbf{C_{44}}$	Elastic constant of the matrix
$\mathbf{L}$	Precipitate size

List of Figures

List of Tables

CHAPTER 1 – STATE OF THE ART

Chapter 1 – State of the art

1.1 Motivation for Research

Aluminium alloys are widely applied in aircraft, automobile and other engineering structures. The reason for this large application is due to a wide range of excellent properties including low density, corrosion resistance and high strength to weight ratio. Some aluminium alloys are commonly used in aircraft and other aerospace structures: 7075, 6061, 6063, 2024, 5052 aluminium alloys. Al-Li alloys are used in space shuttle super lightweight external tank and Al-Cu alloys are used in the original space shuttle standard weight external tank as 2195, 2219 aluminium alloys. In Marine application, aluminium alloys are used for boat building and shipbuilding, and other marine and salt-water sensitive shore applications. They are 5052, 5059, 5083, 5086, 6061, 6063 aluminium alloys. In cycling frames and components, 2014, 6063, 7005, 7075 and scandium aluminium alloys were applied. 6111 aluminium alloy is extensively used for automotive body panels.

Al–Sc alloys have excellent mechanical properties at ambient and elevated temperatures due to the presence of a high density (as high as 10^{22} m^{-3}) of elastically-hard Al_3Sc ($L1_2$ structure) precipitates [1-5], which remain coherent with the α-Al matrix at elevated temperatures [1,3]. On a per-atom basis, Sc has the greatest strengthening effect of any existing alloying addition to Al [6]. The Al_3Sc precipitates coarsen slowly up to ~300°C, imparting good creep resistance in coarse-grained cast alloys [1-3,5,7-11]. The lattice parameter mismatch of Al and Al_3Sc also contributes to the high creep resistance of Al–Sc alloys. The good interfacial strength between the Al_3Sc precipitates and the aluminium matrix creates a significant lattice strain, which blocks dislocation motion and prevents grain growth [12]. Furthermore, the thermal stability of the Al_3Sc precipitates suppresses recrystallization [13,14] and leads to a significant strengthening effect. In general, large aluminium alloy weldments are susceptible to hot cracking. However, the dispersion of thermally stable Al_3Sc precipitates suppresses thermal cracking in the heat affected zone of the weldment [15-17]. Therefore Al-Sc alloys are widely used in the fabrication of sports equipment, aerospace components and in a range of structural applications.

Although Al–Sc alloys are very attractive field but they are limited by the cost and availability of Sc. The price of Al–2 wt% Sc master alloy is 512 $/kg. A possible solution for this problem is solid solution strengthening to substitute alloying additions that are similar in nature to Sc to reduce the Sc content without decreasing of properties. Some previous researches showed that ternary additions to Al–Sc alloys

improve mechanical properties by solid solution strengthening as in the case of Mg [18-22], or by substituting for Sc in Al_3Sc precipitates as in the cases of Ti and Zr [13-26]. Ti and Zr diffuse significantly more slowly than Sc in Al [27-29] and decrease the lattice parameter mismatch between the α–Al matrix and the precipitates [30]. While both of these attributes increase coarsening resistance, the latter may decrease creep resistance by reducing elastic interactions with dislocations during climb bypass [23,24,31]. The ideal ternary additions for Al–Sc alloys should thus exhibit high solubility in Al_3Sc and low diffusivity in α–Al (like Ti and Zr), while moderately increasing the lattice parameter of Al_3Sc (unlike Ti and Zr) [32]. The rare-earth metals (REMs) are attractive ternary additions to substitute Sc.

In this research, based on Al–0.28Sc and Al–4 wt% Mg-0.3 wt% Sc alloys, we studied dilution Al–Sc and Al–Mg-Sc alloys with microalloying additions of Yb. The effects of substituting Yb for Sc on the microstructure and the mechanical properties of Al–Sc alloy are investigated by using SEM, TEM, HRTEM and Vickers hardness. The precipitate evolution and precipitation hardening were understood.

In the aluminium casting industry grain refinement plays an important role to enhance mechanical properties as toughness, fracture resistance, fatigue strength and isotropic behaviour of the cast alloys. Grain refinement also reduces hot tearing, porosity and the pore size [33,34]. Several processes have been applied to achieve a fine, equiaxed and uniform grain microstructure. In this work, the role of Mg and Sc as well as the influence of pouring temperature on grain refinement of Al–1 wt% Mg–0.3 wt% Sc was studied. Moreover, the microstructures of Al–1 wt% Mg–0.3 wt% Sc alloy at various pouring temperatures without and with ultrasonic treatment were studied. The mechanism of grain refinement was proposed and understood. The age hardening behaviour of those alloys without and with ultrasonic treatment was investigated.

Almost researchers focused in microstructural and mechanical properties of these alloys. However, a limited work about corrosion behaviour has been studied. We have known that the chemical and mechanical characteristics have considerable influences on the passivity of Al alloys, resulting in the different corrosion behaviour. The existence of second phase in the alloy matrix also effects on the corrosion behaviour [35,36]. The corrosion resistant property of these alloys is very important property for application in shipbuilding and marine industry. In this research, the corrosion behaviour of these alloys will be studied to evaluation the capability for these alloys to apply in seawater environment.

1.2 Literature Review

1.2.1 Al–Sc and Al–Mg–Sc alloys

1.2.1.1 The binary Al–Sc system and Al_3Sc phase

The binary Al–Sc phase diagram on the Al rich side is shown in Figure 1.1 which indicates the limited solubility of Sc in α–Al below the eutectic temperature [37,38]. The maximum solid solubility of Sc in α–Al is 0.38 wt% that occurs at the eutectic temperature of 660 ◦C as the following reaction:

$$Liq. = \alpha(Al) + Al_3Sc \qquad (1.1)$$

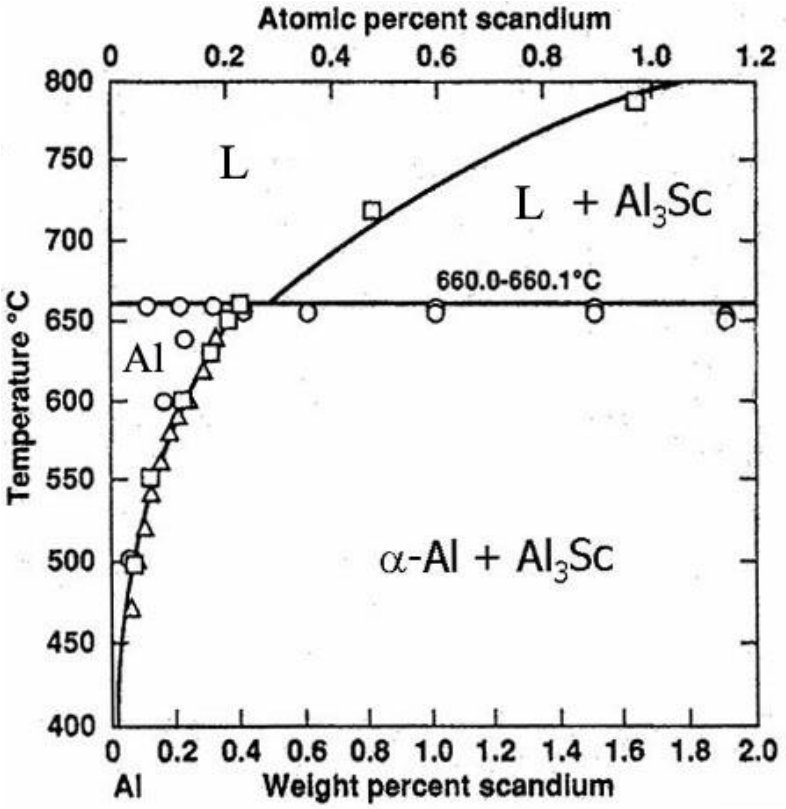

Figure 1.1. Al–Sc phase diagram on the Al rich side [37].

The solid solubility of Sc in α–Al drops sharply below 0.1 wt% at 500 ◦C. The solid solubility of Sc in α–Al at various temperatures can be determined from Figure 1.2 [5,39]. However, the high supersaturated solid solution of Al–Sc alloy can be obtained by high cooling rate during solidification process. The supersaturated solid solutions of 0.6 wt% Sc in α–Al was achieved at the cooling rate of 100 ◦C [2], and the supersaturation in excess of 5 wt% Sc was obtained by quenching the melt with a rotating mill device [40]. The Al–Sc supersaturated solid solution decomposes into fine coherent Al_3Sc precipitates with an ordered

$L1_2$ structure [41]. At ambient temperature the lattice parameters of α–Al and Al_3Sc are 0.40496 and 0.4105 nm, respectively [30, 42]. The lattice parameter mismatch is defined by following equation:

$$\delta = 2\frac{a_{Al_3Sc} - a_{Al}}{a_{Al} + a_{Al_3Sc}} \qquad (1.2)$$

where a_{Al_3Sc} and a_{Al} are lattice parameter at room temperature of Al_3Sc and α–Al.

The lattice parameter mismatch of α–Al matrix phase and Al_3Sc precipitate phase at room temperature are calculated and shows the value of 1.35 %. While at 300°C, this mismatch decreases to about 1.1% due to thermal expansion [43]. The crystallography of Al_3Sc was reported in similarity with Cu_3Au, Ni_3Al and Ni_3Fe lattice structure. This lattice structure is ordered LI_2 structure and space group Pm3m [41]. The atomic arrangement in Al_3Sc is shown in Figure 1.3. This structure is ordered face-center cubic (FCC), but in fact the Al_3Sc lattice structure is simple cubic lattice that contains one Sc and three Al atoms.

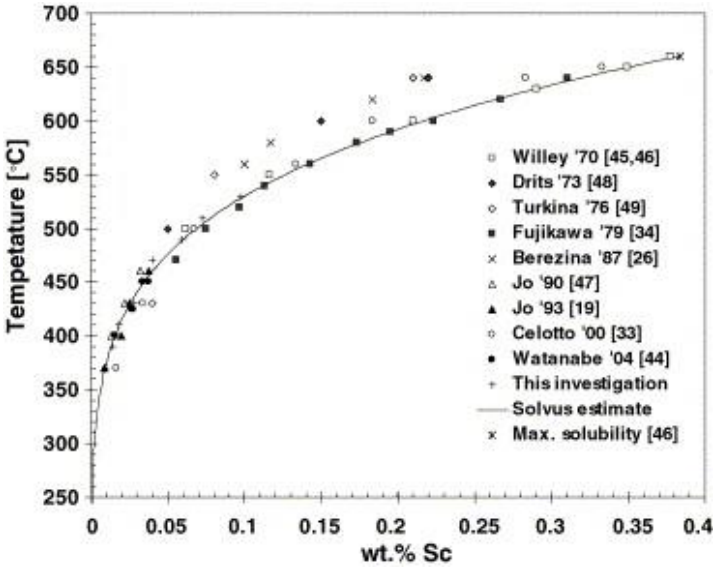

Figure 1.2. The solvus line of Sc in Al [5,39].

The diffraction patterns of Al_3Sc precipitates are almost similar to that of FCC materials. But one characteristic for diffraction patterns of Al_3Sc precipitates was noted. The reflections such as {100}, {010}, and {110} reflections which are invisible in an FCC material will be appeared in a diffraction pattern of Al_3Sc precipitate. The diffraction pattern taken along the [001] axis of Al_3Sc precipitates in Al–Sc alloy is shown in Figure 1.4 [7]. The {100} and {010} reflections of Al_3Sc precipitates and the {200} and {020} reflections of the α–Al matrix were observed.

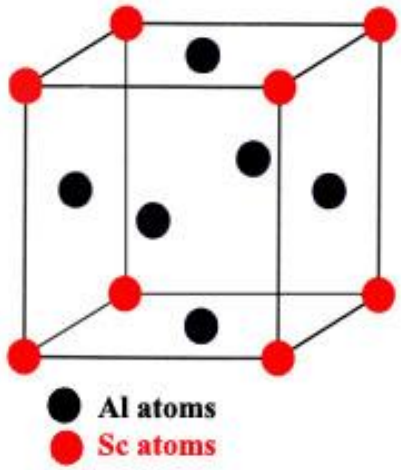

Figure 1.3. Atomic arrangement of the Al_3Sc phase.

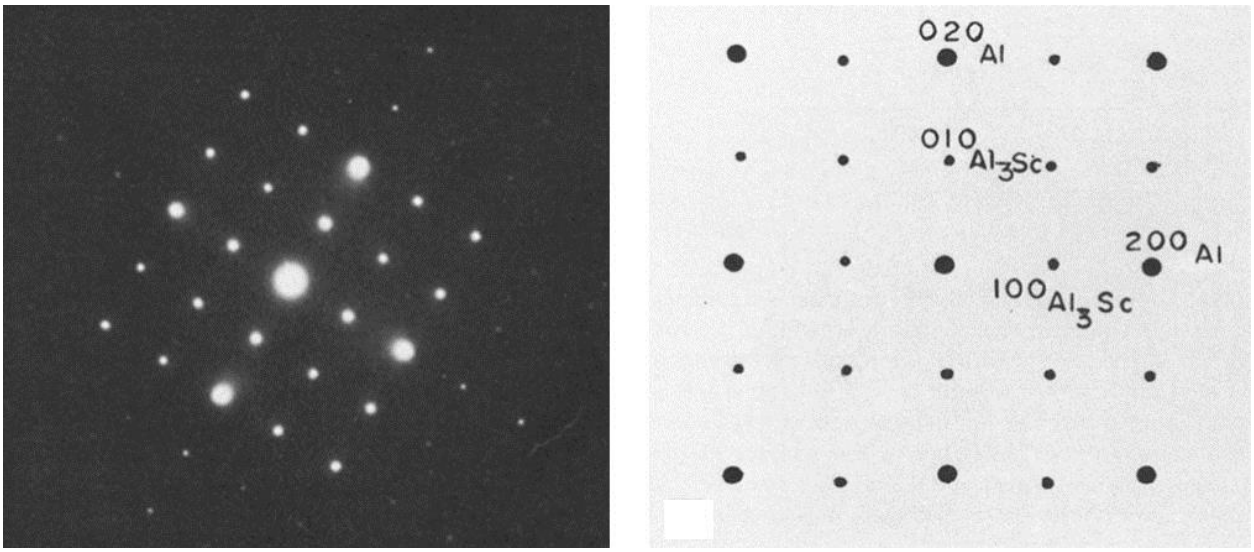

Figure 1.4. The [001] diffraction pattern of Al_3Sc precipitates in Al–Sc alloy [7].

The Al_3Sc phase can be formed in Al–Sc alloys through possible four ways:

1) Al_3Sc is the first phase forming in the hypereutectic Al–Sc alloys during solidification. According to the Al–Sc binary phase diagram in Figure 1.1, with the Al–Sc alloys contain Sc higher than the eutectic composition (0.55 wt%), the Al_3Sc phase will be formed in the melt and exists as second phase particles in the α–Al matrix during solidification [44,45]. The morphology and the nucleation mechanism of Al_3Sc in the Al–0.7 wt% Sc alloy casted at various cooling rate was studied by Hyde *et al.* [45,46]. This result showed that the Al_3Sc particles were heterogeneously nucleated on oxides within the melt. The morphology of Al_3Sc particles exhibit the faceted cubic shape at slow cooling rate (~1 K s^{-1}), and become unstable along the

cube edges and corners, forming growth perturbations. The overall shape is cubic morphology with cellular-dendritic sub-structures.

2) According to reaction (1.1), Al_3Sc phase can be formed by the eutectic formation in hypo- and hypereutectic Al–Sc alloys. Hyde *et al.* [45,46] suggested that the eutectic Al_3Sc could be formed in the Al–0.7 wt% Sc alloy during solidification.

3) Al_3Sc phase can be formed by discontinuously precipitation from supersaturated solid solution. In this way, the supersaturated solid solution of Sc in α–Al decomposes into α–Al and Al_3Sc at a moving grain boundary. The driving force for the grain boundary migration is the volume free energy that is released during the precipitation. According to Norman *et al.* [44] and Blake *et al.* [7], the grain boundaries migrated during cooling, and left a fan shaped array of precipitates behind the moving grain boundaries. The morphology of coherent rod-like precipitates was observed.

4) Al_3Sc phase can be formed by continuously precipitation (nucleation and growth) from supersaturated solid solution. Continuous precipitation of Al_3Sc occurs during the isothermal treatment of as-cast alloy with supersaturated solid solution of Sc in α–Al. This process includes three stages: nucleation, growth and coarsening stage of Al_3Sc precipitates. The homogeneous nucleation and diffusion controlled growth is main mechanism of continuous precipitation [10,11,47]. Some investigations reported the heterogeneous nucleation of Al_3Sc precipitates on dislocation [3,11,13] and grain boundaries [4,11,13,48]. In the continuous precipitation, the morphology of Al_3Sc precipitates is almost spherical [41,49-52]. There are some investigations showed the different morphology. The Al_3Sc precipitates with spherical, cuboidal, and/or cauliflower shape were indicated in Riddle *et al.* [53] and Novotny *et al.* [11]. The Al_3Sc precipitate with large oblong morphology was observed in Al–0.06 at. % Sc aged at 400 °C for 24 h. According to Marquis *et al.* [3] the morphology of Al_3Sc consists of 6 {100} (cube), 12 {110} (rhombic dodecahedron), and 8 {111} (octahedron) facets, that corresponds to a Great Rhombicuboctahedron. The Figure 1.5 and 1.6 show the HRTEM image taken along the [100] zone axis of an Al_3Sc precipitate obtained by aging Al–0.3 wt% Sc at 300°C for 350 h and the Great Rhombicuboctahedron morphology with various projections.

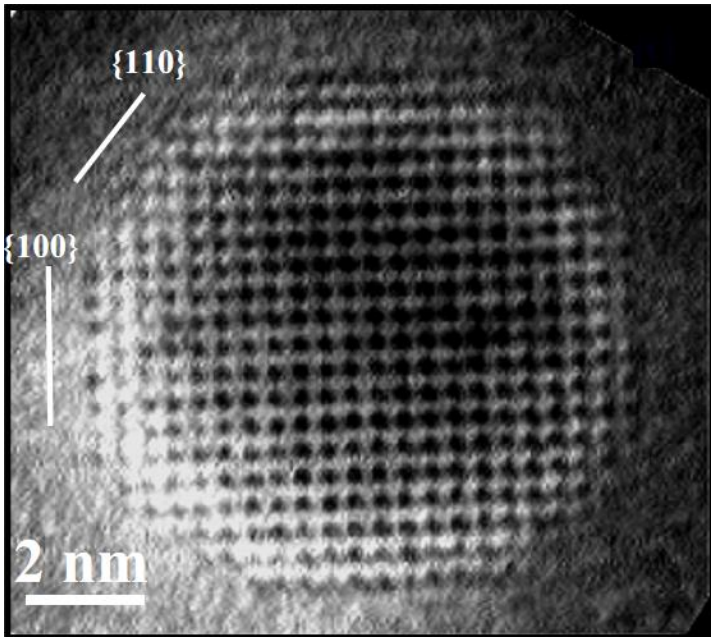

Figure 1.5. HRTEM image taken along the [100] zone axis of an Al_3Sc precipitate in Al–0.3 wt% Sc alloy aged at 300°C for 350 h [3].

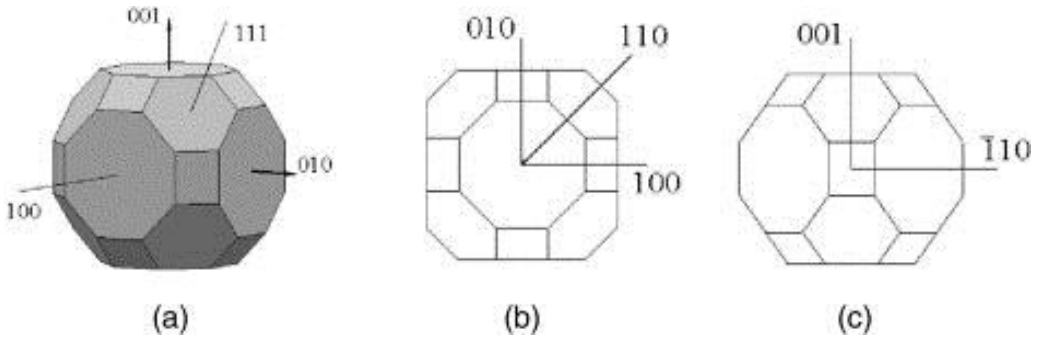

Figure 1.6. Great Rhombicuboctahedron morphology: (a) three dimensional precipitate; (b) [100] projection; and (c) [110] projection [3].

1.2.1.2 The Al–Mg–Sc system

Aluminum alloys with magnesium as a main alloying element are widely used in industry as non-aging, ductile, medium-strength, weldable, and corrosion-resistant materials [54]. However, their relatively low strength characteristics hinder their use as structural materials in ship building and the aerospace industry. Alloying with scandium is the a excellent way to solve these problems [2]. Some previous researches indicated that the strength of Al–Mg alloys can be substantially improved by the addition of small amount of scandium due to the presence of elastically hard, coherent and nano–sized Al_3Sc ($L1_2$) particles, which strongly inhibit the dynamic recrystallization and dislocation movement [55-61].

In the Al-Mg-Sc ternary system, the mutual solid solubilities of Mg and Sc are decreased with the decrease of temperature. The solid solubility of Mg in Al at various temperatures is shown in Table 1.1.

Table 1.1. Solid solubility of Mg in Al [2]

t, °C	450	427	400	377	350	327	300	277	177	127	100
wt%	17.4	15.3	13.5	11.5	9.9	8.1	6.7	5.5	2.6	2.0	1.9
at%	18.5	16.4	-	12.5	-	9.0	-	6.4	3.3	2.7	2.3

The maximum solid solubility of Mg in Al is 17.4 wt% (18.5 at%) at 450 °C in a binary Al-Mg alloy and it decreases to 10.5 wt% (11.6 at%) with 0.007 at% Sc at 447 °C [2]. The mutual solubility of Mg and Sc in Al at 430 °C is 10.5 wt% (11.6 at%) and 0.01 wt% (0.006 at%) respectively. Turkina and Kuzmina [62] and Pisch *et al.* [63] calculated the solid-solubility of Sc and Mg that is shown in Figure 1.7.

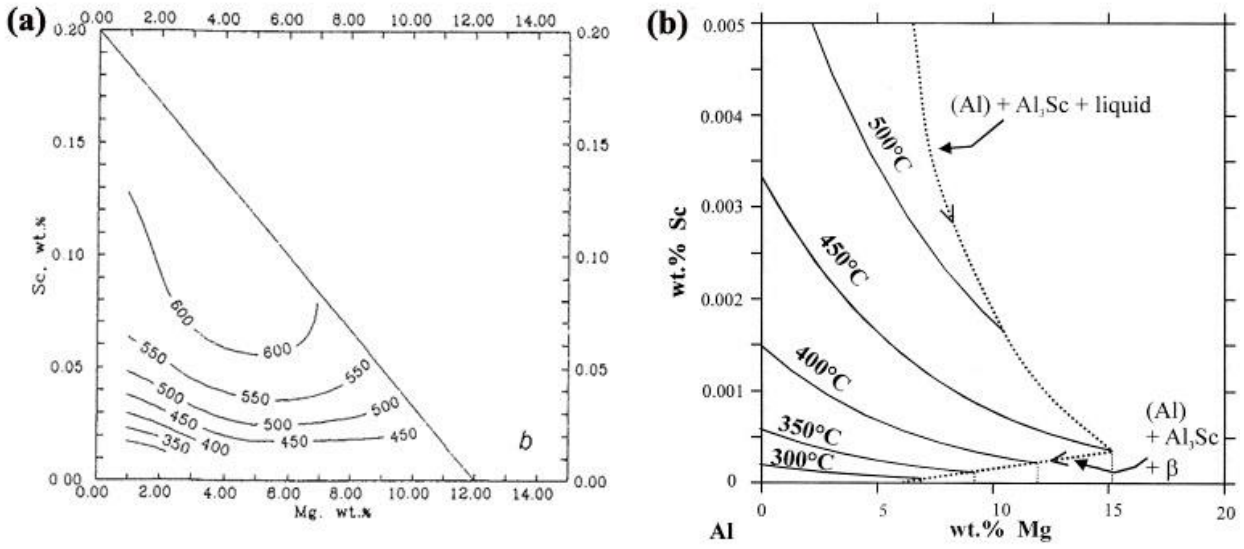

Figure 1.7. Isotherms of the solvus surface in the Al–Mg–Sc phase diagram: (a) [62] (b) [63].

The Al–Mg–Sc phase diagram was studied by Turkina and Kuzmina [62] up to 26 wt% Mg and 3 wt%. Isothermal section of the Al–Mg–Sc system at 430 °C was constructed and shown in Figure 1.8. The given portion of the phase diagram includes a single-phase field of the aluminium based solid solution, two two-phase fields (Al) + Mg_2Al_3 and (Al) + Al_3Sc, and a three-phase field (Al) + Mg_2Al_3 + Al_3Sc.

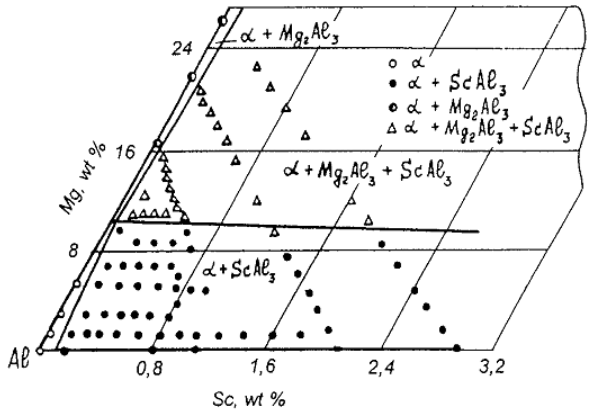

Figure 1.8. Isothermal section of the Al–Mg–Sc system at 430 ◦C [62].

Alexander Pisch *et al.* [63] indicated that the eutectic composition of Sc decreases with increasing Mg content in the Al–Mg–Sc alloy. The eutectic composition of Sc reduces down to 0.3 wt% Sc for 7 wt% Mg at 625°C (Figure 1.9).

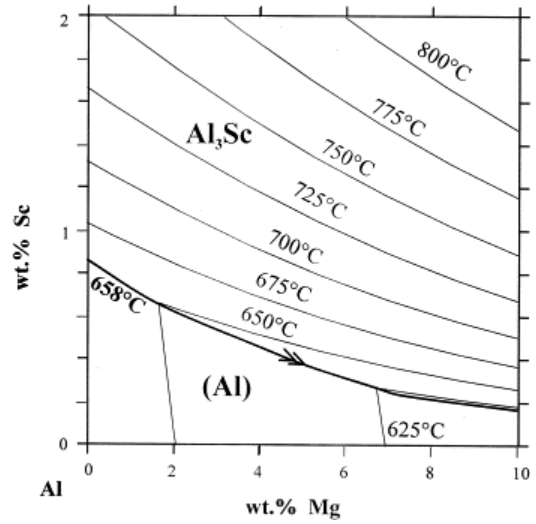

Figure 1.9. Liquidus surface of the Al rich corner in the Al–Mg–Sc system [63].

1.2.2 Precipitate coarsening kinetics

Some previous studies about Al–(0.2–0.5) wt% Sc indicated that very fine, coherent, and homogeneously distributed Al_3Sc precipitates are formed during heat treatment process at various temperature from 300–400 ◦C [37,41]. The evolution of precipitate follows the sequence of an initial incubation stage and nucleation, the precipitates nucleate from a supersaturated solid solution and grow, and then a gradual coarsening by Ostwald ripening [41,49]. No GP zones or metastable precipitates are observed [41]. The coarsening kinetics of the coherent precipitates obey the diffusion limited coarsening theory proposed by

Lifshitz and Slyozov [64] and Wagner [65] (LSW theory). The LSW theory is applied for binary alloys that are assumed as follow [66,67]:

- No elastic interactions occur among precipitates, thereby limiting the precipitate volume fraction to zero;
- The linearized version of the Gibbs-Thomson equation is valid;
- Coarsening occurs in a stress-free matrix;
- Dilute solution theory obtains;
- Diffusion fields of precipitates do not overlap;
- Precipitates have a spherical morphology;
- Precipitates form with the correct composition as given by the equilibrium phase diagram;
- Coarsening is a self-similar process.

The LSW theory was developed for concentrated multicomponent systems by Umantsev and Olson [68] and then studied more detail for ternary alloys which included capillary effects by Kuehmann and Voorhees [69]. The time exponent for the evolution of average precipitate radius $< R(t) >$ of the ternary alloys was predicted to be $1/3$, the same as for the binary alloys, but a different rate constant, K_{KV}, with the LSW model. Three following equations derived from the Kuehmann and Voorhees model for coarsening in ternary alloys [69] assume that quasi-stationary coarsening is occurring:

$$< R(t) >^3 - < R(t_0) >^3 = K_{KV}(t - t_0) \quad (1.3)$$

$$N_v(t)^{-1} - N_v(t_0)^{-1} = 4.74 \frac{K_{KV}}{V_v}(t - t_0) \quad (1.4)$$

$$\Delta C_i^{\alpha}(t) = < C_i^{\alpha}(t) > - < C_i^{\alpha}(t \to \infty) > = K_{i,KV}^{\alpha}(t)^{-1/3} \quad (1.4)$$

where K_{KV} and $K_{i,KV}^{\alpha}$ are the coarsening rate constants for $< R(t) >$ and $\Delta C_i^{\alpha}(t)$, respectively; $< R(t) >$ and $< R(t_0) >$ are the average precipitate radius at the onset of quasi-stationary coarsening at time t and t_0, respectively; $N_v(t)$ and $N_v(t_0)$ is the precipitate density at the onset of quasi-stationary coarsening at time t and t_0, respectively; V_v is equilibrium volume fraction of precipitates; the superscript α refers to the matrix phases; $\Delta C_i^{\alpha}(t)$ denotes supersaturation that is the difference between the concentration of i^{th} component in the matrix, $< C_i^{\alpha}(t) >$ is the composition of the i^{th} component in the matrix, and $< C_i^{\alpha}(t \to \infty) >$ is the solid-solubility of the i^{th} component in the matrix.

The theoretical expression of K_{KV} for the evolution of the precipitate radius is given by:

$$K_{KV} = \frac{8\sigma V_m}{9RT\sum_i(\frac{C_i^\alpha(1-k_i)^2}{D_i})} \qquad (1.5)$$

where V_m is the molar volume of the precipitate; σ is an isotropic interfacial free energy; R is the ideal gas constant; T is the absolute temperature; C_i^α is the composition of the i^{th} component in the matrix; D_i is the diffusion coefficient of the i^{th} component; k_i is the distribution coefficient of the i^{th} species between the matrix (α) and precipitate (β) phases that is defined by C_i^β / C_i^α.

In Al–Sc–Yb alloys, the i^{th} component is Sc and Yb.

The theoretical expression of $K_{i,KV}^\alpha$ is given by:

$$K_{i,KV}^\alpha = \frac{2\sigma V_m k_{exp}^{-1/3}(C_i^\beta - C_i^\alpha)}{RT\sum_i(C_i^\alpha(1-k_i)^2)} \qquad (1.6)$$

where k_{exp} is the experimentally determined coarsening rate constant, C_i^β is the composition of the i^{th} component in the precipitate phase.

In the Al–Sc alloys, Al_3Sc precipitates have slow coarsening rate due to the very low solid solubility of Sc in Al. As coherent precipitates coarsen, they eventually lose their coherency with the matrix, resulting in a decrease in the overall mechanical properties of the alloy and a rapid increase in coarsening rate. In Al–Sc alloys, a rapid coarsening of the precipitates was reported above 400 °C. Below this temperature, particles remain stable and coherent for long periods of time. The research of Iwamura and Miura [1] about the coarsening behaviour of the Al_3Sc particles in Al–0.2 wt% Sc alloy at 400–490 °C indicated that the coherent stage exists when the precipitate radius below 15 nm, semi-coherent stage exists when the precipitate radius over 40 nm, and the radius for coherent/semi-coherent transition where coherent and semi-coherent precipitates coexist is 15–40 nm.

Mg present in solid solution with α–Al that leads to reduce the lattice parameter mismatch between the matrix and Al_3Sc precipitates. As a consequence, Al_3Sc precipitates still remain coherent with α–Al matrix even in the large size. The lattice parameter mismatch is reduced from 1.35 to 0.54%, and the coherency loss occurs when precipitates coarse up to 116 nm in Al–6.3Mg–0.21Sc (wt%) alloy [52] and 80 nm in Al–3 wt% Mg–0.2 wt% Sc alloy.

1.2.3 Precipitation strengthening

Adding Sc leads to significantly increase strength of Al due to the formation of Al_3Sc precipitates. In the binary Al-Sc alloy, the most effective strengthening was reported when the alloys were perform the aging in the temperature range 250–350 ◦C. Yield strength of Al increases from 15 to 159 and 199 Mpa by adding 0.23 and 0.38 wt% Sc, respectively [5]. Adding 0.3 wt% of Sc increases the yield stress of Al-1 wt% Mg from 43 to 288 MPa and the ultimate tensile stress from 111 to 303 MPa [5]. Sc is the most effective precipitation hardening element per atomic fraction than any existing alloying addition [50, 70] (Only Au has a stronger strengthening effect than Sc [49]). However, the amount of Sc that can be precipitated from supersaturated solid solution is rather limited.

In the precipitation strengthening mechanisms, the dislocations in a material can interact with the precipitate particles through two ways: cutting or Orowan-bypassing mechanisms (Figure 1.10). Cutting or shearing occurs for small and coherent precipitates. As a result, new surfaces (b in Figure 1.10) of precipitate would get exposed to the matrix and the precipitate/matrix interfacial energy would increase. In the cutting mechanism, the strengthening effect of the precipitates is approximately proportional to the precipitate size (Figure 1.12). Four mechanisms can contribute to strengthen alloys when the dislocations shear through precipitates. They are: coherency strain, anti-phase-boundary energy (APB), interfaces, and modulus effect (Figure 1.11). There is a few researches studying about the strengthening mechanisms of binary Al–Sc alloys. The strengthening in Al–Sc alloys from coherency strain and APB energy was proposed by Parker *et al.* [71] and from shear modulus mismatch between the matrix and the precipitates was confirmed by Marquis *et al.* [4,48].

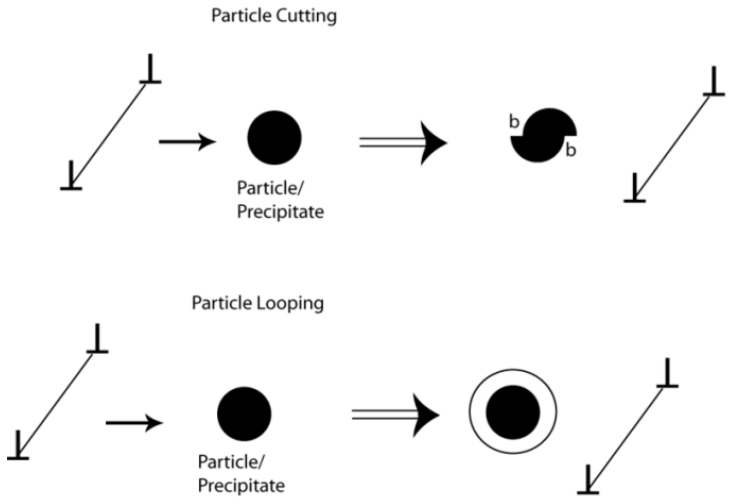

Figure 1.10. Schematic of the interaction of dislocations and second phase particle.

The Orowan-bypassing mechanism happens for larger precipitate particles. In this case, dislocation bowing between the precipitates and loop forming occurs when either the precipitates exceed a critical size or after they lose coherency (Figure 1.10). The strengthening effect of the precipitates is approximately proportional inversely to the precipitate size and the mean particle spacing (Figure 1.12). Torma *et al.* [72] study showed that the Orowan dislocation mechanism control the strengthening of Al–0.18 and 0.31 wt% Sc alloys at room temperature with coherent precipitates larger than 4.3 nm in radius. In Al–0.3 wt% Sc alloy, Marquis *et al.* [4] predicted a transition from cutting mechanism to Orowan bypass mechanism at a precipitate radius of 2.1 nm.

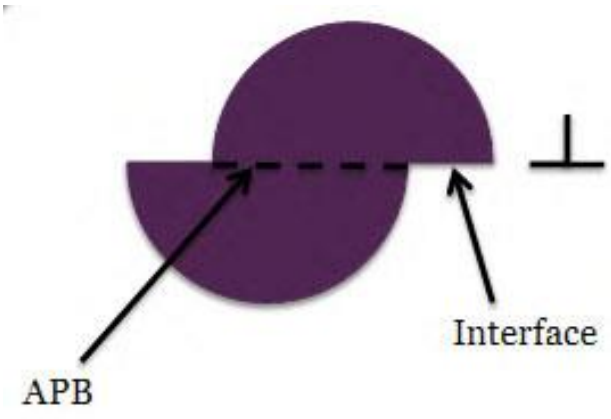

Figure 1.11. Schematic of a precipitate cutting.

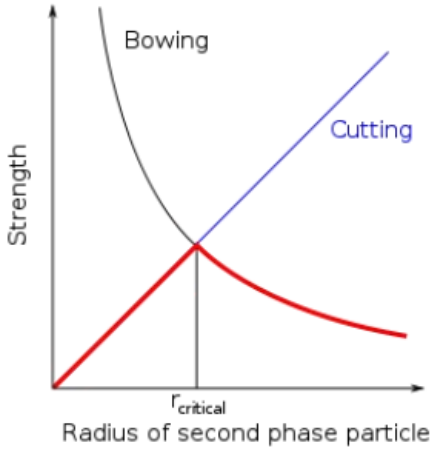

Figure 1.12. Shear Strength vs. Particle Radius.

1.2.4 The effect of Sc in aluminium alloys

1.2.4.1 Mechanical properties

The overview of yield strength and ultimate tensile strength of Al alloys containing Sc with deferent series is shown in Table 1.2. It can be seen that the yield strength of pure Al increases dramatically from 15 to 198 and 240 MPa by adding 0.23 wt% and 0.38 wt% of Sc, respectively [73]. With all series of Al alloys, the strength of alloy increase significantly when adding Sc.

Table 1.2. Literature data on the effect of Sc on the strength of the various classes of wrought aluinium alloys

Alloy system	Ref.	Alloy	Yield Strength (MPa)	Ultimate Tensile Strength (MPa)	Note
1xxx	[73]	Al Al–0.23Sc Al–0.38Sc	15 198 240	48 208 264	Cold rolled material (89%), aged 288 °C/8h
2xxx	[74]	2618 2618 + Sc,Zr	~260 ~340	~330 ~390	Rolled sheet, solution heat treated, aged to peak hardness at 200 °C (16-20h)
5xxx	[57]	Al–1Mg Al–1Mg–Sc (1515) Al–2Mg-Mn Al–2Mg-Sc (1523) Al–4Mg-Mn Al–4Mg-Sc (1535) Al–5Mg-Mn Al–5Mg-Sc (1545) Al–6Mg-Mn Al–6Mg-Sc (1570)	50 160 90 200 140 280 170 290 180 300	120 250 190 270 270 360 300 380 340 400	As hot worked or annealed condition
6xxx	[76]	6082 6082 + Sc,Zr	333/338 329/333	351/357 362/366	Extruded rods, T5 age hardening at 185°C/4h (1st value) and 165°C/24h
7xxx	[77]	6060 +Zr 6060 + Sc,Zr	81 182	163 247	Extruded rods, T1 condition
	[78]	1370	380	430	Rolled sheet, T6 condition
	[79]	7017 7017 + 0.25Sc	400 415	475 490	Hot rolled plate, solution heat treated + aged to max. hardness at 120°C
	[80]	Al–8.6Zn–2.6Mg–2.4Cu–0.1Zr Al–8.6Zn–2.6Mg–2.4Cu–0.1Zr–0.2Sc	649 689	672 715	Extruded rod, T6 condition
Al-Li	[81]	1420 (=1421 without Sc) 1421 1423 1424	270/280 320/340 350/330 320/320	440/450 460/480 460/460 475/425	Rolled sheet. Strength in longitudinal direction (1st value) and transverse direction (2nd value)

Tables 1.3 shows the mechanical properties of Al–Mg– 0.5 wt% Sc alloy with various compositions of Mg [82]. The yield strength and ultimate tensile strength of Al–0.5 wt% Sc alloy slightly increase and the elongation decreases when the content of Mg increase from 2 to 6 wt%.

Table 1.3. Mechanical Properties of Al-Sc and Al-Mg-Sc Alloys [82]

Alloys (wt%)	Yield Strength (MPa)	Ultimate Tensile Strength (MPa)	Elongation (%)
Al–0.5Sc	158.63	213.80	14
Al–2Mg–0.5Sc	202.08	265.35	10
Al–4Mg–0.5Sc	215.87	272.43	9.5
Al–6Mg–0.5Sc	255.19	286.22	9

1.2.4.2 Recrystallization resistance

Recrystallization in deformed materials is the formation of new grains free of dislocations by the formation and migration of high angle grain boundaries with misorientation angles larger than $10-15^{\circ}$ under the stored energy of deformation [83,84]. Recrystallization involves the growth of subgrains by mechanisms such as migration of low angle boundaries in an orientation gradient or strain induced boundary migration. Recrystallization is an important way to be considered for designing microstructures with required mechanical properties in aluminium alloys [84]. Previous studies about aluminium alloys have shown that through recrystallization controlling, fine grained microstructures with grain sizes of $1-2$ μm can improve the yield strength in comparison with coarse grained materials [85,86].

Precipitates can act as a factor to retard recrystallization. Two different conditions are required to form Al_3Sc precipitates for recrystallization resistance: (i) Sc is in solid solution before the deformation to ensure during annealing, the Al_3Sc precipitates nucleate and grow before recrystallization occurring; (ii) the Al_3Sc precipitates are formed in the alloy before deformation. The first publication about this characteristic was given in a patent [73] which showed the effect of 0.3 wt% Sc on the recrystallization of Al–Mg, Al–Mn and Al–Zn–Mg alloys. The results showed that the addition of Sc increase the temperature for initiation of recrystallization approximately 220 °C. Jones and Humphreys [13] studied the effect of Al_3Sc precipitates on recrystallization of Al–Sc alloys. The results showed that the recrystallization in Al–0.25 wt% Sc alloy only occurs at long aging times or temperatures higher than 500 °C. At these temperatures, precipitates coarsen

and lose their full coherency and therefore initiate recrystallization. In deformed supersaturated Al–0.12 wt% Sc alloy, at temperatures below 370 °C, precipitation happens and inhibits recrystallization. Above this temperature recrystallization and precipitation occur simultaneously. Figure 1.13 shows the recrystallization kinetics of Al–0.02 wt% Sc, Al–0.12 wt% Sc, and Al–0.25 wt% Sc alloys.

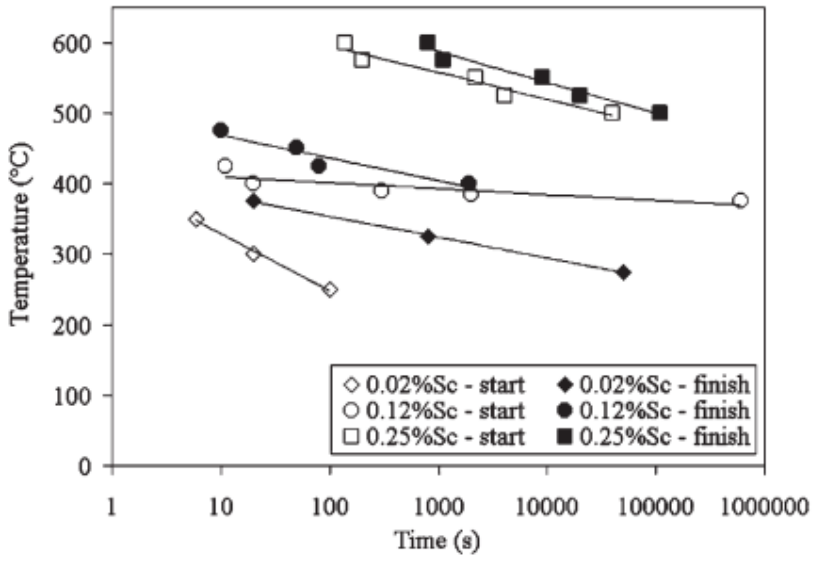

Figure 1.13. Isothermal recrystallization kinetics of Al-Sc alloys [13].

Ocenasek and Slamova [87] showed that fully recrystallization occurs in the AlMg3 alloy (AA5754) after 5 min annealing at 360 °C; the addition of 0.25 wt% Sc and 0.08 wt% Zr lead the alloy resist to recrystallization even when annealed for 8 h at 520 °C. The study of Yin *et al.* [88] had the same conclusion when adding Sc and Zr to Al–8.2Zn–2.1Mg–2.3Cu (wt%) alloy. According to Mirua's [89], the recrystallization temperature increase 200 °C when adding 0.2 wt% Sc to Al–3 wt% Mg alloy. Some studies have proven that Al_3Sc precipitates promote thermal stability to the deformed microstructures even at high temperatures in deformed Al–Sc alloys [90-92]. Figure 1.14 illustrates the effect of annealing time and temperature on grain size of Al–0.2 wt% Sc alloy deformed by equal channel angular pressing (ECAP) [92].

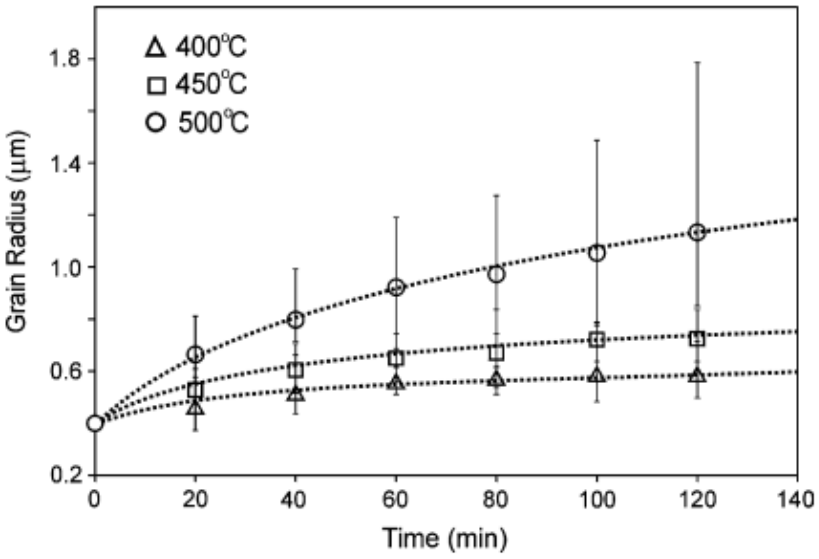

Figure 1.14. The effect of annealing time and temperature on grain size of Al–0.2 wt% Sc alloy [92].

1.2.4.3 Corrosion resistance

The studies about corrosion behaviour of Al alloys containing Sc reported that addition of Sc increases the corrosion potential (less negative) in pure Al [93,94], Al–Zn alloys [95,96], Al–Mg alloys [97] Al–Zn–Mg–Cu alloys [80,94], Al–Cu–Mg–Mn alloys [94], and Al–Cu–Li–Mg–Ag alloys [94]. Some characteristics were noted. The effect of Sc on the corrosion potential is more evident with the hypereutectic composition Al–Sc alloys [93]. The heat treatment conditions of Al alloys containing Sc can affect corrosion potential [80,97]. The results of corrosion rates and passivation current densities indicated that the addition of Sc enhances the corrosion resistance of wrought Al alloys [80,93,94,97].

Ahmad et al. [98] studied the effect of Al_3Sc precipitates on the corrosion behavior of Al–2.5 wt% Mg (5052) alloy adding 0.1–0.3 wt% Sc in 3.5 wt% NaCl. The result showed that Sc does not increase the corrosion rate of Al–Mg alloys. The better corrosion resistance in Al–2.5 wt% Mg–(0.1–0.3) wt% Sc alloys in comparison with commercial aluminium alloys such as 5052, 6063, 6013, 3023, 6061 was indicated. The weight-loss studies showed that the corrosion rate decreased with the exposure period. Table 1.4 summarizes the corrosion rates of Al–Mg–Sc alloys in 3.5 wt% of NaCl (after 400 h) and Table 1.5 shows the corrosion rates of some commercial aluminium alloys.

Table 1.4. Corrosion rate of Al–Mg–Sc alloys in 3.5 wt% of NaCl (after 400 h) [98]

Alloy	Corrosion rate	
	mm/year	Mdd*
Al–2.5Mg	0.023	1.477
Al–2.5Mg–0.1Sc	0.031	1.98
Al–2.5Mg–0.15Sc	0.046	2.914
Al–2.5Mg–0.3Sc	0.038	2.46

*mdd — milligrams per square decimeter per day.

Table 1.5. Corrosion rates of commercial aluminum alloys [98]

Alloy	Corrosion rate (mm/year)
6061	0.109 [99]
5052 (0 Zr)	0.071 [100]
3023	0.075 [100]
6063	0.109 [100]
6013	0.089 [98]

The corrosion rate of Al-2.5 wt% Mg-0.1 wt% Sc alloy decreases from 2.4 mdd (0.038 mm/y) to 1.44 mdd (0.023 mm/y) after 800 h exposure. It can be explained by the formation of protective films of either bayerite (β-$Al_2O_3 \cdot 3H_2O$) or boehmite (γ-$Al_2O_3 \cdot H_2O$). Pitting studies by ASTM cyclic-polarization technique showed that age hardening does not affect the pitting potential. The pitting data of Al–2.5 wt% Mg–(0.1–0.3) wt% Sc alloys in 3.5 wt% NaCl and some commercial alloys are shown in Table 1.6 and 1.7.

Table 1.6. Pitting potential (Ep) and protection potential (Epp) of Al–Mg–S alloy in 3.5 wt% NaCl [98]

Alloy	E_p (V)	E_{pp} (V)	E_{corr} (V)
Al–2.5Mg–0Sc	–0.521	–0.697	–0.643
Al–2.5Mg–0.1Sc	–0.578	–0.713	–0.659
Al–2.5Mg–0.15Sc	–0.518	–0.694	–0.628
Al–2.5Mg–0.30Sc	–0.670	–0.729	–0.742

Table 1.7. Ep values of some selected aluminum alloys in 3.5 wt% NaCl [98]

Alloy	E_p *V* vs SCE
6061	−0.669
6013	−0.688
2024	−0.540
5456	−0.695

The pitting potentials of Al–2.5 wt% Mg–(0.1–0.3) wt% Sc alloys show the more positive values in comparison with those of commercial Al–Mg alloys. It indicates a good pitting resistance of Al–2.5 wt% Mg–(0.1–0.3) wt% Sc alloys. The pitting morphologies of Al–2.5 wt% Mg–(0–0.3) wt% Sc alloys are shown in Figure 1.15. The alloys exhibit irregular crystallographic pits with small pitting depths. Pits on the alloy surface are covered by $Al(OH)_3$ (Figure 1.15 (d)).

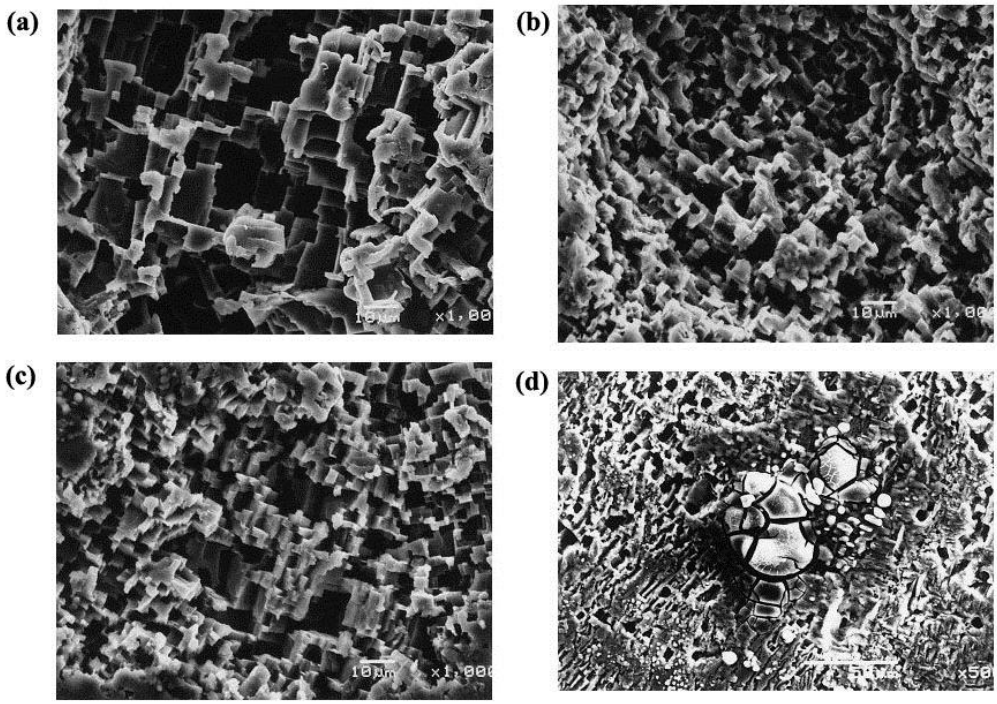

Figure 1.15. SEM micrographs showing crystallographic pitting of: (a) Al–2.5Mg, (b) Al–2.5Mg–0.1Sc, (c) Al–2.5Mg–0.15Sc, and (d) SEM micrographs of Al–2.5Mg–0.15Sc showing covering of pits by gelatinous $Al(OH)_3$ [98].

The effect of Al_3Sc particles on the initiation and propagation of pitting corrosion in 0.1 M NaCl of Al–Sc alloys was studied by Cavanaugh *et al.* [101]. The results showed that Al_3Sc exhibits a good electrochemical

compatibility with Al alloys and consequently better corrosion resistance than other common dispersoid intermetallic compounds in Al alloys as Al_6Mn, Al_3Zr and Al_3Ti. The comparison of the distribution of corrosion potential between Al_3Sc and other dispersoid intermetallic compounds is shown in Figure 1.16. Figure 1.17 illustrates the oxygen reduction reaction rate at −950 mV_{SCE} of dispersoid intermetallic compounds in 0.1 M NaCl solution. This figure shows that oxygen reduction reaction rate of Al_3Sc is slowest in comparison with others.

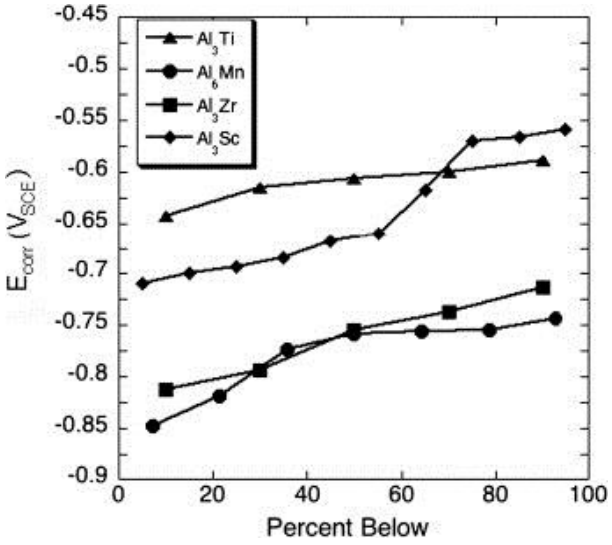

Figure 1.16. Distribution of corrosion potentials of Al_3Sc, Al_3Ti, Al_3Zr and Al_6Mn [101].

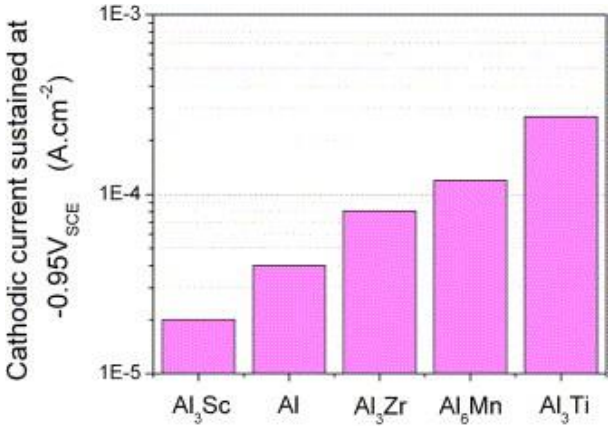

Figure 1.17. Magnitude of cathodic current sustained by Al_3Sc, Al (99.9999), Al_3Zr, Al_6Mn and Al_3Ti at a potential of −950 V_{SCE} in 0.1 M NaCl [101].

1.2.5 Al–Sc–REMs alloys

An element that substitutes for Sc in Al_3Sc should have the following characteristics if it is to be effective for high-temperature applications:

- to facilitate precipitation from a solid solution, it should have solubility in α–Al on the order of hundreds of ppm at the alloy homogenization temperature, but low solubility at aging and service temperatures [32];
- to limit the rate of precipitate coarsening, it should have a small diffusivity in α–Al;
- to increase creep resistance, it should increase the lattice parameter mismatch to maximize elastic interactions between precipitates and dislocations;
- to decrease the price of the alloy, it should be less expensive than Sc.

Many of these characteristics exhibited by the rare-earth metals (REMs) are attractive ternary additions because:

- many REMs substitute for Sc in the Al_3Sc precipitates forming $Al_3(Sc_{1-x}REM_x)$ ($L1_2$ structure) with a high solubility, thereby replacing the more expensive Sc [103,104];
- the light REMs have a smaller diffusivity in Al than Sc [105], improving the coarsening resistance of the precipitates;
- however, both the light REMs and ytterbium (Yb) have a larger diffusivity in Al [16] than Zr or Ti [28], so that the REM atoms are incorporated into the $L1_2$ precipitates with faster kinetics than the Zr or Ti atoms;
- unlike Ti or Zr [30], REMs increase the lattice parameter mismatch between α–Al and $Al_3(Sc_{1-x}REM_x)$ [103,104], which could increase the creep resistance of the alloy [31];
- from Table 1.8 the electronegativity difference between Al and Sc is small, which suggests that the bonding between the two is predominantly metallic or covalent. Most of the REMs have electronegativity values very similar to Sc, in where Y and Gd through Tm being the closest. This comparability suggests that these metals should strongly resemble Sc in their interaction with Al. The metallic radii of all RE metals are significantly larger than Sc. The closest in size of RE metals with Sc are Y and the series Gd though. This characteristic lead RE metals increase the lattice parameter mismatch between α–Al and $Al_3(Sc_{1-x}REM_x)$.

Table 1.8. Radii and electronegativity for various metals [106]

Metal	Atomic number	Metallic radius (nm)	Electronegativity
Al	13	0.143	1.61
Sc	21	0.162	1.36
Y	39	0.1802	1.22
Ce	58	0.182	1.12
Pr	59	0.182	1.13
Nd	60	0.182	1.14
Sm	62	0.182	1.17
Gd	64	0.1801	1.20
Tb	65	0.1782	1.20
Dy	66	0.1773	1.22
Ho	67	0.1765	1.23
Er	68	0.1757	1.24
Tm	69	0.1720	1.25
Yb	70	0.179	1.10
Lu	71	0.174	1.27

Sawtell and Morris [107,108] found that additions of 0.3 at% Er, Gd, Ho, or Y improve the ambient-temperature tensile strength of Al–0.3 at% Sc by 11-23%. Both Sc and the REMs exceeded their maximum equilibrium solid solubility, which, in the binary alloys, occurs at the eutectic temperatures of 639–655 °C for the various RE elements and 660 °C for Sc [109]. The samples were chill-cast with mildly rapid solidification rates of 10–100 Ks^{-1}. Since the Sc and REMs were supersaturated, the alloys in this study were not homogenized. The peak-aged tensile strength at room temperature, when compared to that of binary Al–0.3 at% Sc, was found to be up to 25% greater. Very small precipitates were observed by TEM after aging, which were assumed to be $Al_3(Sc_{1-x}REM_x)$. Therefore, the increased strengthening provided by the addition of 0.3 at% REM was attributed to an increase in volume fraction, strength and stability of $Al_3(Sc_{1-x}RE_x)$ precipitates.

Dunand and Seidman et al. [30,110-116] have paid a lot of attention to ternary Al–0.06Sc–0.02REM alloys (at%, REM = Y, Sm, Gd, Dy, Er, Yb, Tb, Ho, Tm or Lu). It was shown that REMs substitute for Sc in the nanoscale $L1_2$ trialuminide precipitates, resulting in an aging Vickers hardness response at 300 °C generally similar to that of a binary Al–0.08Sc alloy with the same solute concentration. The incubation time, peak hardness, and over-aging behaviour were mostly unaffected by the partial replacement of Sc by REM. Several exceptions were noted. First, Al–Sc–Sm and Al–Sc–Gd alloys have

lower peak strengths than Al–0.08Sc due to the lower solubility of these elements in Al_3Sc as compared to the other REMs studied, and due to the precipitation of micron-scale Al–Sm precipitates at the grain boundaries in the Al–Sc–Sm alloy. Second, a very rapid initial increase in the Vickers hardness of Al–Sc–Yb occurred, attributed to the experimentally observed clustering of Yb atoms at early aging times (including the as quenched state). Third, ATP studies demonstrated that Er and Gd (and therefore probably also the other REMs) partitioned to the $Al_3(Sc_{1-x}REM_x)$ precipitates and segregated at their cores [117]. The maximum solid solubilities in α-Al, as measured by APT of Er is 0.0461 ± 0.0006 at% and Yb is 0.0248 ± 0.0007 at% at 640 and at 625 °C, respectively. Both values are smaller than the maximum solubility of Sc in Al (0.23 at%). Hence, the maximum volume fraction of Al_3Yb (ϕ=0.11%) or Al_3Er (ϕ=0.14%) precipitates is smaller than that of Al_3Sc (ϕ=0.95%) in binary alloys. As compared to Sc, two REM Er and Yb have diffusivity in Al (Al–0.045 Er and Al–0.03 Yb alloys, at%) at 300 °C much significantly greater ((4 ± 2) x 10^{-19} m^2s^{-1} for Er, (6 ± 2) x 10^{-17} m^2s^{-1} for Yb and 9 x 10^{-20} m^2s^{-1} for Sc) [110]. The value for diffusivity of Yb in Al is larger in comparison with Er and five lighter lanthanides (La, Ce, Pr, Nd and Sm) which were extrapolated to 300 °C from data obtained above 450 °C [105, 113, 118]. The Al/Al_3REM interfacial free energies, $\gamma^{Al/Al3REM}$, calculated from the isothermal coarsening data at 300 °C, are $\gamma^{Al/Al3REM}$ –0.4 ± 0.2 and $\gamma^{Al/Al3REM}$ –0.6 ± 0.3 J m^{-2}, both of which are greater than $\gamma^{Al/Al3REM} \approx 0.2$ Jm^{-2} [29]. These results lead REM to the rapid decomposition of the supersaturated solid-solution and growth of the precipitates in α-Al.

In the study of Krug *et al.* [113], four ternary Al–0.08Sc–0.02REM alloys (at.%, REM = Tb, Ho, Tm or Lu) were cast, homogenized at 640 °C, and aged at 300 °C, resulting in nanoscale $Al_3(Sc_xREM_{1-x})$ precipitates responsible for increases in Vickers hardness. The microstructures of the alloys aged for 10 min and 24 h were investigated by ATP. The incubation times and thus the early age hardening behavior of the present Al–0.06Sc–0.02REM (where REM = Tb, Ho, Tm or Lu) fall between those of Al–0.06Sc–0.02Yb and Al– 0.06Sc–0.02Er, suggesting that diffusivity of these REMs stays between Er and Yb [113].

In another aspect, Yb has a lower melting temperature (824 °C) than Er (1497 °C) and the other lanthanides, which increase from 920 to 1545 °C with increasing atomic number, Z, with the exceptions of Ce (795 °C), Eu (826 °C) and Yb. Also, Yb is the only REM with a face-centered cubic crystal structure; all other REMs have a hexagonal close-packed structure except for the body-centered cubic Eu and the trigonal Sm. Finally, Yb has an anomalous valence state in Al compared with the other lanthanides (again except Eu) and has much different enthalpies of formation for the Al_2REM and Al_3REM phases.

1.2.6 Grain refinement of Al alloys

1.2.6.1 Grain refinement of Al–Sc alloys

A limited-solubility eutectic diagram of Sc with Al was shown in Figure 1.1. The maximum solid solubility of Sc in α–Al is 0.38 wt% and the eutectic composition is 0.55 wt% of Sc. The grain refinement effect of Sc occurs in hypereutectic alloys which the Sc content exceeds 0.55 wt%. In these alloys the Al_3Sc particles are the first phase to form in the melt during casting process. The lattice parameter of Al_3Sc is close to that of Al showing the small lattice parameter mismatch of them. Moreover the $L1_2$ structure of Al_3Sc is an ordered structure that based on the FCC structure of α–Al with Sc atoms at the face centres of the unit cell. These characteristics conduct Al_3Sc particles act as potent sites for the heterogeneous nucleation of α–Al grains [44]. Many researches have reported that very fine grains structure in aluminium alloys was obtained by adding Sc [44,45,119-125]. Those studies demonstrated that approximate 0.7wt% Sc is sufficient to provide excellent grain refinement.

In ternary and higher order systems, the eutectic Sc composition may depend on the present of other alloying elements. In the ternary Al–Mg–Sc system, the eutectic composition of Sc probably decrease with the increase of Mg content [63]. A good grain refinement was observed in Al–7Mg–0.5Sc (wt%) alloy [126]. It is also observed that grain refinement is obtained at low Sc contents by adding Sc together with Zr. The addition of 0.25 wt% Sc + 0.25 wt% Zr provides good grain refinement in pure Al [44]. Adding 0.2 wt% Sc + 0.1 wt% Zr to Al–5 wt% Mg alloys provides a finer grain size structure than adding either 0.2 wt% Sc, 0.6 wt% Sc or 0.1 wt% Zr [127]. Effect of Sc on grain size of Al–Sc and in an Al–Zn–Mg–Sc–Zr alloy is shown in Figure 1.18 [5]. The comparison of grain refinement with Sc content from 0.05 to 1.2 wt% shown in Figure 1.19 was reported by Zhang *et al.* [125].

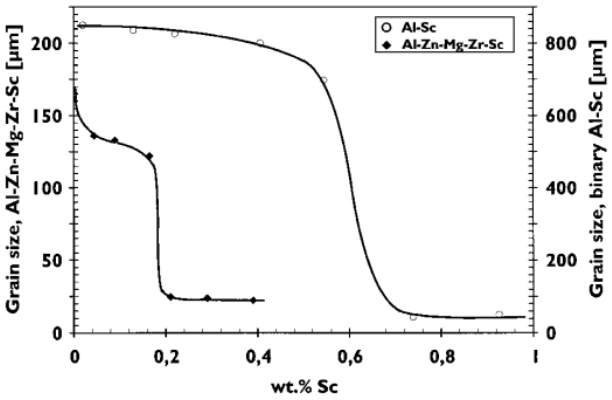

Figure 1.18. Grain refinement as a function of Sc addition in pure Al and Al–Zn–Mg–Zr [5].

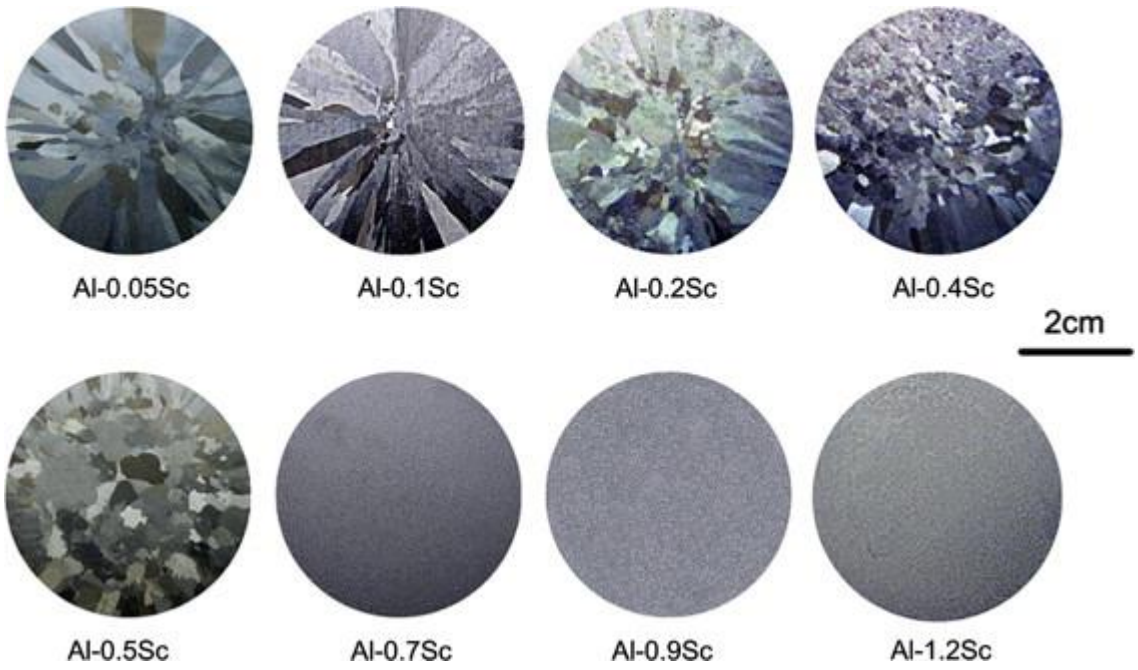

Figure 1.19. Comparison of grain refinement with Sc content from 0.05 wt% to 1.2 wt% [125].

1.2.6.2 Grain refinement mechanisms of Al alloys by adding Al–Ti–B grain refiner

In order to understand the grain refinement mechanism in Sc-containing Al alloys, we summarized the grain refinement mechanism of Al alloys by adding Al–Ti–B grain refiner that is quite similar with Al–Sc system. The proposed mechanisms for grain refinement can be divided into two groups:

✓ First is "nucleant paradigm" which proposed that the nucleant particle plays the most important role. The nucleant paradigm includes the following theories:

- Boride/carbide theory
- Phase diagram/peritectic theory
- Peritectic hulk theory
- Hypernucleation theory
- Duplex nucleation theory

✓ Second, called "solute paradigm" which assumed that the solute elements will decide a fine grained microstructure. According to the solute paradigm, the grain refinement mechanisms are driven by constitutional undercooling.

(i) Nucleant paradigm

- ***Boride/carbide theory***

The boride/carbide theory was first proposed by Cibula [128]. According to this theory, TiC and/or TiB_2 crystals nucleate solid aluminium by heterogeneous nucleation after the addition of Al–Ti–B master alloy. The added Ti and carbon impurities always present in the melt will react to form TiC. Soon after the addition of the master alloy, the $TiAl_3$ particles begin to dissolve rapidly, thereby creating a constitutionally favourable growth condition for α–Al to grow on these TiB_2 and TiC particles.

- ***Phase diagram/peritectic theory***

This theory in Al–Sc alloys was known as phase diagram/eutectic theory that was used to explain the grain refinement in hypereutectic Al–Sc alloys.

The peritectic nucleation theory proposed that grain refinement is achieved by a peritectic reaction of transition elements such as Ti, Sc, Zr, Cr, Mo and W with Al. According to Al–Ti phase diagram, the reaction in the melt of Al alloys containing Ti can occur as follows:

$$Al\ (liquid) + TiAl_3 \rightarrow Al\ (solid\ with\ titanium\ in\ solid\ solution)$$

The peritectic reaction occurs at approximately 665°C at a minimum concentration of 0.15 wt% Ti. The $TiAl_3$ particles will act as nuclei sites for heterogeneous nucleation of α-Al grain. A layer of α-Al then forms and completely encloses the surface of the particle. Figure 1.20 shows the aluminium-rich side of the Al–Ti phase diagram with the peritectic point at 1.2 wt% Ti and 665°C.

The big problem of this theory is that could not explain the grain refinement in Al alloys when the content of Ti is lower than 0.15 wt%. Delamore and Smith [129] suggested that probably $TiAl_3$ nucleates aluminium heterogeneously without any peritectic reaction. Marcantino and Mondolfo [130] proposed that, the existence of boron can shift in the peritectic reaction to a composition below 0.15 wt% Ti. They suggested the ternary Al–Ti–B peritectic reaction as follows [130]:

$$Liquid \rightarrow (Al, Ti)B_2 + TiAl_3 + Solid$$

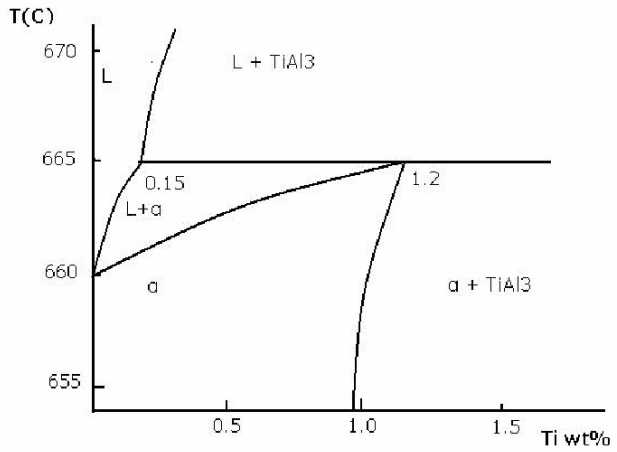

Figure 1.20. Detail of Al–Ti phase diagram showing the minimum Ti content for the peritectic reaction at 0.15% and 665°C [131].

However, there is no experimental record that can prove those suggestions. Theoretical thermodynamic analyses from Jones and Pearson [132] and Sigworth [131,133] study has shown that ternary peritectic does not occur. Another problem came from Johnsson and Backerud [134] study that indicated that Al_3Ti would dissolve into the melt. They suggested that Al_3Ti would take less than 1 minute to dissolve at 775 ± 10 °C. According Backerud *et al.* [135], a spherical Al_3Ti with size of 20 μm would dissolve into the melt in 3–4 seconds.

- ***Peritectic Hulk theory***

The peritectic hulk theory was proposed by Backerud *et al.* [135] and Vader and Noordegraaf [136]. This theory suggested that Al_3Ti is a more powerful nucleant than TiB_2. According to the peritectic hulk theory, TiB_2 shell will be formed around the Al_3Ti and therefore slow down the dissolution of Al_3Ti. The Al_3Ti dissolves inside of TiB_2 shell to form the liquid with the higher content of Ti than other sites. The peritectic reaction occurs and α-Al could be nucleated and grown [137]. However, TiB_2 shells existed more often in Al grains than at the centre of grains at hypopretectic concentrations [138]. Indeed, the peritectic hulk theory is not evident to explain the grain refinement properly.

- ***The hyper-nucleation Theory***

The hyper-nucleation theory was proposed by Jones [139] which suggested that:

- melt solutes can segregate stably to the interface of the melt-inoculants;
- with the right conditions, stable pseudo-crystals can be created even above the liquidus;
- immediately below the liquidus these pseudo crystals allow nucleation and growth of α-Al;

- the atomic size of the segregant element relative to aluminium is a key factor in hyper nucleation;
- competitive segregation of solutes with mismatching size can poison the process.

According this theory, TiB_2 creates an activity gradient that leads Ti atoms to segregate at the TiB_2/melt interface. The preitectic reaction would occur and a thin layer of $TiAl_3$ could be formed on the TiB_2 particles that can act as nuclei sites for α-Al grains. But the main problem of this theory is that there is no evident experimental result to prove it.

- ***Duplex nucleation theory***

This theory was proposed by Mohanty et al. [34,140] and further convincing evidence has been provided by Greer and Schumacher and co-workers [141,142]. The theory suggested that at a hyperperitectic composition of Ti, Al_3Ti layer was formed on the surface of TiB_2 and around which was an α-Al layer. However, at a hypoperitectic concentration of Ti, Al_3Ti layer existed in between the TiB_2 and α-Al. The formation of Al_3Ti could be due to the adsorption effect at the boride/aluminide interface but the stability of this layer has not been confirmed. Johnsson *et al.* [143] measured the nucleation and growth temperature across the Al-Ti phase diagram and mentioned that the liquid adjacent to the Al_3Ti needs to be 0.15wt% Ti which means the nucleation temperature should correspond to the nucleation temperature at the peritectic concentration. For an alloy containing 0.05 wt% Ti this means the nucleation temperature should be 3 °C above the liquidus temperature and the duplex nucleation theory would fail to explain this.

(ii) Solute paradigm

This theory was proposed by Johnsson *et al.* [143] which suggested that nucleants and segregating solutes are two main factor to control grain refinement. The solute paradigm was based on the constitutional undercooling mechanism. The equiaxed crystal can nucleate in the solute-enriched liquid ahead of a growing solid/liquid interface. Solute elements like Ti, Si and Fe have a restrictive effect on the solidifying metal. They segregate to the nucleant/melt interface and restrict the growth of dendrites. They build up a constitutionally undercooled zone in front of the interface [137] that facilitates nucleation and produce nuclei for α-Al grains. A schematic of constitutional undercooled zone in front of the interface mechanism was shown in Figure 1.21.

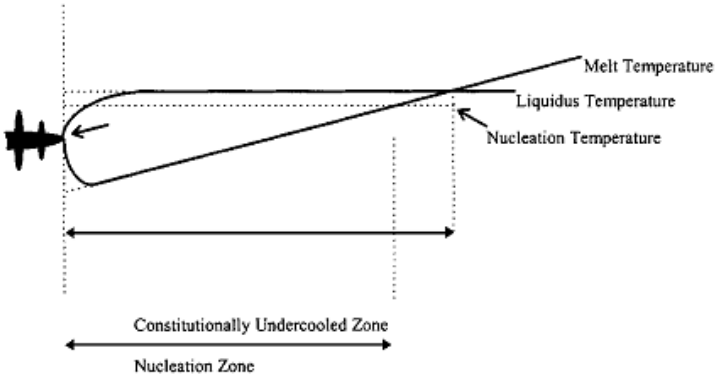

Figure 1.21. Constitutional undercooled zone in front of the interface. The size of the zone depends on the nucleant and the constitution of the melt [137].

The growth-restricting factor (GRF) measures the growth restricting effect of solute elements on the growth of the solid-liquid interface of the new grains in the melt. It was used to evaluate the segregation potential of elements. Solute elements like Ti, Si and Fe have been found to restrict dendrite growth and their GRFs prove more clearly for that observation. Particularly, Ti showed a strong tendency to segregate that lead to more effective on grain refinement.

Many researches have studied the effect of solute elements on grain refinement through controlling the growth with the growth–restriction parameter Q [144-146]. Maxwell and Hellawell [146] investigated the effect of the number of nucleant particles and the amount of solute on grain refinement. The evaluation was based on the nucleant potency, cooling rate, nucleant particle size and segregating potency of the solute elements. They predicted that GRF has the largest effect on grain size of alloys. The effect of GRF on grain size was shown in Figure 1.22. This paradigm could explain why TiB_2 has no grain refinement effect when adding into the alloys. Because there are no segregating elements and constitutionally undercooled zone to promote nucleation in front of the interface does happen.

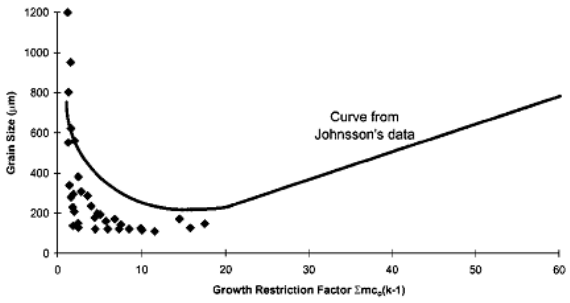

Figure 1.22. Graph from Spittle and Sadli's grain size data plotted against the GRF [137].

(iii) Summary

Table 1.9 summarises all theories above and describes the nucleating substrate and the effect of solute on grain refining in each case. However, the mechanism of grain refinement is still not clear and considerable controversy still surrounds this issue.

Table 1.9. Summary of the important grain refinement theories, in terms of their understanding of nucleation and the effect of solute

Theory	Nucleating substrate	Effect of solute in grain refining performance
The nucleant paradigm		
Boride diagram theory	On borides or carbides	None, except some suggest Ti as a powerful segregant restricts growth of grains, which allows for further nucleation events.
Phase diagram theories	Via peritectic reation	Ti is present to form Al_3Ti, which acts as nucleant.
Peritectic hulk	In a Ti-rich boride shell via the peritectic reation	Ti present in the boride shell after Al_3Ti dissolution at the peritectic concentration.
Hypernucleation	On borides	Ti segregates down an activity gradient to the boride to provide a suitable interface for nucleation of α-Al
Duplex nucleation	On Al_3Ti, which is formed on the surface of TiB_2 particles	Ti is present to segregate to TiB_2 down an activity gradient to form Al_3Ti on the surface, which then nucleates Al.
The solute paradigm		
Undercooling-driven mechanism	Borides (or other partcles)	Solute affects dendrite growth and builds up constitution ally undercooled zone in front of the interface. This undercooled zone facilitates nucleation and the new grain does the same to the next grain. The shape and magnitude of the constitutionally undercooled zone depend upon the dendrite growth, which is affected by solute, which in turn affects the subsequent nucleation behaviour.

1.2.6.3 Grain refinement mechanism by ultrasonic treatment

Three mechanisms have been proposed to explain for grain refinement by ultrasonic treatment:

- Cavitation-enhanced heterogeneous nucleation.
- Cavitation-induced dendrite fragmentation.
- Vibration-stimulated separation of wall crystals.

i) Cavitation-enhanced heterogeneous nucleation

The cavitation-enhanced heterogeneous nucleation was explained through three mechanisms:

- The first mechanism is based on the promotion of the wetting behaviour of second phase particles with the melt due to cavitation bubbles collapse. When ultrasonic vibration was applied into the melt, a large number of cavitation bubbles were formed and dispersed in the whole of the melt. The collapse of cavitation bubbles in the vicinity of second phase particles leads to produce locally high temperature, pressures and melt flows [147]. The pressures pulse promotes filling of the cracks (capillaries) on the surface of second phase particles by the melt and improves the wetting of those particles with the melt [148]. According to Easton and StJohn [149], the higher wettability of substrates with the melt leads to the smaller free energy barrier for nucleation even at relatively low undercooling. As a consequence, these substrates will acts as effective nucleation sites and enhance the nucleation [147].
- The second mechanism is based on the pressure pulse melting point where the pressure pulse generated from the cavitation bubbles collapse conducts the increasing of melting point according to the Clausius-Clapeyron equation [147,150]. Consequently, the localized undercooling occurs that leads to promote nucleation throughout the melt.
- The third mechanism explained that the expansion of gas inside the cavitation bubbles leads to increase the bubble size and decrease the bubble temperature [150,151]. This phenomenon resulted in undercooling of the melt and form nuclei on the surface of bubbles. When these bubbles collapsed, a significant number of nuclei were produced into the melt and promoted heterogeneous nucleation in the melt.

ii) Cavitation-induced dendrite fragmentation

In the cavitation-induced dendrite fragmentation mechanism, fragmentation of dendrites occurred by the shock waves that were generated from bubbles collapse. These fragments were distributed throughout the melt by acoustic streaming which leads to increase the number of solidification sites [147,152,153].

iii) Vibration-stimulated separation of wall crystals

The ultrasonic treatment increased the wettability of the mould wall with the melt that resulted in the promotion of nucleation on the mould wall [154]. The local shaking and/or shearing during ultrasonic vibration conducted the separation of the nuclei from the mould wall into the whole of the melt. Due to this trend, the number of nucleation sites was increase and hence grain refinement was obtained.

1.2.7 Application of Sc-containing Al alloys

Sc-containing Al alloys have been used in a wide range of applications. They are potentially applied in automotive and aerospace for wheels, running gear, seat tracks, bumpers, frames, pistons and fuel and exhaust systems. Some of Sc-containing Al alloys are used in MiG 29 fighter aircrafts. Al–Mg–Sc and Al–Mg–Li–Sc alloys have been evaluated to use in structural applications of Airbus airplanes. AirLite ScTM handgun produced by Smith & Wesson is made by Sc–containing Al alloys. Due to a good corrosion resistance, Sc–containing Al alloys can be used in a saltwater environment as heat exchanger tubes in desalination plants.

Ashurst Technology has succeeded to produce sports equipment by Sc–containing Al alloys as bicycle frames, baseball/softball bats, and lacrosse sticks. Using Sc–containing Al alloys in bicycle frames lead to reduce 12% of weight, increase 50% of yield strength and 24% of fatigue in comparison with best-selling aluminium bicycle. Alloy designated Sc7000 and Sc 61.10 A have been used in bicycle frame tubing by Easton Bicycle Products Group and Dedacciai (Italian bicycle tubing manufacturer), respectively. Aluminium alloys designated Sc500 by Ashurst Technology and Sc777 by Kaiser Aluminium have been used in baseball/softball bats by Easton. Sc777 is used three new lines of baseball/softball bats: Sc777 Triple Seven series, Sc777 Z-Core series and Sc777 ConneXion series. Sc containing Al alloys designated C555 was produced by Alcoa that was used in baseball/softball bats by DeMarini, Louisville Slugger and Worth manufacturers. All of those alloys above are Al–Zn–Mg–Sc alloys. Hawk series of baseball/softball bats from Nike also are made from Sc containing alloy designated ScX. STX is a major Lacrosse equipment manufacturer. They produced Lacrosse stick handles from Sc–containing Al alloys provided by Ashurst Technology and Kaiser Aluminum. Birdland, an outdoor equipment manufacturer, have introduced a series of lightweigth tents, Colibri made from Sc-containing Al alloys that is designated Alu–SC.

References

[1] Iwamura S, Miura Y. Loss in coherency and coarsening behavior of Al3Sc precipitates. Acta Mater. 2004;52:591-600.

[2] Toropova LS, Eskin DG, Kharakterova ML, Dobatkina TV. Advanced aluminum alloys containing scandium: structure and properties. Amsterdam, The Netherlands: Gordon and Breach; 1998.

[3] Marquis EA, Seidman DN. Nanoscale structural evolution of Al3Sc precipitates in Al(Sc) alloys. Acta Mater. 2001;49:1909-19.

[4] Marquis EA, Seidman DN, Dunand DC. Precipitation strengthening at ambient and elevated temperatures of heat-treatable Al(Sc) alloys. Acta Mater. 2002;50:4021–35.

[5] Røyset J, Ryum N. Scandium in aluminium alloys. Int. Mater. Rev. 2005;50:19-44.

[6] Drits MY, Ber LB, Bykov YG, Toropova LS, Anastas'eva GK. Aging of alloy Al-0. 3 at. %Sc. Phys. Met. Metallogr. 1984;57:118-26.

[7] Blake N, Hopkins MA. Constitution and age hardening of Al-Sc alloys. J. Mater. Sci. 1985; 20: 2861-7.

[8] Clouet E, Barbu A, Laé L, Martin G. Precipitation kinetics of Al3Zr and Al3Sc in aluminum alloys modeled with cluster dynamics. Acta Mater. 2005;53:2313-25.

[9] Fuller CB, Seidman DN, Dunand DC. Creep properties of coarse-grained Al(Sc) alloys at 300°C. Scri. Mater. 1999;40:691-6.

[10] Hyland RW. Homogeneous Nucleation Kinetics of Al3Sc in a dilute Al-Sc alloy. Metall. Trans. A. 1992;23:1947-55.

[11] Novotny GM, Ardell AJ. Precipitation of Al3Sc in binary Al–Sc alloys. Mater. Sci.Eng. A. 2001;318:144-54.

[12] Kramer LS, Tack WT, Fernandes MT. Scandium in aluminum alloys. Adv. Mater. Processes. 1997;152:23-4.

[13] Jones MJ, Humphreys FJ. Interaction of recrystallization and precipitation: The effect of Al3Sc on the recrystallization behaviour of deformed aluminium. Acta Mater. 2003;51:2149-59.

[14] Ocenasek V, Slamova M. Resistance to recrystallization due to Sc and Zr addition to Al-Mg alloys. Mater. Charact. 2001;47:157-62.

[15] Norman AF, Hyde K, Costello F, Thompson S, Birley S, Prangnell PB. Examination of the effect of Sc on 2000 and 7000 series aluminium alloy castings: for improvements in fusion welding. Mater. Sci. Eng. A. 2003;354:188-98.

[16] Paglia CS, Jata KV, Buchheit RG. A cast 7050 friction stir weld with scandium: microstructure, corrosion and environmental assisted cracking. Mater. Sci. Eng. A. 2006;424:196-204.

[17] Irving B. Scandium Places Aluminum Welding on a New Plateau. Welding Journal. 1997;7:53-7.

[18] Marquis EA, Seidman DN, Dunand DC. Effect of Mg addition on the creep and yield behavior of an Al-Sc alloy. Acta Mater. 2003;51:4751-60.

[19] Marquis EA, Seidman DN, Dunand DC. Microstructure and creep of the Al-2Mg-0.2Sc alloy. TMS Annual Meeting. 2003; 177-84.

[20] Marquis EA, Seidman DN, Asta M, Woodward C, Ozoliņš V. Mg Segregation at Al/Al{3}Sc Heterophase Interfaces on an Atomic Scale: Experiments and Computations. Phys. Rev. Lett. 2003;91:036101.

[21] Marquis EA, Seidman DN. Nanostructural evolution of Al3Sc precipitates in an Al-Sc-Mg alloy by three-dimensional atom probe microscopy. Surf. Interface Anal. 2004;36:559-63.

[22] Marquis EA, Seidman DN, Asta M, Woodward C. Composition evolution of nanoscale Al3Sc precipitates in an Al–Mg–Sc alloy: Experiments and computations. Acta Mater. 2006;54:119-30.

[23] Fuller CB, Seidman DN, Dunand DC. Mechanical properties of Al(Sc,Zr) alloys at ambient and elevated temperatures. Acta Mater. 2003;51:4803-14.

[24] van Dalen ME, Dunand DC, Seidman DN. Effects of Ti additions on the nanostructure and creep properties of precipitation-strengthened Al-Sc alloys. Acta Mater. 2005;53:4225-35.

[25] Fuller CB, Murray JL, Seidman DN. Temporal evolution of the nanostructure of Al(Sc,Zr) alloys: Part I – Chemical compositions of Al3(Sc1−xZrx) precipitates. Acta Mater. 2005;53:5401-13.

[26] Fuller CB, Seidman DN. Temporal evolution of the nanostructure of Al(Sc,Zr) alloys: Part II-coarsening of Al3(Sc1-xZrx) precipitates. Acta Mater. 2005;53:5415-28.

[27] Marumo T, Fujikawa S, Hirano K-i. Diffusion of zirconium in aluminum. J Jap Inst Light Metals. 1973;23:17-25.

[28] Bergner D, Chi NV. Wissenschaftliche Zeitschrift der Padagogischen Hochschule Halle 1977;15:15.

[29] Fujikawa SI. Impurity diffusion of scandium in aluminum. Defect Diff. Forum. 1997;143:115–20

[30] Harada Y, Dunand DC. Microstructure of Al3Sc with ternary transition-metal additions. Mater. Sci. Eng. A. 2002;329–331:686-95.

[31] Marquis EA, Dunand DC. Model for creep threshold stress in precipitation-strengthened alloys with coherent particles. Scri. Mater. 2002;47:503-8.

[32] Knipling KE, Dunand DC, Seidman DN. Criteria for developing castable, creep-resistant aluminum-based alloys - A review. Z. Metallkd. 2006;97:246-65.

[33] Wannasin J, Canyook R, Wisutmethangoon S, Flemings MC. Grain refinement behavior of an aluminum alloy by inoculation and dynamic nucleation. Acta Mater. 2013;61:3897-903.

[34] Mohanty PS, Gruzleski JE. Mechanism of grain refinement in aluminium. Acta Metall. Mater. 1995;43:2001-12.

[35] Kiourtsidis GE. Stress corrosion behavior of aluminum alloy 20247 silicon carbide particles (SiCp) metal matrix composites. Corrosion. 2000;56:646-53.

[36] Trzaskoma PP. Corrosion behavior of SiC/Al metal matrix composites. J. Electrochem. Soc. 1983; 130:1804-9.

[37] Hyland RW. Homogeneous nucleation kinetics of Al3Sc in a dilute Al-Sc alloy. Metall. Mat Trans A. 1992;23:1947-55.

[38] Murray JL. The Al-Sc (aluminum-scandium) system. J. Phase Equil. 1998;19:380-4.

[39] Røyset J, Ryum N. Kinetics and mechanisms of precipitation in an Al–0.2wt% Sc alloy. Mater. Sci. Eng. A. 2005;396:409-22.

[40] Očko M, Babić E, Krsmik R, Girt E, Leontić B. Some properties of AlSc solid solutions. J. Phys. F: Met. Phys. 1976;6:703-7.

[41] Sano N, Hasegawa Y, Hono K, Jo H, Hirano K, Pickering H, W., et al. Precipitation process of Al-Sc alloys. J Phys Colloques. 1987;48:C6-337-C6-42.

[42] Xia K, Tausig G. Liquidus casting of a wrought aluminum alloy 2618 for thixoforming. Mater. Sci. Eng. A. 1998;246:1-10.

[43] Harada Y, Dunand DC. Thermal expansion of Al3Sc and Al3(Sc0.75X0.25). Scri. Mater. 2003;48:219-22.

[44] Norman AF, Prangnell PB, McEwen RS. The solidification behaviour of dilute aluminium–scandium alloys. Acta Mater. 1998;46:5715-32.

[45] Hyde KB, Norman AF, Prangnell PB. The effect of cooling rate on the morphology of primary Al3Sc intermetallic particles in Al–Sc alloys. Acta Mater. 2001;49:1327-37.

[46] Hyde KB, Norman AF, Prangnell PB. The Growth Morphology and Nucleation Mechanism of Primary Ll2 Al3Sc Particles in Al-Sc Alloys. Mater. Sci. Forum. 2000;31-337:1013-8.

[47] Robson JD, Jones MJ, Prangnell PB. Extension of the N-model to predict competing homogeneous and heterogeneous precipitation in Al-Sc alloys. Acta Mater. 2003;51:1453-68.

[48] Seidman DN, Marquis EA, Dunand DC. Precipitation strengthening at ambient and elevated temperatures of heat-treatable Al(Sc) alloys. Acta Mater. 2002;50:4021-35.

[49] Jo HH, Fujikawa SI. Kinetics of precipitation in Al-Sc alloys and low temperature solid solubility of scandium in aluminum studied by electrical resistivity measurements. Mater. Sci. Eng. A. 1993;171:151-61.

[50] Drits MY, Ber LB, Bykov YG, Toropova LS, Anastas'eva GK. Ageing of alloy Al-0.3 at%Sc. Phys. Met. Metallogr. 1984;57:118-26.

[51] Elagin VI, Zakharov VV, Rostova TD. Some features of decomposition for the solid solution of scandium in aluminum. Met. Sci. Heat Treat. 1983;25:546-9.

[52] Drits ME, Bykov YG, Toropova LS. Effect of ScAl3 phase dispersity on hardening of Al-6.3% Mg-0.21% Sc alloy. Met. Sci. Heat Treat. 1985;27:309-12.

[53] Riddle YW, Sanders TH. Contribution of Al3Sc to Recrystallization Resistance in Wrought Al-Sc Alloys. Mater. Sci. Forum. 2000;31-337:939-44.

[54] Polmear IJ. Light alloys: metallurgy of the light metals. E. Arnold; 1982.

[55] Liu Z, Li Z, Wang M, Weng Y. Effect of complex alloying of Sc, Zr and Ti on the microstructure and mechanical properties of Al–5Mg alloys. Mater. Sci. Eng. A. 2008;483–484:120-2.

[56] Fuller CB, Krause AR, Dunand DC, Seidman DN. Microstructure and mechanical properties of a 5754 aluminum alloy modified by Sc and Zr additions. Mater. Sci. Eng. A. 2002;338:8-16.

[57] Filatov YA, Yelagin VI, Zakharov VV. New Al-Mg-Sc alloys. Mater. Sci. Eng. A. 2000;280:97-101.

[58] Sawtell R, Jensen C. Mechanical properties and microstructures of Al-Mg-Sc alloys. Metall. Mater. Trans. A. 1990;21:421-30.

[59] Lapasset G, Girard Y, Campagnac MH, Boivin D. Investigation of the microstructure and properties of a friction stir welded Al-Mg-Sc alloy. Mater. Sci. Forum. 2003;426-432:2987-92.

[60] Lee S, Utsunomiya A, Akamatsu H, Neishi K, Furukawa M, Horita Z, et al. Influence of scandium and zirconium on grain stability and superplastic ductilities in ultrafine-grained Al–Mg alloys. Acta Mater. 2002;50:553-64.

[61] Fazeli F, Poole WJ, Sinclair CW. Modeling the effect of Al3Sc precipitates on the yield stress and work hardening of an Al–Mg–Sc alloy. Acta Mater. 2008;56:1909-18.

[62] Turkina NI, Kuzmina VI. Phase Reactions in Al-Mg-Sc Alloys (up to 26% Mg and 3% Sc). Metally. 1976;4:179-81.

[63] Pisch A, Gröbner J, Schmid-Fetzer R. Application of computational thermochemistry to Al and Mg alloy processing with Sc additions. Mater. Sci. Eng. A. 2000;289:123-9.

[64] Lifshitz IM, Slyozov VV. The kinetics of precipitation from supersaturated solid solutions. J. Phys. Chem. Solids. 1961;19:35-50.

[65] Wagner CZ, Elektrochem Z. Angew Phys Chem. 1961;65:581.

[66] Ratke L, Voorhees PW. Growth and Coarsening: Ostwald Ripening in Material Processing. Series: Engineering Materials. Springer; 2002.

[67] Wagner R, Kampmann R, Voorhees PW. Homogeneous Second-Phase Precipitation. Phase Transformations in Materials. Wiley-VCH Verlag GmbH & Co. KGaA; 2005. 309-407.

[68] Umantsev A, Olson GB. Ostwald ripening in multicomponent alloys. Scri. Metall. Mater. 1993;29:1135-40.

[69] Kuehmann CJ, Voorhees PW. Ostwald ripening in ternary alloys. Metall. Mater. Trans. A. 1996;27:937-43.

[70] Drits ME, Dutkiewicz J, Toropova LS, Salawa J. The effect of solution treatment on the ageing processes of Al—Sc alloys. Cryst. Res.Technol. 1984;19:1325-30.

[71] Parker BA, Zhou ZF, Nolle P. The effect of small additions of scandium on the properties of aluminium alloys. J. Mater. Sci.. 1995;30:452-8.

[72] Torma T, Kovács-Csetényi E, Turmezey T, Ungár T, Kovács I. Hardening mechanisms in Al-Sc alloys. J. Mater. Sci. 1989;24:3924-7.

[73] Wille LA. US patent 3 619 181November 9 1971.

[74] Kun YU SL, Wenxian LI. Effect of trace Sc and Zr on the mechanical properties and microstructure of Al alloy 2618. J Mater Sci Technol. 2000;16:416-20.

[75] Riddle YW, Hallem H, Ryum N. Highly Recrystallization Resistant Al-Mn-Mg Alloys Using Sc and Zr. Mater. Sci. Forum 2002;396 - 402:563-8.

[76] Røyset J, Tundal U, Skjervold SR, Waterloo G, Braathen C, Reiso O. An Investigation of Sc Addition on the Extrudability, Recrystallisation Resistance and Mechanical Properties of a 6082- and a 7108-Alloy. In: Nie JF, Morton AJ, Muddle BC, editors. 9th International Conference on Aluminium Alloys. Brisbane, Australia: Institute of Materials Engineering Australasia Ltd; Aug. 2-5 2004. p. 246-51.

[77] Leo P, Cerri E, De Marco PP, Roven HJ. Properties and deformation behaviour of severe plastic deformed aluminium alloys. J. Mater. Process. Technol. 2007;182:207-14.

[78] Kolobnev NI, Khokhlatova LB, Samokhvalov SV, Alekseev AA, Sbitneva SV, Tararaeva TI, et al. Heat Treatment Effect on Properties of Al-Mg-Si-Cu 1370 Alloy. Mater. Sci. Forum 2006;519 - 521:519-24.

[79] Mukhopadhyay AK, Prasad KS, Kumar V, Kamat SV. Influence of Small Additions of Sc and Ag on the Microstructure and Properties of Al Alloy 7017. In: Nie JF, Morton AJ, Muddle BC, editors. 9th International Conference on Aluminium Alloys. Brisbane, Australia: Institute of Materials Engineering Australasia Ltd; Aug. 2-5 2004. p. 793-8.

[80] Wu Y-L, Li C, Froes FH, Alvarez A. Microalloying of Sc, Ni, and Ce in an advanced Al-Zn-Mg-Cu alloy. Metall. Mater. Trans. A. 1999;30:1017-24.

[81] Fridlyander IN, Kolobnev NI, Grushko OE, Davydov VG. Advanced Weldable Damage Tolerant AlMgLi Alloy for Aircraft Application. Mater. Sci. Forum 1996;242:249-54.

[82] Sawtell R, Jensen C. Mechanical properties and microstructures of Al-Mg-Sc alloys. Metall. Mater. Trans. A. 1990;21:421-30.

[83] Doherty RD, Hughes DA, Humphreys FJ, Jonas JJ, Jensen DJ, Kassner ME, et al. Current issues in recrystallization: a review. Mater. Sci. Eng. A. 1997;238:219-74.

[84] Rollett A, Humphreys FJ, Rohrer GS. Recrystallization and Related Annealing Phenomena. Elsevier Science; 2004.

[85] Tsuji N, Ito Y, Saito Y, Minamino Y. Strength and ductility of ultrafine grained aluminum and iron produced by ARB and annealing. Scri. Mater. 2002;47:893-9.

[86] Kim H-W, Kang S-B, Tsuji N, Minamino Y. Elongation increase in ultra-fine grained Al–Fe–Si alloy sheets. Acta Mater. 2005;53:1737-49.

[87] Ocenasek V, Slamova M. Resistance to recrystallization due to Sc and Zr addition to Al–Mg alloys. Mater. Char. 2001;47:157-62.

[88] He Y-d, Zhang X-m, You J-h. Effect of minor Sc and Zr on microstructure and mechanical properties of Al-Zn-Mg-Cu alloy. Trans. Nonferrous Met. Soc. China. 2006;16:1228-35.

[89] Miura Y, Shioyama T, Hara D. Recrystallization of Al-3Mg and Al-3Mg-0.2Sc Alloys. Mater. Sci. Forum 1996;217 - 222:505-10.

[90] Ferry M, Burhan N. Structural and kinetic aspects of continuous grain coarsening in a fine-grained Al–0.3Sc alloy. Acta Mater. 2007;55:3479-91.

[91] Ferry M, Burhan N. Microstructural evolution in a fine-grained Al–0.3wt% Sc alloy produced by severe plastic deformation. Scri. Mater. 2007;56:525-8.

[92] Ferry M, Hamilton NE, Humphreys FJ. Continuous and discontinuous grain coarsening in a fine-grained particle-containing Al–Sc alloy. Acta Mater. 2005;53:1097-109.

[93] Ganiev IN. High-Temperature and Electrochemical Corrosion of Aluminum-Scandium Alloys. Protection of Metals. 1995;31 543-6.

[94] Vyazovikina NV. The Effect of Scandium on the Corrosion Resistance of Aluminum and its Alloys in 3% NaCl Solution. Protection of Metals. 1999;35 448-53.

[95] Kharina GV, Kuznetsov MV, Kochergin VP. Mechanism and kinetics of anodic dissolution of aluminum and its alloys with zinc and rare-earths in a sodium polyvanadate solution. Russ. J. Electrochem. 1998;34 482–5.

[96] Kharina GV, Kochergin VP. Corrosion of Alloys of Aluminum with Zinc and Rare Earth Metals in Sodium Metavanadate Solutions. Protection of Metals. 1996;32:134-6.

[97] Sinyavskii VS, Val'kov VD, Titkova EV. The Effect of Scandium and Zirconium Additions on Corrosion Properties of Al-Mg Alloys. Protection of Metals. 1998;34: 549-55.

[98] Ahmad Z, Ul-Hamid A, B.J A-A. The corrosion behavior of scandium alloyed Al 5052 in neutral sodium chloride solution. Corros. Sci. 2001;43:1227-43.

[99] Bhat MSN, Surappa MK, Nayak HVS. Corrosion behaviour of silicon carbide particle reinforced 6061/Al alloy composites. J. Mater. Sci. 1991;26:4991-6.

[100] Venkateswaran G, Venkateswaran KS. International Congress Metallic Corrosion. 1987. p. 1587.

[101] Cavanaugh MK, Birbilis N, Buchheit RG, Bovard F. Investigating localized corrosion susceptibility arising from Sc containing intermetallic Al3Sc in high strength Al-alloys. Scri. Mater. 2007;56:995-8.

[102] Polmear IJ. Light alloys: metallurgy of the light metals: John Wiley & Sons Australia, Limited. 1995.

[103] Zalutskaya OI, Kontseyoy VG, Karamishev NI, Ryabov VR, Zalutskii II. Dopovidi Akademii Nauk Ukr RSR. 1970:751.

[104] Palenzona A. The ytterbium-aluminum system. J Less Common Met. 1972;29:289-92.

[105] Mondolfo LF. Aluminum alloys: structure and properties London: Butterworths. 1976.

[106] JCPDS-International Centre for Diffraction Data

[107] Sawtell RR. Morris JW. Dispersion Strengthened Aluminum Alloys. Y.-W. Kim, W.M. Griffith (Eds.), T TMS Publishing. 1988;409.

[108] Sawtell RR. Exploratory alloy development in the system Al–Sc–X. PhD Thesis, University of California, Berkeley. 1988.

[109] Massalski TB, Okamoto H. Binary Alloy Phase Diagrams, ASM International. Ohio. Materials Park. 1990.

[110] van Dalen ME, Karnesky RA, Cabotaje JR, Dunand DC, Seidman DN. Erbium and ytterbium solubilities and diffusivities in aluminum as determined by nanoscale characterization of precipitates. Acta Mater. 2009;57:4081-9.

[111] van Dalen ME, Gyger T, Dunand DC, Seidman DN. Effects of Yb and Zr microalloying additions on the microstructure and mechanical properties of dilute Al–Sc alloys. Acta Mater. 2011;59:7615-26.

[112] van Dalen ME, Dunand DC, Seidman DN. Microstructural evolution and creep properties of precipitation-strengthened Al–0.06Sc–0.02Gd and Al–0.06Sc–0.02Yb (at.%) alloys. Acta Mater. 2011;59:5224-37.

[113] Krug ME, Werber A, Dunand DC, Seidman DN. Core–shell nanoscale precipitates in Al–0.06 at.% Sc microalloyed with Tb, Ho, Tm or Lu. Acta Mater. 2010;58:134-45.

[114] Knipling KE, Karnesky RA, Lee CP, Dunand DC, Seidman DN. Precipitation evolution in Al–0.1Sc, Al–0.1Zr and Al–0.1Sc–0.1Zr (at.%) alloys during isochronal aging. Acta Mater. 2010;58:5184-95.

[115] Karnesky RA, van Dalen ME, Dunand DC, Seidman DN. Effects of substituting rare-earth elements for scandium in a precipitation-strengthened Al–0.08 at. %Sc alloy. Scri. Mater. 2006;55:437-40.

[116] Dalen ME, Dunand DC, Seidman DN. Nanoscale precipitation and mechanical properties of Al-0.06 at.% Sc alloys microalloyed with Yb or Gd. J. Mater. Sci. 2006;41:7814-23.

[117] Karnesky RA, van Dalen ME, Dunand DC, Seidman DN. Effects of substituting rare-earth elements for scandium in a precipitation-strengthened Al–0.0 at. %Sc alloy. Scri. Mater. 2006;55:437-40.

[118] Murarka SP, Agarwala RP. Govt of India Atomic Energy Commun 1968.

[119] Costa S, Puga H, Barbosa J, Pinto AMP. The effect of Sc additions on the microstructure and age hardening behaviour of as cast Al–Sc alloys. Mater. Des.. 2012;42:347-52.

[120] Kaiser MS, Datta S, Roychowdhury A, Banerjee MK. Effect of scandium on the microstructure and ageing behaviour of cast Al–6Mg alloy. Mater. Charact. 2008;59:1661-6.

[121] Lathabai S, Lloyd PG. The effect of scandium on the microstructure, mechanical properties and weldability of a cast Al–Mg alloy. Acta Mater. 2002;50:4275-92.

[122] Patakham U, Kajornchaiyakul J, Limmaneevichitr C. Grain refinement mechanism in an Al–Si–Mg alloy with scandium. Journal of Alloys and Compounds. 2012;542:177-86.

[123] Venkateswarlu K, Pathak LC, Ray AK, Das G, Verma PK, Kumar M, et al. Microstructure, tensile strength and wear behaviour of Al–Sc alloy. Mater. Sci. Eng. A. 2004;383:374-80.

[124] Zakharov VV. Effect of Scandium on the Structure and Properties of Aluminum Alloys. Met. Sci. Heat Treat. 2003;45:246-53.

[125] Zhang WG, Ye YC, He LJ, Li PJ, Feng X, Novikov LS. Dynamic response and microstructure control of Al–Sc binary alloy under high-speed impact. Mater. Sci. Eng. A. 2013;578:35-45.

[126] Fasoyinu FA, Thomson J, Cousineau D, Castles T, Sahoo M. Grain Refinement and Thermal Analysis of Al-Mg Alloy 535. 6th International AFS Conference on Molten Aluminum Processing. 2001:20.

[127] Yin Z, Pan Q, Zhang Y, Jiang F. Effect of minor Sc and Zr on the microstructure and mechanical properties of Al-Mg based alloys. Mater. Sci. Eng. A. 2000;280:151-5.

[128] Cibula A. The mechanism of grain refinement of sand casting in aluminium alloys. J. of the Institute of Metals. 1949-1950;76:321-60.

[129] Delamore GW, Smith RW. The mechanisms of grain refinement in dilute aluminum alloys. Metall. Trans. 1971;2:1733-8.

[130] Antonio JAM, Lfo LFM. Grain refinement in aluminum alloyed with titanium and boron. Metall. Trans. 1971;2:465-71.

[131] Sigworth G. The Grain Refining of Aluminum and Phase Relationships in the Al-Ti-B System. Metall and Mat Trans A. 1984;15:277-82.

[132] Jones GP, Pearson J. Factors affecting the grain-refinement of aluminum using titanium and boron additives. Metall. Trans. B. 1976;7:223-34.

[133] Sigworth G. Author's reply. Metall and Mat Trans A. 1986;17:349-51.

[134] Johnsson M, Baeckerud L. The influence of composition on equiaxed crystal growth mechanisms and grain size in Al alloys. Z. Metallkd. 1996;87:216-20.

[135] Backerud L, Gustafson P, Johnsson M. Grain refining mechanisms in aluminium as a result of additions of titanium and boron. Aluminium. 1991;67:910-5.

[136] Vader M, Noordegraaf J. The effectiveness of a grain refiner reinforced by a built-in energy content. j. Light Met. 1990:85-857.

[137] Easton M, StJohn D. Grain refinement of aluminum alloys: Part I. the nucleant and solute paradigms—a review of the literature. Metall. Mater. Trans. A. 1999;30:1613-23.

[138] Johnsson M, Baeckerud L. Nucleants in grain refined aluminium after addition of Ti- and B-containing master alloys. Z. Metallkd. 1992;83:774-80.

[139] Jones GP. Solidification Processing. The Institute of Metals, London1987.

[140] Mohanty PS, Samuel FH, Gruzleski JE. Studies on addition of inclusions to molten aluminum using a novel technique. Metall. Mater. Trans. B. 1995;26:103-9.

[141] Schumacher P, Greer AL. Heterogeneously nucleated α-Al in amorphous aluminium alloys. Mater. Sci. Eng. A. 1994;178:309-13.

[142] Schumacher P, Greer AL. Enhanced heterogeneous nucleation of α-Al in amorphous aluminium alloys. Mater. Sci. Eng. A. 1994;181–182:1335-9.

[143] Johnsson M, Backerud L, Sigworth G. Study of the mechanism of grain refinement of aluminum after additions of Ti- and B-containing master alloys. Metall and Mat Trans A. 1993;24:481-91.

[144] Greer AL, Bunn AM, Tronche A, Evans PV, Bristow DJ. Modelling of inoculation of metallic melts: application to grain refinement of aluminium by Al–Ti–B. Acta Mater. 2000;48:2823-35.

[145] McCartney DG. Grain refining of aluminium and its alloys using inoculants. Int. Mat. Rev. 1989;34:247-60.

[146] Maxwell I, Hellawell A. A simple model for grain refinement during solidification. Acta Metall. 1975;23:229-37.

[147] Eskin GI. Ultrasonic Treatment of Light Alloy Melts. Gordon and Breach Science Publishers; 1998.

[148] Li YL, Feng HK, Cao FR, Chen YB, Gong LY. Effect of high density ultrasonic on the microstructure and refining property of Al–5Ti–0.25C grain refiner alloy. Mater. Sci. Eng. A. 2008;487:518-23.

[149] Easton MA, StJohn DH. A model of grain refinement incorporating alloy constitution and potency of heterogeneous nucleant particles. Acta Mater. 2001;49:1867-78.

[150] Hunt JD, Jackson KA. Nucleation of Solid in an Undercooled Liquid by Cavitation. J. Appl. Phys. 1966;37:254-7.

[151] Jian X, Meek TT, Han Q. Refinement of eutectic silicon phase of aluminum A356 alloy using high-intensity ultrasonic vibration. Scri. Mater. 2006;54:893-6.

[152] Abramov OV. Ultrasound in liquid and solid metals: CRC Press; 1994.

[153] Eskin GI. Influence of cavitation treatment of melts on the processes of nucleation and growth of crystals during solidification of ingots and castings from light alloys. Ultrason. Sonochem. 1994;1:S59-S63.

[154] Qian M, Ramirez A, Das A. Ultrasonic refinement of magnesium by cavitation: Clarifying the role of wall crystals. J. Cryst. Growth. 2009;311:3708-15.

CHAPTER 2 - EXPERIMENTAL PROCEDURES

Chapter 2 – Experimental Procedures

The following chart (Figure 2.1) outlines the experimental procedures of research.

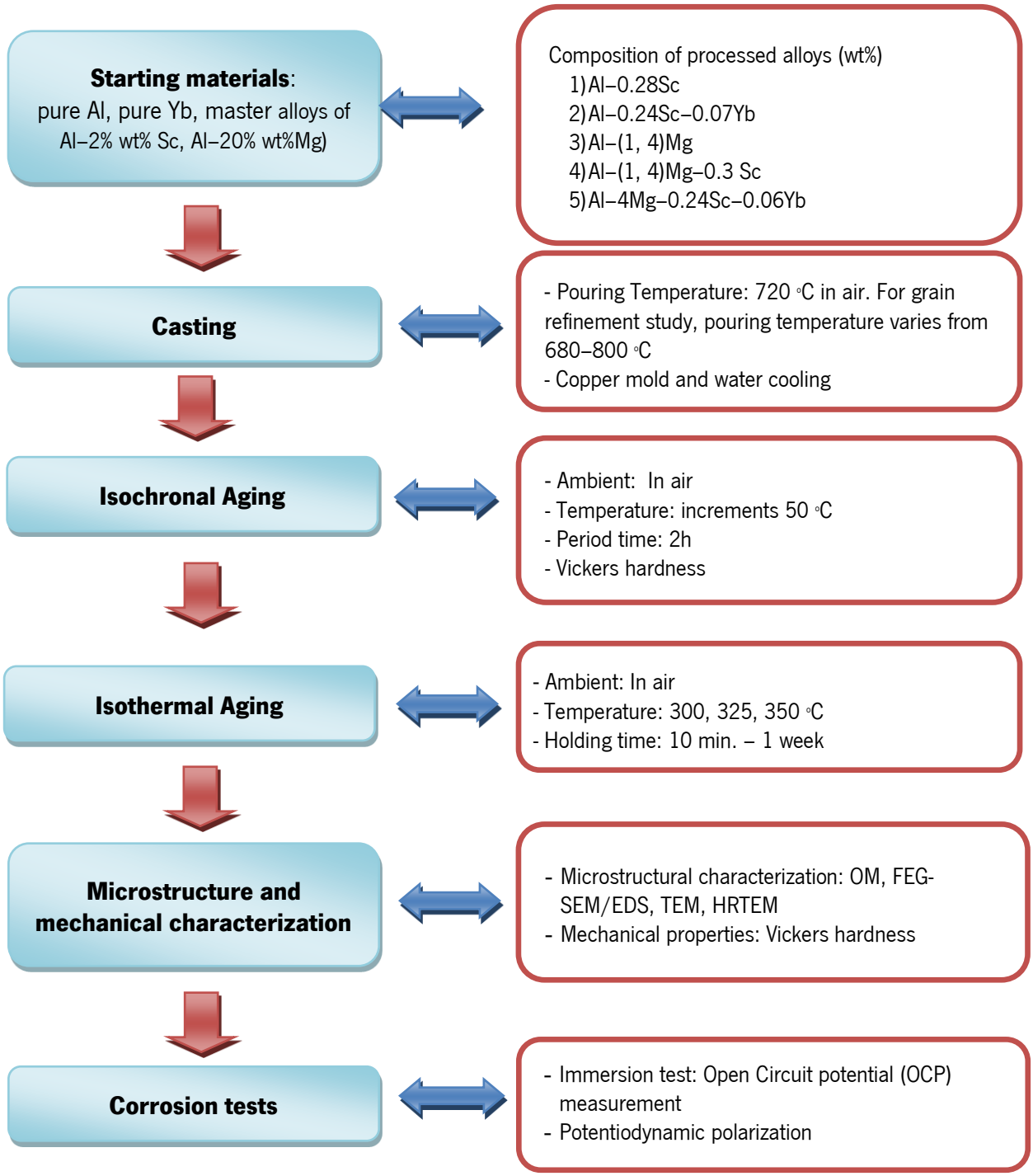

Figure 2.1. Outline of the research experimental procedure.

2.1 Alloys processing

2.1.1 Al–Sc and Al–Sc–Yb alloys

Al–0.28Sc and Al–0.24Sc–0.07Yb (wt%) alloys were cast by using commercially pure Al (99.83 wt% purity), Al–2 wt% Sc master alloy and pure Yb (99.99 wt% purity). The alloys were melted in a graphite crucible using a high frequency induction furnace. For each alloy, pure Al was firstly melted at 720 °C ± 5. Then the Al–2 wt% Sc master alloy and pure Yb were added into the melt. The melt was kept at this temperature for 30 minutes and stirred with an alumina rod to ensure homogeneity. The molten alloys were poured into cylindrical copper moulds with 16 mm in diameter and 80 mm in length and water cooled. All the ingots were cut into several samples with size of 16 mm in diameter and 6 mm in length. Position of the analysed sections on the sample was shown in Figure 2.2. Samples from the centre of each ingot were used for microstructure characterization.

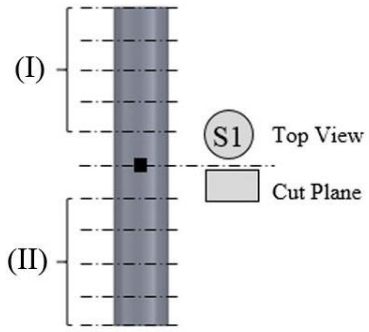

Figure 2.2. Position of the analysed sections on the sample.

The composition of the as-cast alloy was measured by X-ray Fluorescence Spectrometery (Bruker S8 Tiger). The chemical composition of the as-cast alloys is given in Table 2.1.

Table 2.1. Chemical composition of the Al–0.28Sc and Al–0.24Sc–0.07Yb as-cast alloys

Alloy		Sc	Yb	Si	Fe	Ni	Cu	Ba	Mn	Ti	Al
Al–Sc	wt%	0.283	-	0.383	0.130	0.010	0.007	0.060	0.010	0.009	Bal
	at%	0.170		0.369	0.063	0.005	0.003	0.012	0.005	0.005	Bal
Al–Sc–Yb	wt%	0.243	0.068	0.328	0.208	0.040	0.032	0.015	-	-	Bal
	at%	0.146	0.011	0.316	0.101	0.018	0.014	0.003	-	-	Bal

2.1.2 Al–Mg–Sc and Al–Mg–Sc–Yb alloys

Al–4Mg, Al–4Mg–0.3Sc, and Al–4Mg–0.24Sc–0.06Yb (wt%) alloys were cast by using commercially pure Al (99.83 wt% purity), Al–2 wt% Sc and Al–20 wt% Mg master alloys as melting stock. The proper weights of these starting materials were melted in an electrical resistance furnace equipped with a SiC crucible. For each alloy pure Al was firstly melted at 800 ± 5 °C followed by addition of the master alloys. The melt was kept at this temperature for 30 minutes and stirred with an alumina rod to ensure homogeneity. The melt was then cooled down and poured at 720 ± 5 °C. Before pouring, the melt was degassed by argon gas purging. Casting was carried out in the same copper mould above and immediately cooled to room temperature by immersion into water. The composition of the as-cast alloy was measured by X–ray spectrometer (X'Unique II, Philips). The chemical compositions of the as-cast alloys are given in Table 2.2.

Table 2.2 – Chemical composition of Al–4Mg, Al–4Mg–0.3Sc, and Al–4Mg–0.24Sc–0.06Yb as-cast alloys (wt%)

Alloy	Mg	Sc	Yb	Si	Fe	Cu	Zn	Cr	Mn	Ti	Al
Al–4Mg	3.93	-	-	0.128	0.228	0.024	0.015	-	0.008	-	Bal
Al–4Mg–0.3Sc	3.86	0.291	-	0.15	0.325	0.031	0.018	0.03	-	0.011	Bal
Al–4Mg–0.24Sc–0.06Yb	3.91	0.235	0.071	0.177	0.358	0.029	0.023	0.022	0.012	0.007	Bal

2.1.3 Casting for grain refinement study

Step 1: In order to study the effect of Mg and Sc on grain refinement of Al–Mg–Sc alloys, Al–1Mg, Al–4Mg, Al–0.3Sc, Al-1Mg-0.3Sc and Al–4Mg–0.3Sc (wt%) alloys were cast by using commercially pure Al (99.83 wt% purity), Al–2 wt% Sc and Al–20 wt% Mg master alloys as melting stock. The casting in this step was performed by the same procedure referred in Section 2.1.2. The different thing is pouring temperature which was 700 ± 5 °C.

Step 2: The effect of pouring temperature on grain refinement of Al–1Mg–0.3Sc (wt%) alloy was performed. Al–1Mg–0.3Sc alloys were prepared by the same procedure referred above (Step 1) and poured at different temperatures ranging from 680 ± 5 °C to 800 ± 5 °C.

Step 3: In step, the effect of ultrasonic treatment on grain refinement of Al–1Mg–0.3Sc (wt%) alloy at a wide range of pouring temperatures was evaluated. The experimental set-up (Figure 2.3) used in this work consisted of a novel MMM (Multi-frequency, Multimode, Modulated technology) ultrasonic power supply

unit, a high power ultrasonic converter (1200W), a 30mm diameter and 150mm long acoustic waveguide and the acoustic load itself which consists on a 20mm diameter and 75mm long Nb acoustic radiator and the melt.

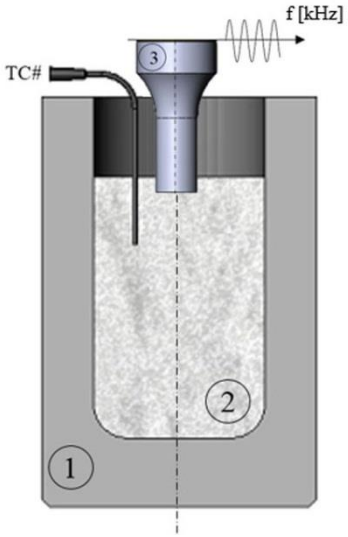

Figure 2.3. Schematic representation of the experimental setup used in the experiments ((1) SiC Crucible, (2) the melt and (3) Acoustic radiator).

Melting stocks of Al–1Mg–0.3Sc consisted of commercially pure Al (99.83 wt% purity), Al–2 wt% Sc and Al–20 wt% Mg master alloys. Suitable masses of these starting materials were melted in a SiC crucible, using an electrical resistance furnace. For each alloy, pure Al was firstly melted at 800 ± 5 ◦C. Then the master alloys were added into the melt. The melt was kept at this temperature for 30 minutes and stirred with an alumina rod to ensure homogeneity. The melt was cooled down to different temperatures ranging from 800 ± 5 ◦C to 700 ± 5 ◦C and the sonotrode was preheating to avoid a drop in temperature of the melt when applying ultrasonic vibration. Ultrasonic frequency of 20.3 ± 0.25 kHz at electric power of 30 % for 30 s was applied for each processing condition. After ultrasonic treatment, the molten alloy was poured into a copper mould and immediately cooled to ambient temperature by immersion in water.

2.2 Heat treatments

Samples for this step were taken from section I and II (Figure 2.2).

The effect of homogenization treatment and aging temperature on precipitation behaviour and age hardening response of Al–0.28Sc and Al–0.24Sc–0.07Yb was investigated. Two separate studies were conducted: in one, the as-cast alloys were treated at 640 ◦C for 72 h for homogenization and water quenched to room temperature. The samples were subsequently treated at various temperatures within the

range 150 to 375 °C for 2 h, followed by water quenching to ambient room temperature; in the other, the same procedure without homogenization treatment was carried out.

In order to evaluate the aging kinetics of Al–Sc, Al–Sc–Yb, Al–Mg–Sc, and Al–Mg–Sc–Yb alloys, isothermal aging without homogenization treatment of the cast samples was carried out. The samples were aged at different temperatures between 300 and 350 °C for times ranging from 10 minutes to 7 days.

Vickers hardness was used to monitor the hardening behaviour. Vickers hardness measurements were performed at room temperature using 30 kg load and 20 second dwell time. Eight measurements were performed on each sample.

2.3 Microstructural characterization of the alloys

Several techniques were used to characterize the microstructure of the alloys. Prior for all analysis the sample were metallographic prepared,

2.3.1 Optical microscopy and scanning electron microscopy

Samples for microstructural characterization were taken from each cast sample by sectioning them perpendicularly to its longitudinal axis (S1 in Figure 2.2). The samples were ground with SiC paper, polished down using non-crystallizing colloidal silica suspension.

For optical microscopy analysis the samples were anodised at a voltage of 30 V in a 2.5 % aqueous solution of fluoroboric acid (HBF_4) to reveal grain size. The overall microstructure morphology was analysed by optical microscopy using a Leica DM 2500 M and Image-Pro Plus software was used to quantify the average grain size and grain size distribution.

Scanning electron microscopy (SEM) and Energy Dispersive Spectroscopy (EDS) analysis were done to the as-cast alloys as well as to homogenised alloys in a FEG-SEM equipment (Nano-SEM-FEI Nova 200/EDAX–Pegasus X4 M).

2.3.2 Transmission electron microscopy and high resolution electron microscopy

Transmission electron microscopy (TEM) and high resolution electron microscope (HRTEM) were used to determine the structure, distribution and morphological characteristics of the precipitates. Discs of 3 mm diameter were prepared and mechanically ground to 100 μm. The foils were prepared by double-jet electropolishing in a solution of 25% nitric acid and 75% methanol solution. The specimens were examined by FEI TECNAI G20 or JEOL JEM-2200FS operating at 200 kV. Thin foils for TEM and HRTEM observations were sectioned from the alloys under different conditions.

In order to determine the average diameter and evaluate the number of precipitates, the TEM micrographs were analysed by Image J software. For each condition, four TEM micrographs at various positions of sample with more than 200 precipitates were selected to measure the precipitate size. Image-Pro Plus software was used to quantify precipitates size distribution. Gatan Digital Micrograph software was used to analyse HRTEM images.

2.4 Electrochemical tests

Prior to the electrochemical tests the samples were polished with colloidal silica (0.3 μm) and cleaned ultrasonically 10 min in propanol followed by 5 min in distilled water. The electrochemical tests consisted in open circuit potential (OCP) and potentiodynamic polarisation tests. All electrochemical tests were performed using a conventional three-electrode electrochemical cell adapted from ASTM standard practice G3-89[1], where 3.5 wt% NaCl (sea water) was used as the electrolyte. A saturated calomel electrode (SCE) used as the reference electrode, Pt electrode used as the counter electrode, and the samples used as the working electrode, having an exposure area of 0.07 cm^2. All potentials are given with respect to SCE. All electrochemical tests were performed by using a Gamry Instruments Reference 600™ Potentiostat controlled by the Gamry Instruments Framwork™ software (Gamry Instruments, Warminster, PA, USA).

The immersion tests were performed during 96 h (4 days). OCP was measured just after immersion during 30 min and after that, for 15 min during the following each 4 days. Potentiodynamic polarisation measurements started from a cathodic potential of −1.5 V up to the anodic domain (O V vs. SCE) with a scan rate of 0.5 mV/s. The samples after electrochemical tests were ultrasonically cleaned in hot water to remove the corrosion products. Each test was repeated at least three times and the average value of corrosion potential (E_{corr}), pitting potential (E_p), corrosion current density (i_{corr}) were determined by using the software program Gamry Echem Analyst (Version 5.61). The i_{corr} and E_{corr} ($E_{(i=0)}$) were determined by extrapolation of the Tafel lines of each polarisation curve.

[1] ASTM Standard G3–89, Standard Practice for Conventions Applicable to Electrochemical Measurements in Corrosion Testing. West Conshohocken, PA: ASTM International; 1999

CHAPTER 3 - EFFECT OF Yb SUBSTITUTING FOR Sc ON THE MICROSTRUCTURE AND AGE-HARDENINGBEHAVIOUR OF Al–Sc ALLOY

The work presented in this chapter was based on the published paper: **N.Q. Tuan**, A.M.P. Pinto, H. Puga, L.A. Rocha, J. Barbosa, Materials Science &Engineering A, 601, (2014), 70-77, http//dx.doi.org/10.1016/j.msea.2014.02.042

Chapter 3 – Effect of substituting Yb for Sc on the microstructure and age-hardening behaviour of Al-Sc alloys

Introduction

Al–Sc alloys have excellent mechanical properties at ambient and elevated temperatures due to the presence of a high number density (as high as 10^{22} m^{-3}) of elastically-hard Al_3Sc ($L1_2$ structure) precipitates [1-4]. The Al_3Sc precipitates remain fully coherent with the α–Al matrix at elevated temperatures [1,5]. Among alloying elements of Al alloys, Sc has one of the greatest strengthening effect on a per-atom basis [6]. The Al_3Sc precipitates are very stable with respect to coarsening, even for long aging times at 350 °C [1], while in commercial age-hardening 2xxx and 6xxx series alloys containing Cu, Mg and Si, the precipitates coarsen rapidly at temperatures above 250 °C [6]. At ambient temperature the lattice parameters of Al and Al_3Sc are 0.40496 and 0.4105 nm, respectively, showing a small lattice parameter mismatch of Al_3Sc precipitates with the α–Al matrix [7-9]. A good interfacial strength between the Al_3Sc precipitates and the α–Al matrix will hinder dislocation motion and prevent grain growth [10]. In addition, the high thermal stability of the Al_3Sc precipitates will improve the strength of these alloys at high temperature [11,12]. Therefore Al–Sc alloys are widely used in the fabrication of sports equipment, aerospace components and in a range of structural applications.

Although Al–Sc alloys are very attractive, their use is limited by the cost and availability of Sc. A possible solution for this problem could be replacing part of the Sc by other alloying elements similar in nature in order to reduce the Sc content without decreasing properties. Among them, REMs are attractive ternary additions to substitute Sc. Karnesky *et al.* [13] showed that the Vickers hardness of Al–0.06 at% Sc–0.02 at% REM alloys (REM = Dy, Er, Gd, Sm, Y, or Yb) aging at 300°C are generally similar to that of Al–0.08 at% Sc alloy. The Al–0.06 at% Sc alloys microalloyed with Yb or Gd have much improved creep resistance when compared to binary Al–Sc or ternary Al–Sc–Zr alloys with the same composition and precipitate radius [14]. According to Sawtell and Morris [15,16], addition of 0.3 at% Er, Gd, Ho, or Y improves the tensile strength of Al–0.3 at% Sc alloys at room temperature.

In this chapter, the microstructure and mechanical properties of Al–0.24Sc–0.07Yb in comparison with Al–0.28Sc alloys were presented. The aging behaviour, precipitate morphologies, precipitate coarsening and precipitation hardening of both alloys were discussed. The average diameter and the size distribution of nanoscale Al_3Sc and $Al_3(Sc,Yb)$ precipitates at various aging conditions were measured. TEM and HRTEM were used to understand the precipitate evolution.

3.1 Results and discussion

3.1.1 Age Hardening Behaviour of the as-cast Alloys

3.1.1.1 Effect of homogenization treatment and aging temperatures on ageing behaviour

The Vickers hardness curves of Al–0.28Sc and Al–0.24Sc–0.07Yb alloys aged at various temperatures within the range 150 to 375 ◦C for 2 h with and without homogenization treatment are shown in Figure 3.1. It is evident that the hardness values of the alloys aged in the as-cast condition are significantly higher than those of the alloys homogenized and aged. In the as-cast alloys, Sc and Yb exist in α–Al supersaturated solid solution due to the high cooling rate during solidification. The precipitation of intermetallic particles occurs during the homogenization treatment, reducing the supersaturation level of Sc and Yb in α–Al solid solution. As a consequence, homogenized alloys will have the lower hardening effect due to the lower fraction volume/density of precipitates. Figure 3.2 shows SEM micrographs of as-cast and homogenized Al–0.24Sc–0.07Yb samples. In the homogenized samples, several large particles of intermetallic precipitates were formed and heterogeneously distributed in α–Al.

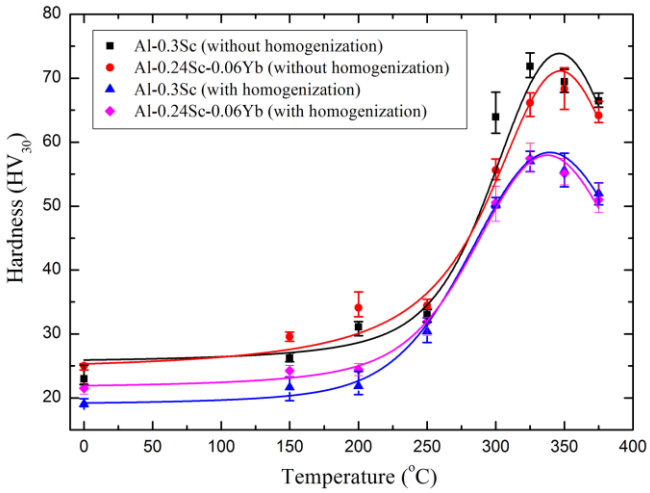

Figure 3.1. Vickers hardness curves of Al–0.28Sc, Al–0.24Sc–0.07Yb alloys at various aging temperatures with and without previous homogenization treatment.

Also shown in Figure 3.1 is the effect of substituting 0.07Yb for Sc of Al–0.28Sc alloy on aging behaviour at various temperatures. The onset of age hardening for both alloys occurs at 200 ◦C. The precipitates form most rapidly at the temperature range of 300-350 °C, for which the highest hardness values were obtained. In the aging process without homogenization treatment, the Vickers hardness value peaks of Al–0.28Sc and Al–0.24Sc–0.07Yb alloys are 72 HV at 325 ◦C and 68 HV at 350 ◦C, respectively. A decreasing in Vickers hardness is observed for both alloys for temperatures higher than 375 ◦C due to the

precipitate coarsening. The results showed that the partial replacement of Sc by Yb did not significantly affect either the kinetics or the peak hardness. Karnesky *et al.* [17] reported similar effect of Yb on the hardening response of an Al-0.08 at% Sc based alloy.

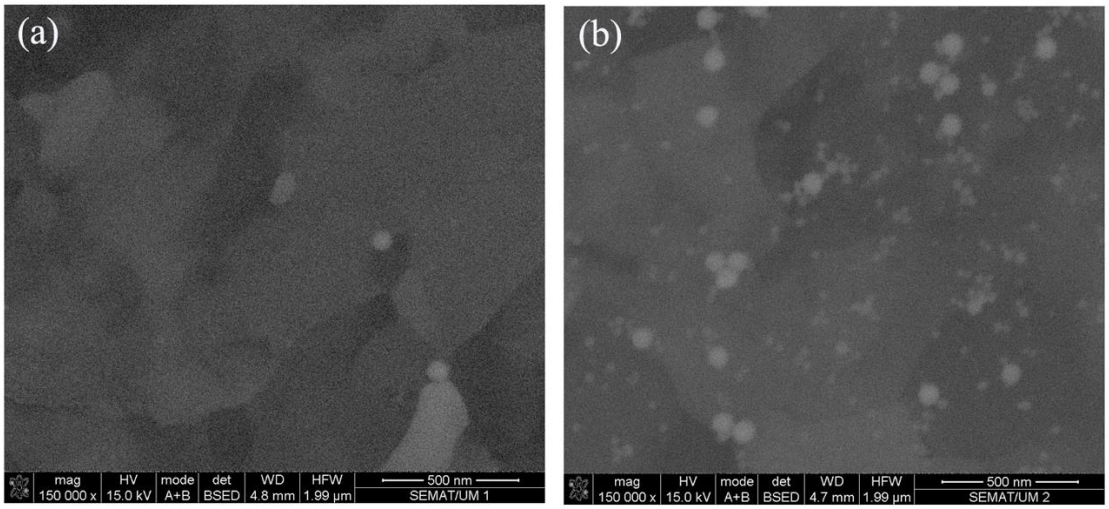

Figure 3.2. SEM micrographs of Al–0.24Sc–0.07Yb alloy: (a) as-cast and (b) homogenization treated.

The alloys used in this work present in their composition small contents of other elements, namely Si and Fe that may have some small influence on the alloys mechanical properties, namely hardness. Nevertheless, the difference between both alloys is very small, suggesting that the relative hardness values have not been influenced by the presence of those elements.

3.1.1.2 Isothermal aging behaviour

The age hardening behaviour of Al–0.28Sc and Al–0.24Sc–0.07Yb alloys at aging temperatures of 300, 325 and 350 °C is shown in Figure 3.3. It is quite evident that the Al–0.24Sc–0.07Yb alloy shows the similarity of Vickers hardness and aging behaviour with the Al–0.28Sc alloy. All the curves exhibits four different regions: (a) an incubation period; (b) a period with a rapid increase in hardness values where the precipitates nucleate from a supersaturated solid solution and grow; (c) a period of maximum hardness values (peak aging); and (d) over-aging, characterized by a slow decrease in hardness by the precipitates coarsening. The time to reach the hardness value peak decreases when the aging temperature increases from 300 to 350 °C. The Al–0.28Sc and Al–0.24Sc–0.07Yb alloys reach the hardness value peak after 20, 5, and 1 h when aging at 300, 325, and 350 °C, respectively. Higher temperature leads to earlier occurrence of over-aging. In Figure 3.3(a), there is no significantly softening due to over-aging for both alloys aged at 300 °C after 7 days. However, Figure 3.3 (b) and (c) show a fast over-aging for both alloys

aged at 325 and 350 °C. At these aging temperatures, the hardness drop becomes obviously after reaching the peak values. Higher aging temperature conducts to higher diffusion rate for precipitates nucleation and growth. It accelerates the over-aging stage.

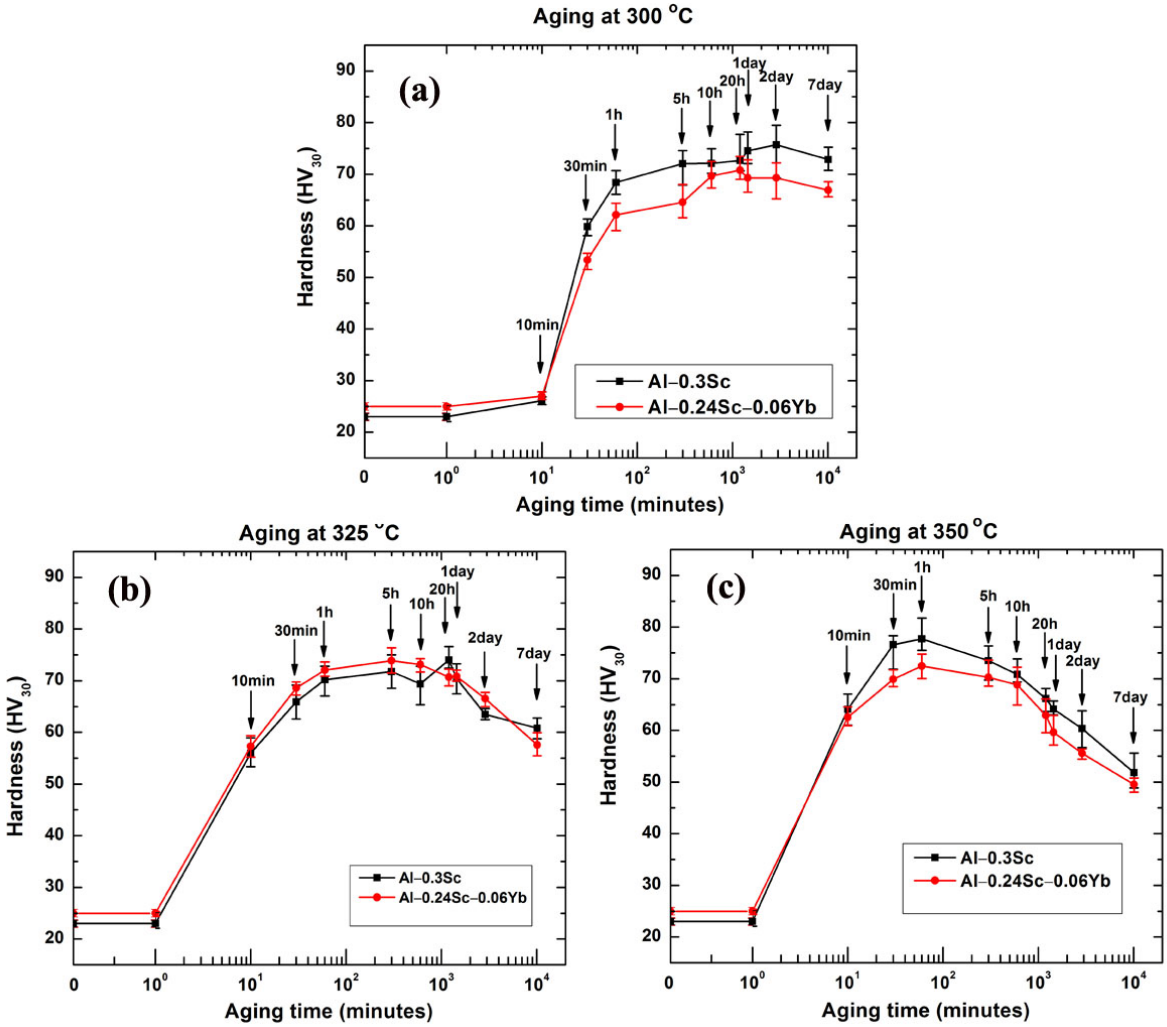

Figure 3.3. Isothermal ageing curves of Al–0.28Sc and Al–0.24Sc–0.07Yb alloys at: (a) 300 ◦C; (b) 325 ◦C; (c) 350 ◦C.

3.1.2 Evolution of precipitates

3.1.2.1 Precipitate morphologies

The aging behaviour presented above is controlled by the alloys microstructure. In order to correlate the observed hardening with microstructures, TEM and HRTEM observations were performed on samples at different processing states to reveal the evolution of the precipitates.

The TEM micrographs of Al–0.28Sc and Al–0.24Sc–0.07Yb alloys aged at 325 ◦C for 5 h, 325 ◦C for 7 days, and 350 ◦C for 7 days are shown in Figure 3.4, respectively.

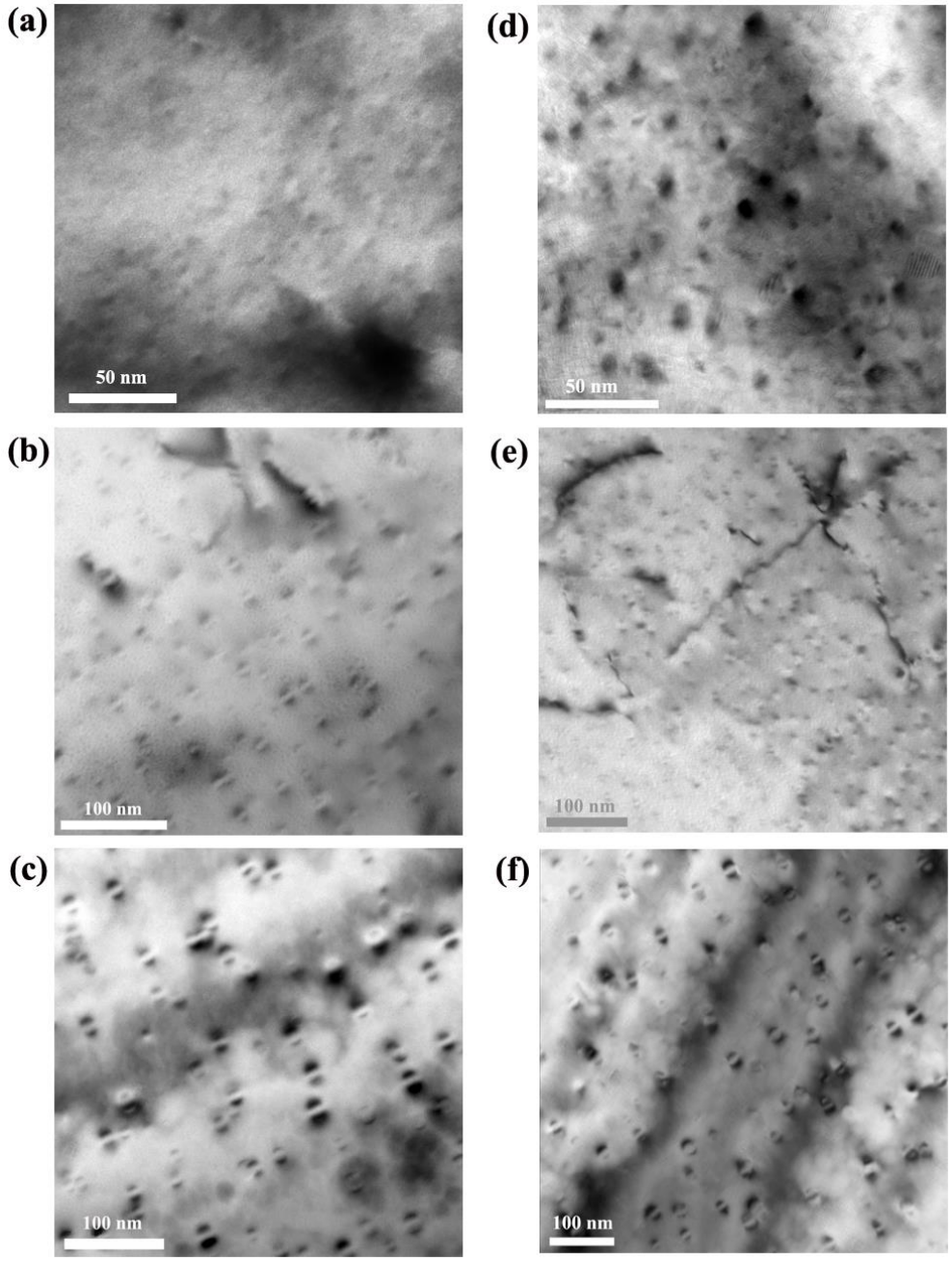

Figure 3.4. TEM micrographs of Al–0.28Sc (a–b–c) and Al–0.24Sc–0.07Yb (d–e–f) alloys aged at 325 ◦C for 5 h, 325 ◦C for 7 days, and 350 ◦C for 7 days.

In order to observe more clearly the morphology of precipitates, higher magnification of TEM micrographs with bright-field and dark-field techniques are exhibited in Figure 3.5. The micrographs show the approximately spheroidal Al_3Sc and $Al_3(Sc,Yb)$ precipitates, uniformly distributed throughout the α–Al matrix.

The $Al_3(Sc,Yb)$ precipitates in Al–0.24Sc–0.07Yb alloy could be Al_3Sc, $Al_3(Sc_{1-x}Yb_x)$ (Sc-rich composition), $Al_3(Yb_{1-x}Sc_x)$ (Yb-rich composition), or Al_3Yb precipitates. There are no signs of coherency loss that can be observed in Figure 3.4 and Figure 3.5. The precipitates in both alloys aged at the higher temperature (350 °C) for long holding time (7 days) still remain coherent with α–Al matrix.

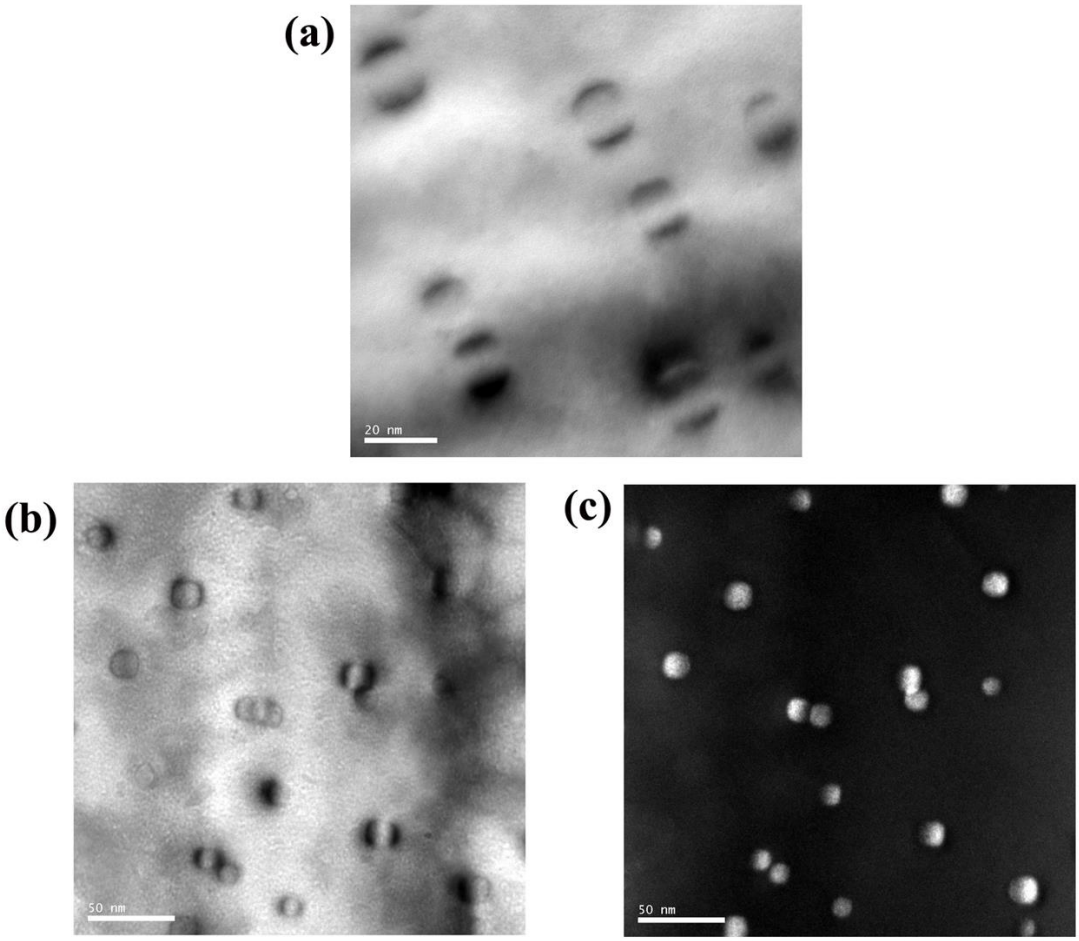

Figure 3.5. TEM micrographs of Al–0.28Sc (a) and Al–0.24Sc–0.07Yb (b–c) alloys aged at 350 °C for 7 days: (a), (b) bright-field TEM image; and (c) dark-field TEM image.

The precipitate diameter of both alloys at the different aging conditions was measured and the corresponding results are presented in Table 3.1. After aging at 300°C for 7 days the average diameter of Al_3Sc precipitate is 5.6 nm and that of $Al_3(Sc,Yb)$ precipitate is 5.9 nm. The presence of very small precipitates after long aging time indicates that coarsening occurred very slowly at 300 °C. In combination with hardness results presented in section 3.2, it can be seen that the strongest hardening effects of both alloys was achieved at aging temperature of 300 °C. When alloys were aged at 325 °C, the average

diameter is 4.3 nm for the Al_3Sc precipitate and 4.5 nm for the $Al_3(Sc,Yb)$ precipitates at the aging peak. With prolonged aging times, after 7 days the average diameter of Al_3Sc and $Al_3(Sc,Yb)$ precipitates slowly increase to 8.4 and 8.8 nm, respectively. At the temperature of 350 °C and 7 days aging, the average diameter of Al_3Sc and $Al_3(Sc,Yb)$ precipitates are 13.7 and 15.4 nm, respectively. The TEM images show a smaller number of larger size precipitates due to the coarsening process. The average precipitates size of Al–0.24Sc–0.07Yb alloy is slightly higher than that of Al–0.28Sc alloys for all aging conditions. Thus, it suggests that Yb did not affect the coarsening rate of Al–Sc alloy.

Table 3.1. Average precipitate diameter and hardness of Al–0.28Sc and Al–0.24Sc–0.07Yb alloys

Aging condition	Al–0.28Sc		Al–0.24Sc–0.07Yb	
	Precipitate diameter (nm)	Hardness (HV_{30})	Precipitate diameter (nm)	Hardness (HV_{30})
300 °C , 7 days	5.6 ± 0.5	73 ± 2	5.9 ± 0.7	67 ± 2
325 °C, 5h	4.3 ± 0.2	72 ± 3	4.5 ± 0.8	74 ± 3
325 °C, 7 days	8.4 ± 0.9	61 ± 2	8.8 ± 1.8	58 ± 2
350 °C, 7 days	13.7 ± 1.9	52 ± 3	15.4 ± 1.8	50 ± 1

The precipitates size distribution (PSDs) of Al–0.28Sc and Al–0.24Sc–0.07Yb alloys aged at 325 °C and 350 °C for 7 days is illustrated in Figure 3.6. The PSDs of Al–0.28Sc aged at 325 °C for 7 days showed more narrow width in comparison with Al–0.24Sc–0.07Yb alloys at the same aging condition. The precipitates diameter ranges of Al–0.28Sc and Al–0.24Sc–0.07Yb alloys are 7–10.5 and 5–12 nm, respectively. The PSDs of both alloys aged at 350 °C for 7 days exhibited a similar width. The precipitates diameter ranges of Al–0.28Sc and Al–0.24Sc–0.07Yb alloys at this aging condition are 10–18 and 12–20 nm, respectively.

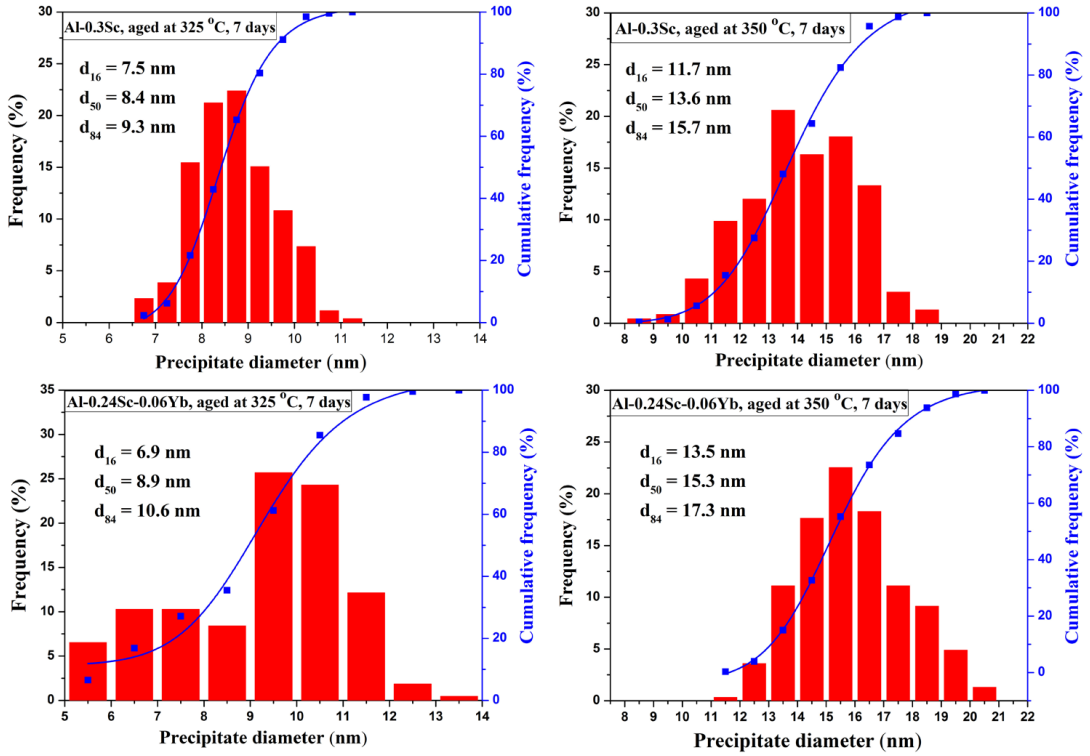

Figure 3.6. Precipitates size distribution of Al–0.28Sc and Al–0.24Sc–0.07Yb alloys at different aging conditions: d_{16}, d_{50}, and d_{84} are the precipitate diameters corresponding to 16, 50, and 84 % cumulative undersize particle size distribution.

Precipitates in Al–0.28Sc and Al–0.24Sc–0.07Yb alloys at aging peak and the most coarsened stage were studied by HRTEM technique. The HRTEM images of both alloys aged at 325 ◦C for 5 h and 350 ◦C for 7 days are shown in Figure 3.7. Through fast Fourier transform (FFT) analysis, the [011] zone axis orientation was found to fit well to the simulation of the reciprocal lattice section at the orientation. The FFT images show the reflections from (100) and $(0\bar{1}1)$ of Ll_2 Al_3Sc and $Al_3(Sc,Yb)$ precipitates and the reflections from (200), $(0\bar{2}2)$, and $(1\bar{1}1)$ of α–Al. The interface between the precipitates and the α–Al matrix remained coherent in both alloys even after aging at 350 ◦C for 7 days. There are no interfacial misfit dislocations in the HRTEM images, which conducts fully coherency of precipitates. Figure 3.7(a, b) shows the precipitates morphology of Al–0.28Sc and Al–0.24Sc–0.07Yb alloys aged at 325 ◦C for 5 h. The images show small precipitates with diameter less than 5 nm. The larger size and more obvious morphologies of precipitates are observed in Figure 3.7(c, d) corresponding to both alloys aged at 350 ◦C for 7 days. The Al_3Sc precipitates in Al–0.28Sc alloy have a facetted shape that corresponds to a great rhombicuboctahedron predicted by Marquis *et al.* [1]. Facets are parallel to the {100} and $\{0\bar{1}1\}$ planes. The precipitates average diameter is 18.1 nm, while the $Al_3(Sc,Yb)$ precipitate in Al–0.24Sc–0.07Yb alloy

exhibits an approximately spheroidal shape with 18.5 nm diameter. The presence of Yb decreases the amount of faceting parallel to the {100} and $\{0\bar{1}1\}$ and changes the morphology of precipitates into a more spheroidal shape.

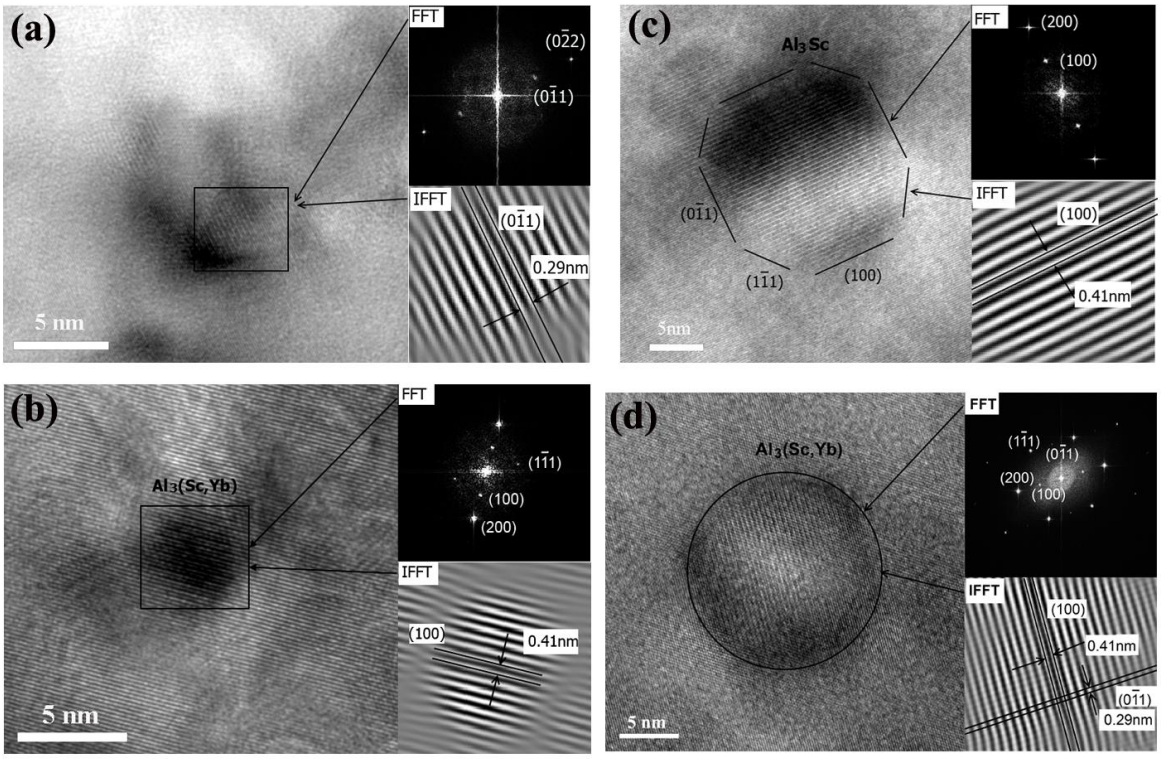

Figure 3.7. High-resolution TEM images of Al–0.28Sc (a–c) and Al–0.24Sc–0.07Yb (b–d) alloys aged at 325 ◦C for 5 h and 350 ◦C for 7 days.

The equilibrium morphology of the precipitate is achieved by minimizing the sum of the interface energy and the elastic strain energy at constant volume [17,18]. The interface energy is caused by the existence of precipitate–matrix interfaces and the elastic strain energy is due to the lattice misfit between the precipitate and matrix. The relative contribution of the elastic strain and interfacial energies is evaluated using the parameter L given by Thompson *et al.* [18] according to the following equation:

$$L = \frac{\varepsilon^2 C_{44} l}{\sigma}$$

where ε is the precipitate–matrix lattice parameter mismatch, C_{44} is an elastic constant of the matrix, l is the measured precipitate dimension, and σ is interfacial energy. The lattice parameter mismatches of Al_3Sc and Al_3Yb with α–Al are 1.36 and 3.65 %, respectively [8,19]. According to the studies of Marquis *et al.* [1], the

elastic constant of α–Al is 28.5 GPa and the interfacial energy σ^{Al/Al_3Sc} approximates 0.2 J m^{-2}. The interfacial energy σ^{Al/Al_3Yb} was obtained by Van Dalen *et al.* [20] and the result showed the value of 0.6 ± 0.3 J m^{-2}.

For the Al_3Sc precipitate shown in Figure 3.7(c) (diameter is 18.1 nm), L approximates 0.4 suggesting that the interfacial energy is dominant to control the precipitate morphology. The precipitate morphology in this case showed a great rhombicuboctahedron shape predicted by Marquis *et al.* [1].

For the $Al_3(Sc,Yb)$ precipitate shown in Figure 3.7(d) (diameter is 18.5 nm) L value is 1.17 ± 0.585. In this case the precipitate morphology was governed by both the elastic strain energy and interfacial energy. Various studies proposed 2D and 3D equilibrium morphology of a misfit, coherent precipitate as a function of L [21-23]. The results showed that the equilibrium morphology of precipitate for a cuboid with smoothly curvature faces, rounded edges and corners. The degree of curvature varies with the value of L. Three-dimensional equilibrium morphology of precipitate at low value of L (L = 1–2) was exhibited in Figure 3.8. This predicted morphology is nearly spheroidal shape and fits with the morphology of $Al_3(Sc,Yb)$ precipitate shown in Figure 3.7(d).

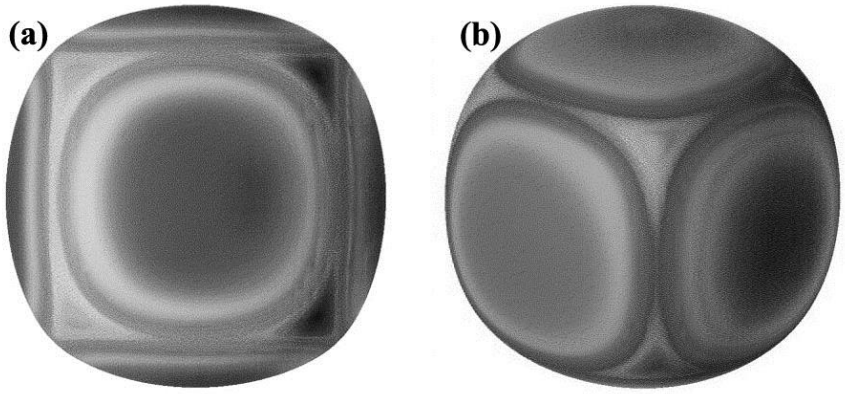

Figure 3.8. Three-dimensional equilibrium morphology for L = 1-2 viewed along: (a) [100] direction and (b) [111] direction [23].

3.1.2.2 Coarsening behaviour

The coarsening behaviour of spherical precipitates in binary alloys was predicted by The Lifshitz–Slyozov–Wagner (LSW) model base on volume diffusion theory [24,25]. The Ostwald ripening of spherical precipitates was developed in concentrated multicomponent alloys by Umantsev and Olsan [26] and more detailed in ternary alloys, allowing for capillary effects by Kuehmann and Voorhees (KV) [27].

According to the KV model, the coarsening behaviour of precipitates was analysed through the following equation:

$$\langle \mathrm{R(t)} \rangle^{n} - \langle \mathrm{R(t_0)} \rangle^{n} = K(t - t_0) \qquad (3.1)$$

where K is a coarsening rate constant, $\langle \mathrm{R(t)} \rangle$ is the average precipitate radius at time t, $\langle \mathrm{R(t_0)} \rangle$ is the average precipitate radius at the onset of quasi-stationary coarsening at time t_0, and n is the inverse time exponent. Eq. (1) could be applied for both binary alloy (Al–0.28Sc) and ternary alloy (Al–0.24Sc–0.07Yb) with different coarsening rate constant. It was assumed that $\langle \mathrm{R(t_0)} \rangle^{n}$ and t_0 is much smaller than $\langle \mathrm{R(t)} \rangle^{n}$ and t, the Eq. (1) became [28,29]:

$$\langle \mathrm{R(t)} \rangle^{n} = Kt \qquad (3.2)$$

A log–log plot of Eq. (2) reveals a slope of $\frac{1}{n}$ as following equation:

$$\log \langle \mathrm{R(t)} \rangle = \frac{1}{n}\log t + \frac{1}{n}\log K \qquad (3.3)$$

This slope is known as a time exponent of coarsening and often reported to indicate the coarsening behaviour of precipitates. By applying the KV model to the Al–0.28Sc and Al–0.24Sc–0.07Yb alloys aged at 325 °C, the time exponents of coarsening $\frac{1}{n}$ was calculated and showed the same value of 0.19 for both alloys. This value indicated that the precipitate coarsening behaviour of both investigated alloys is similar to the Al–0.18 at% Sc alloy aged at 300 °C ($\frac{1}{n}$ = 0.18) referred by Marquis *et al.* [1,28] and Al–0.06 at% Sc–0.02 at% Yb alloy aged at 300 °C ($\frac{1}{n}$ = 0.18) referred by Van Dalen *et al.* [30].

3.1.3 Precipitation hardening mechanisms

The evolution of precipitates and corresponding hardness at different aging conditions is presented in Table. 2. According to Hyland *et al.* [31] and Marquis *et al.* [2], the volume fraction of precipitate is approximately constant for Al–Sc alloys aged at various temperatures from 275 °C to 400 °C after long enough aging time (longer than 10000 s at 288 °C and 2000 s at 343 °C). On this work the alloys were aged at 300, 325, and 350 °C for 5h and 7 days. For these conditions and according to the findings of Hyland and Marquis we can assume that the volume fraction of precipitates is constant. The precipitation hardening is typically understood through the cutting mechanism which dislocations cut through precipitates and the Orowan bypass mechanism which dislocations bow or loop precipitates. According to the experimental data from the

study about precipitation strengthening in Al–0.3 wt% Sc alloy, Marquis *et al.* [2] predicted a transition from cutting mechanism to Orowan bypass mechanism at a precipitate diameter of 4.2 nm. The strength of alloy is controlled by the cutting mechanism for smaller sizes, and the Orowan bypass mechanism for larger sizes of precipitates which higher precipitate diameter results in lower hardness. Table 3.1 showed a maximum hardness around 73 (HV_{30}) at a precipitate diameter from 4.3 to 5.6 nm for both alloys. It sharply decreases to HV_{30} = 50 when the average diameter of precipitate increases to 13.7–15.4 nm. This result is in a good agreement with above theory and the result of Marquis *et al.* [2].

3.2 Conclusions

The similarity of microstructure, hardness and aging behaviour of Al–0.24Sc–0.07Yb alloy in comparison with Al–0.28Sc alloy was shown in this investigation. It indicates that the substitution of 0.07 wt% Yb for more expensive Sc in the Al–0.28Sc alloy is possible. Some final characteristics of Al–0.28Sc and Al–0.24Sc–0.07Yb alloys were concluded below:

- The hardness values of both alloys aged without homogenization treatment are significantly higher than those of alloys aged after homogenization treatment.
- The approximately spheroidal Al_3Sc and $Al_3(Sc,Yb)$ precipitates were uniformly distributed throughout the α–Al matrix. The precipitates remain fully coherent with α–Al matrix even after aging at high temperature for long time.
- With the aging temperature of 325 °C, the average diameter is 4.3 nm for Al_3Sc precipitates and 4.5 nm for $Al_3(Sc,Yb)$ precipitates at the aging peak. At the temperature of 350 °C and 7 days aging, the average diameter of Al_3Sc and $Al_3(Sc,Yb)$ precipitates are 13.7 and 15.4 nm, respectively.
- The Al_3Sc precipitates of Al–0.28Sc alloy show the facetted shape that are similar with great rhombicuboctahedron shape, while the $Al_3(Sc,Yb)$ precipitates of Al–0.24Sc–0.07Yb alloy show an approximately spheroidal shape.

References

[1] Marquis EA, Seidman DN. Nanoscale structural evolution of Al3Sc precipitates in Al(Sc) alloys. Acta Mater. 2001;49:1909-19.

[2] Marquis EA, Seidman DN, Dunand DC. Precipitation strengthening at ambient and elevated temperatures of heat-treatable Al(Sc) alloys. Acta Mater. 2003;51:285-7.

[3] Røyset J, Ryum N. Scandium in aluminium alloys. Int. Mater. Rev. 2005;50:19-44.

[4] Toropova LS, Eskin DG, Kharakterova ML, Dobatkina TV. Advanced aluminum alloys containing scandium: structure and properties Amsterdam, Gordon and Breech, The Netherlands, 1998.

[5] Iwamura S, Miura Y. Loss in coherency and coarsening behavior of Al3Sc precipitates. Acta Mater. 2004;52:591-600.

[6] Drits MY, Ber LB, Bykov YG, Toropova LS, Anastas'eva GK. Aging of alloy Al-0. 3 at. %Sc. Phys. Met. Metallogr. 1984;57:118-26.

[7] ICfD. Data, Using the Powder diffraction file: International Centre for Diffraction Data; 1996.

[8] Harada Y, Dunand DC. Microstructure of Al3Sc with ternary transition-metal additions. Mater. Sci. Eng. A. 2002;329–331:686-95.

[9] Harada Y, Dunand DC. Thermal expansion of Al3Sc and Al3(Sc0.75X0.25). Scri. Mater. 2003;48:219-22.

[10] Kramer LS, Tack WT, Fernandes MT. Scandium in aluminum alloys. Adv. Mater. Processes. 1997;152:23-4.

[11] Jones MJ, Humphreys FJ. Interaction of recrystallization and precipitation: The effect of Al3Sc on the recrystallization behaviour of deformed aluminium. Acta Mater. 2003;51:2149-59.

[12] Ocenasek V, Slamova M. Resistance to recrystallization due to Sc and Zr addition to Al-Mg alloys. Mater. Charact. 2001;47:157-62.

[13] Karnesky RA, van Dalen ME, Dunand DC, Seidman DN. Effects of substituting rare-earth elements for scandium in a precipitation-strengthened Al–0.08 at. %Sc alloy. Scri. Mater. 2006;55:437-40.

[14] Dalen ME, Dunand DC, Seidman DN. Nanoscale precipitation and mechanical properties of Al-0.06 at.% Sc alloys microalloyed with Yb or Gd. J Mater Sci. 2006;41:7814-23.

[15] Sawtell RR, Morris JW. Dispersion Strengthened Aluminum Alloys. TMS, Warrendale, PA. 1988.

[16] Sawtell RR. Exploratory alloy development in the system Al–Sc–X. Berkeley: University of California. 1988.

[17] Onaka S, Kobayashi N, Fujii T, Kato M. Simplified energy analysis on the equilibrium shape of coherent γ' precipitates in γ matrix with a superspherical shape approximation. Intermetallics. 2002;10:343-6.

[18] Thompson ME, Su CS, Voorhees PW. The equilibrium shape of a misfitting precipitate. Acta Metall. Mater. 1994;42:2107-22.

[19] Villars P, Okamoto H, Prince A. Handbook of ternary alloy phase diagrams. [Materials Park, OH]: ASM International; 1995.

[20] van Dalen ME, Karnesky RA, Cabotaje JR, Dunand DC, Seidman DN. Erbium and ytterbium solubilities and diffusivities in aluminum as determined by nanoscale characterization of precipitates. Acta Mater. 2009;57:4081-9.

[21] Mueller R, Gross D. 3D inhomogeneous, misfitting second phase particles-equilibrium shapes and morphological development. Comput. Mater. Sci. 1999;16:53-60.

[22] Li X, Thornton K, Nie Q, Voorhees PW, Lowengrub JS. Two- and three-dimensional equilibrium morphology of a misfitting particle and the Gibbs–Thomson effect. Acta Mater. 2004;52:5829-43.

[23] Thompson ME, Voorhees PW. Equilibrium particle morphologies in elastically stressed coherent solids. Acta Mater. 1999;47:983-96.

[24] Wagner CZ, Elektrochem Z. Angew Phys Chem. 1961;65:581.

[25] Lifshitz IM, Slyozov VV. The kinetics of precipitation from supersaturated solid solutions. J. Phys. Chem. Solids. 1961;19:35-50.

[26] Umantsev A, Olson GB. Ostwald ripening in multicomponent alloys. Scri. Metall. Mater. 1993;29:1135-40.

[27] Kuehmann CJ, Voorhees PW. Ostwald ripening in ternary alloys. Metall. Mater. Trans. A. 1996;27:937-43.

[28] Marquis EA, Seidman DN. Coarsening kinetics of nanoscale Al3Sc precipitates in an Al–Mg–Sc alloy. Acta Mater. 2005;53:4259-68.

[29] Lai J, Zhang Z, Chen XG. Precipitation strengthening of Al–B4C metal matrix composites alloyed with Sc and Zr. J. Alloys Compd. 2013;552:227-35.

[30] van Dalen ME, Dunand DC, Seidman DN. Microstructural evolution and creep properties of precipitation-strengthened Al–0.06Sc–0.02Gd and Al–0.06Sc–0.02Yb (at.%) alloys. Acta Mater. 2011;59:5224-37.

[31] Hyland RW. Homogeneous nucleation kinetics of Al3Sc in a dilute Al-Sc alloy. MTA. 1992;23:1947-55.

CHAPTER 4: PRECIPITATION AND AGE-HARDENING BEHAVIOUR OF Al–Mg–Sc AND Al–Mg–Sc–Yb ALLOYS

Chapter 4: Precipitation and age-hardening behaviour of Al–Mg–Sc and Al–Mg–Sc–Yb alloys

Introduction

In Sc–containing Al alloys, the Al–Mg–Sc alloys have attracted more attention due to their wide range application in automotive, aerospace, ship building and structural fields. The combination between of solid-solution hardening and precipitation hardening leads Al–Mg–Sc alloys have excellent properties of both Al–Mg and Al–Sc alloys. According to Sawtell and Jensen [1], the properties of Al–Mg–Sc alloys appear to reflect a superposition of the characteristics of Al–Sc alloys and Al–Mg alloys. Formation of the $A1_3Sc$ precipitate appears to be unaltered by the presence of Mg. Magnesium increases the strength and strain-hardening exponent of the Al–Sc base alloy in direct proportion to the amount of Mg present in solution. The increased strain hardening significantly improves crack initiation toughness resulting in a better overall combination of strength and toughness for alloys containing Mg. The addition of Mg also reduces the subgrain size during fabrication through their influence on deformation mode and thus improves superplastic performance as measured by maximum superplastic elongation or strain rate/temperature to achieve a given elongation. Lathabai and Lloyd [2] studied the microstructure, mechanical properties and weld hot cracking behaviour of a cast Al–Mg–Sc alloy containing 0.17 wt% Sc in comparison with those of a Sc-free alloy of similar chemical composition. The results showed that the Al–Mg–Sc alloy had significantly higher 0.2% proof stress (~55% higher) and tensile strength (~20% higher) as well microhardness (~30% higher) and a slightly lower ductility than the cast Al–Mg alloy. The higher levels of Sc should improve the weld hot cracking resistance of alloys by enhanced grain refinement of both the casting and the weld metal. The previous researches have proven that Yb can substitute a part of Sc in binary Al–Sc alloy in order to reduce their cost without decreasing of alloy properties [3-5]. There was not any study showing the effect of Yb on properties of Al–Mg–Sc alloy.

In this chapter, in this study the precipitation and age-hardening behaviour of Al–4Mg–0.3Sc and Al–4Mg–0.24Sc–0.06Yb alloys were investigated. The aging behaviour, precipitate morphologies, precipitate coarsening and precipitation hardening of both alloys were discussed. The average diameter and the size distribution of nanoscale Al_3Sc and $Al_3(Sc,Yb)$ precipitates at various aging conditions were measured. Transmission electron microscopy (TEM) and high-resolution TEM were used to understand the precipitate behaviour.

4.1 Results and discussion

4.1.1 Age hardening behaviour of the as-cast alloys

4.1.1.1 Isochronal aging behaviour

The Vickers hardness of Al–4Mg–0.3Sc and Al–4Mg–0.24Sc–0.06Yb alloys aged at various temperatures from 200–450 °C for 2 h were shown in Figure 4.1. The onset of age hardening for both alloys occurs at 250 ◦C. The Vickers hardness increases rapidly when aging at 300 °C and obtains the hardness peaks of 110 HV for Al–4Mg–0.3Sc alloy and 103 HV for Al–4Mg–0.24Sc–0.06Yb alloy at 325 ◦C. The Vickers hardness was decreased sharply at 400 ◦C and 450 ◦C due to the precipitate coarsening. The partial replacement of Sc by Yb did not significantly affect either the kinetics or the peak hardness. In order to compare with Al–4Mg–0.3Sc and Al–4Mg–0.24Sc–0.06Yb alloys, the Vickers hardness curves of Al–0.28Sc and Al–0.24Sc–0.07Yb alloys aged at various temperatures from 150–375 ◦C for 2 h also presented in Figure 4.1. It can be seen that solid solution strengthening by adding Mg has significantly increased the hardness of Al–Sc–(Yb) alloys.

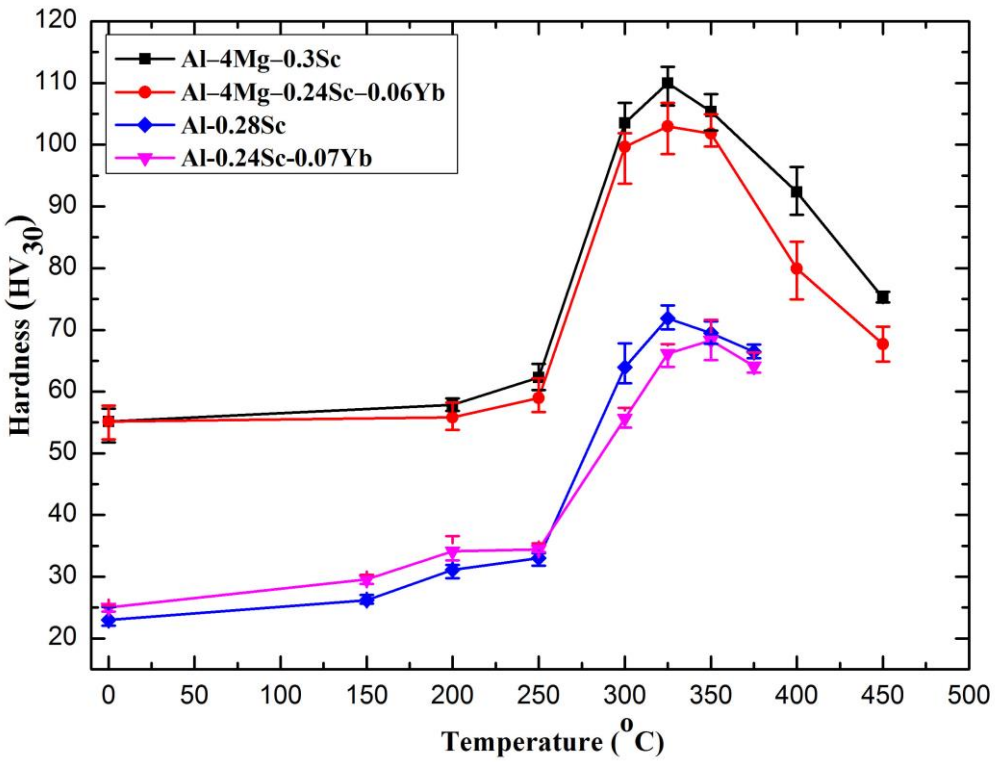

Figure 4.1. Isoschronal aging curves of Al–4Mg–0.3Sc and Al–4Mg–0.24Sc–0.06Yb alloys in comparison with Al–0.28Sc and Al–0.24Sc–0.07Yb alloys.

4.1.1.2 Isothermal aging behaviour

The age hardening behaviour of Al–0.28Sc, Al–0.24Sc–0.07Yb, Al–4Mg–0.3Sc, and Al–4Mg–0.24Sc–0.06Yb alloys at aging temperatures of 300, 325 and 350 °C were shown in Figure 4.2.

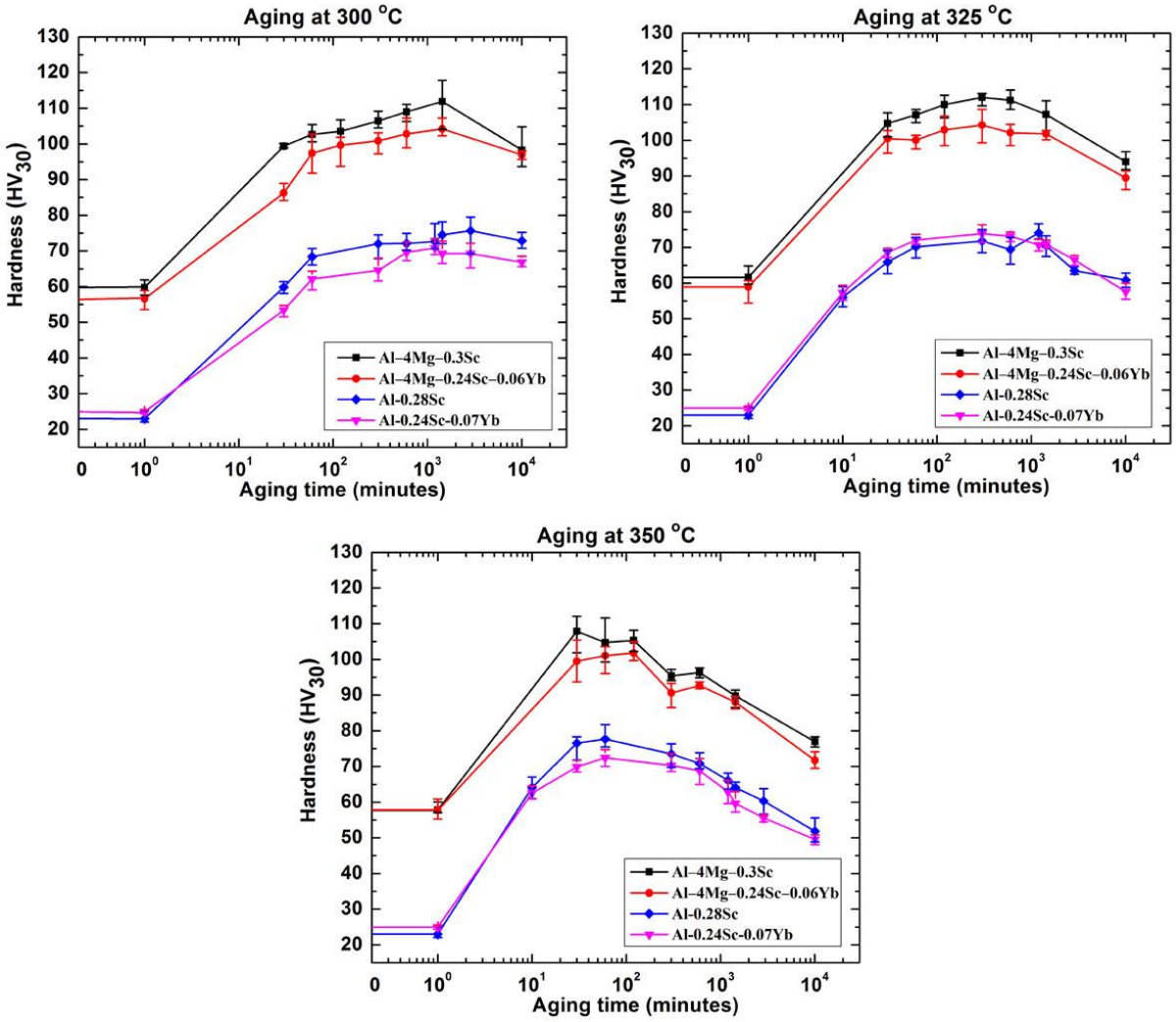

Figure 4.2. Isothermal ageing curves of Al–4Mg–0.3Sc and Al–4Mg–0.24Sc–0.06Yb alloys in comparison with Al–0.28Sc and Al–0.24Sc–0.07Yb alloys aged at 300 ◦C, 325 ◦C, and 350 ◦C.

The curves show that Al–4Mg–0.24Sc–0.06Yb alloy has a similar aging behaviour with Al–4Mg–0.3Sc alloy with four distinguished regions: an incubation period, a period with a rapid increase in hardness values, a period of maximum hardness values (peak aging), and over-aging. The aging rate increases with the increasing of aging temperature. Higher temperature leads to earlier occurrence of over-aging. Higher aging temperature conducts to higher diffusion rate for precipitates nucleation and growth that consequently accelerates the over-aging stage. The Al–4Mg–0.3Sc and Al–4Mg–0.24Sc–0.06Yb alloys reach the hardness value peak after 1 day, 5 h, and 30 minutes when aging at 300, 325, and 350 °C, respectively. At aging temperature of 300 °C, the Vickers hardness of Al–4Mg–0.3Sc and Al–4Mg–0.24Sc–0.06Yb alloys reach peak values of 112 ± 6 and 104 ± 3 HV, and slightly decreases to 98 ± 6 and 97 ± 1 HV after 7 days aging respectively. At aging temperature of 325 °C, the Vickers hardness of Al–4Mg–0.3Sc and Al–4Mg–0.24Sc–0.06Yb alloys reach the peak values of 112 ± 2 and

104 ± 5 HV, and decreases to 94 ± 2 and 89 ± 3 HV after 7 days aging, respectively. At aging temperature of 350 °C, the Vickers hardness of Al–4Mg–0.3Sc and Al–4Mg–0.24Sc–0.06Yb alloys reach the peak values of 108 ± 5 and 102 ± 4 HV, and substantial decreases to 77 ± 1 and 72 ± 2 HV after 7 days aging respectively. It can be seen that both alloys show a slow over-aging at 300 and 325 °C and much faster at 350 °C.

In comparison with Al–0.28Sc and Al–0.24Sc–0.07Yb alloys, the evolutions of hardness of Al–4Mg–0.3Sc, and Al–4Mg–0.24Sc–0.06Yb alloys with time are similar and the values are significantly higher that of Al–0.28Sc and Al–0.24Sc–0.07Yb alloys at every aging conditions. Addition of Mg increases the hardness of Al–Sc–(Yb) alloys but did not change the aging kinetic of those alloys.

4.1.2 Precipitate behaviour

4.1.2.1 Precipitate morphologies and distributions

The TEM micrographs of Al–4Mg–0.3Sc and Al–4Mg–0.24Sc–0.06Yb alloys aged at 325 °C for 5 h, 325 °C for 7 days, and 350 °C for 7 days are shown in Figure 4.3, respectively. The micrographs show the spheroidal Al_3Sc and $Al_3(Sc,Yb)$ precipitates, uniformly distributed throughout the α–Al matrix.

The precipitate diameter of both alloys at different aging conditions was measured and the corresponding results are presented in Table 4.1. At hardness peak when aging at 325 °C, the average diameter of Al_3Sc and $Al_3(Sc,Yb)$ precipitates in both alloys are 3.5 ± 0.6 nm. After 7 days aging at 325 °C, the average diameter of Al_3Sc in Al–4Mg–0.3Sc alloy slowly increases to 6.3 ± 1.4 nm that lead to slightly decreasing of hardness. The $Al_3(Sc,Yb)$ precipitate in Al–4Mg–0.24Sc–0.06Yb alloy shows a faster coarsening rate than Al_3Sc in Al–4Mg–0.3Sc alloy when aging at 325 °C. The average diameter of $Al_3(Sc,Yb)$ in Al–4Mg–0.24Sc–0.06Yb alloy is 9.5 ± 1.4 nm. At the temperature of 350 °C and 7 days aging, the average diameter of Al_3Sc and $Al_3(Sc,Yb)$ precipitates are 13.0 ± 1.6 and 12.6 ± 1.9 nm, respectively. This result is in accordance with the conclusion in the Section 3.2.3 for precipitation hardening in Al–0.28Sc and Al–0.24Sc–0.07Yb alloys. The maximum hardness was achieved at a precipitate diameter around 4–6 nm. The hardness sharply decreases when the average diameter of precipitate above 12 nm. In comparison with Al–0.28Sc and Al–0.24Sc–0.07Yb alloys (Section 3.1.2.1), at the same aging condition the average sizes of precipitates in Al–4Mg–0.3Sc and Al–4Mg–0.24Sc–0.06Yb alloys were slightly lower.

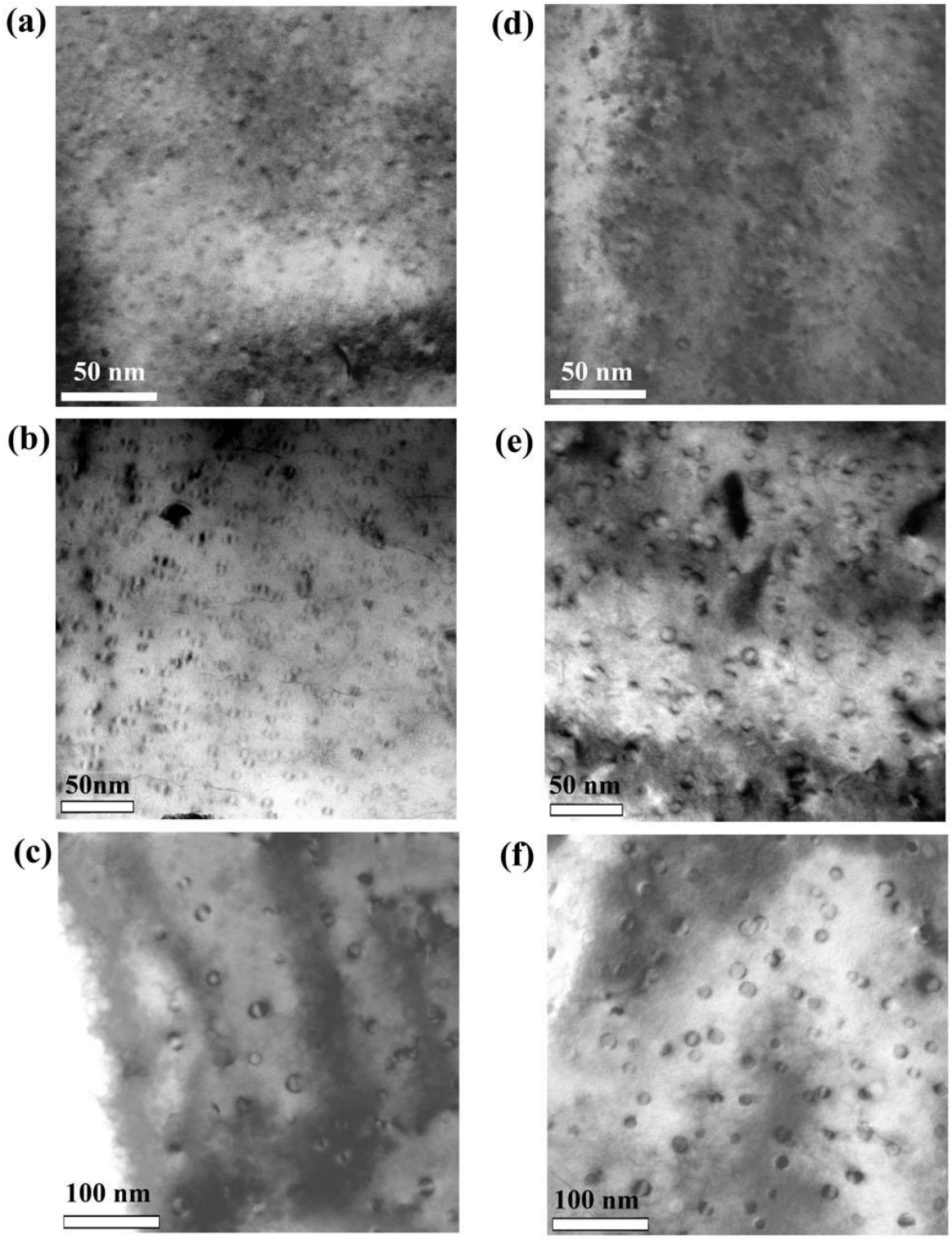

Figure 4.3. TEM micrographs of Al–4Mg–0.3Sc (a–b–c) and Al–4Mg–0.24Sc–0.06Yb (d–e–f) alloys aged at 325 ◦C for 5 h, 325 ◦C for 7 days, and 350 ◦C for 7 days.

Table 4.1. Average precipitate diameter and hardness of Al–4Mg–0.3Sc and Al–4Mg–0.24Sc–0.06Yb alloys

Aging condition	Al–4Mg–0.3Sc		Al–4Mg–0.24Sc–0.06Yb	
	Precipitate diameter (nm)	Hardness (HV_{30})	Precipitate diameter (nm)	Hardness (HV_{30})
325 °C, 5h	3.5 ± 0.6	112 ± 2	3.5 ± 0.6	104 ± 5
325 °C, 7 days	6.3 ± 1.4	94 ± 2	9.5 ± 1.4	89 ± 3
350 °C, 7 days	13.0 ± 1.6	77 ± 1	12.6 ± 1.9	72 ± 2

The precipitates size distribution (PSDs) of Al–4Mg–0.3Sc and Al–4Mg–0.24Sc–0.06Yb alloys aged at 325 °C for 5 h, 325 °C for 7 days, and 350 °C for 7 days are shown in Figure 4.4, respectively.

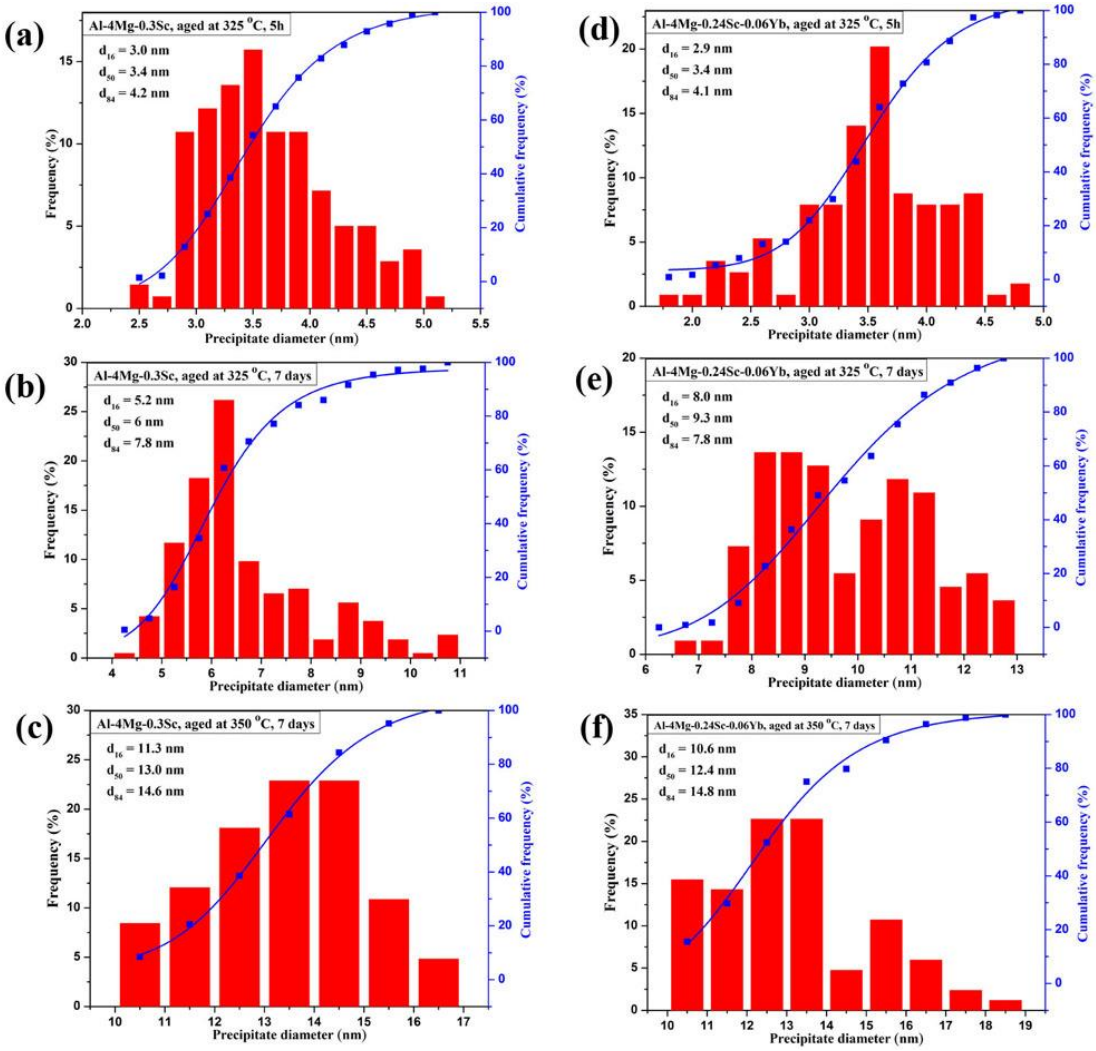

Figure 4.4. Precipitates size distribution of Al–4Mg–0.3Sc (a–b–c) and Al–4Mg–0.24Sc–0.06Yb (d–e–f) alloys aged at 325 °C for 5 h, 325 °C for 7 days, and 350 °C for 7 days: d_{16}, d_{50}, and d_{84} are the precipitate diameters corresponding to 16, 50, and 84 % cumulative undersize particle size distribution.

The results show that the Al_3Sc precipitates in Al–4Mg–0.3Sc alloy are more uniformly distributed than $Al_3(Sc,Yb)$ precipitates in Al–4Mg–0.24Sc–0.06Yb alloy at the same aging condition. The precipitates diameter ranges in Al–4Mg–0.3Sc alloy aged at 325 ◦C for 5 h, 325 ◦C for 7 days, and 350 ◦C for 7 days are 2.5–5.5, 4–11, and 10–17 nm, respectively. The precipitates diameter ranges in Al–4Mg–0.24Sc–0.06Yb alloy aged at 325 ◦C for 5 h, 325 ◦C for 7 days, and 350 ◦C for 7 days are 1.5–5.5, 6.5–13, and 10–19 nm, respectively.

4.1.2.2 High resolution TEM study

Precipitates in Al–4Mg–0.3Sc and Al–4Mg–0.24Sc–0.06Yb alloys aged at 325 ◦C for 5 h, 325 ◦C for 7 days, and 350 ◦C for 7 days were studied by high resolution TEM technique.

According to selected area (electron) diffraction (SAD) analysis, the [011] and [112] (Figure 4.5) zone axis orientation was found to fit well to the simulation of the reciprocal lattice section at the orientation. Al_3Sc and $Al_3(Sc,Yb)$ precipitates with cubic lattice $L1_2$ (cP4) structure in HRTEM images can be identified by using Digital Micrograph software. The reflections from (100) and $(0\bar{1}1)$ of $L1_2$ Al_3Sc and $Al_3(Sc,Yb)$ precipitates were determined by using a fast Fourier transform (FFT) analysis. The inverse fast Fourier transform (IFFT) obtained by applying masks near reflections from (100) and $(0\bar{1}1)$ could show much better contrast for precipitates identification.

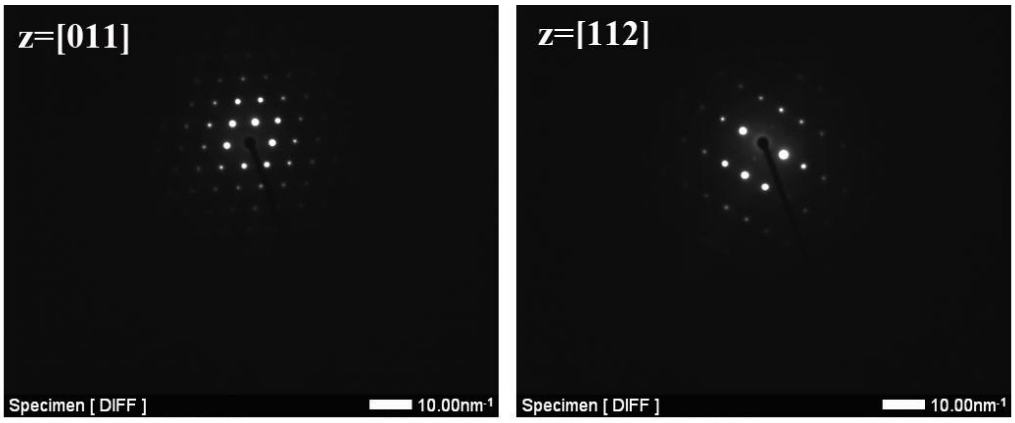

Figure 4.5. SAD taken along the [100] or [110] crystallographic directions.

High-resolution TEM images, FFT and IFFT of precipitates in Al–4Mg–0.3Sc and Al–4Mg–0.24Sc–0.06Yb alloys aged at 325 ◦C for 5 h are shown in Figure 4.6. A clear lattice cross-grating contrast of precipitates is not clearly defined in HRTEM images. Very fine, fully coherent precipitates (3–4 nm) distributed throughout the α–Al matrix were detected by using IFFT analysis. There are no misfits between the precipitates and the matrix appearing in the structure.

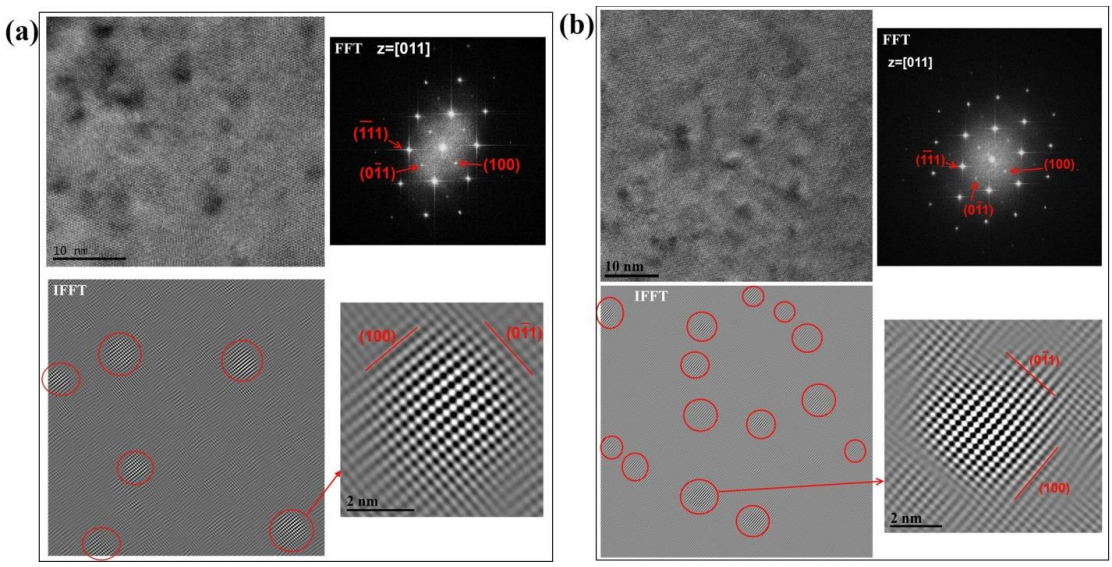

Figure 4.6. High-resolution TEM images, FFT and IFFT of precipitates in Al–4Mg–0.3Sc (a) and Al–4Mg–0.24Sc–0.06Yb (b) alloys aged at 325 °C for 5 h.

High-resolution TEM images, FFT and IFFT of precipitates in Al–4Mg–0.3Sc and Al–4Mg–0.24Sc–0.06Yb alloys aged at 325 °C for 7 days and 350 °C for 7 days are shown in Figure 4.7.

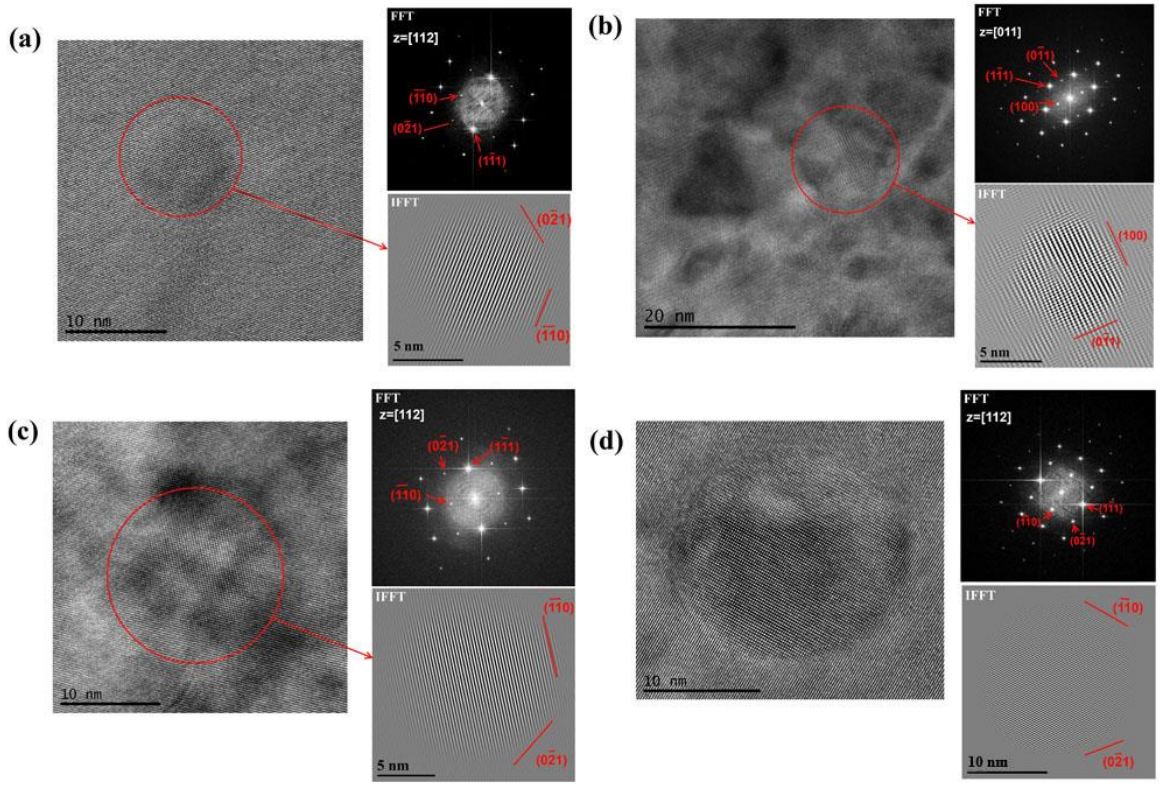

Figure 4.7. High-resolution TEM images, FFT and IFFT of precipitates in Al–4Mg–0.3Sc (a–c) and Al–4Mg–0.24Sc–0.06Yb (b–d) alloys aged at 325 °C for 7 days (a–b) and 350 °C for 7 days (c–d).

The precipitate sizes of Al–4Mg–0.3Sc and Al–4Mg–0.24Sc–0.06Yb alloys were measured and show the values of 10 and 9 nm when aging at 325 °C for 7 days and 14 and 18 nm when aging at 350 °C for 7 days, respectively. All precipitates remain fully coherent with the α–Al matrix. The morphology of Al_3Sc and $Al_3(Sc,Yb)$ precipitates in Al–4Mg–0.3Sc and Al–4Mg–0.24Sc–0.06Yb alloys aged at 350 °C for 7 days is clearly spheroidal shape.

4.2 Conclusions

The precipitation and age-hardening behaviour of Al–4Mg–0.3Sc and Al–4Mg–0.24Sc–0.06Yb alloys were investigated. Some final conclusions were summarized below:

- The spheroidal Al_3Sc and $Al_3(Sc,Yb)$ precipitates were uniformly distributed throughout the α–Al matrix. The precipitates remain fully coherent with α–Al matrix even after aging at high temperature for long time.
- The maximum hardness was achieved at a precipitate diameter around 4–6 nm. The hardness sharply decreases when the average diameter of precipitate above 12 nm.
- The hardness of Al–4Mg–0.3Sc and Al–4Mg–0.24Sc–0.06Yb alloys were significantly higher than that of Al–0.28Sc and Al–0.24Sc–0.07Yb alloys at the same aging condition due to the solid solution strengthening of Al–Mg. The average size of precipitates in Al–4Mg–0.3Sc and Al–4Mg–0.24Sc–0.06Yb alloys was slightly lower than that of Al–0.28Sc and Al–0.24Sc–0.07Yb alloys at the same aging conditions.

References

[1] Sawtell R, Jensen C. Mechanical properties and microstructures of Al-Mg-Sc alloys. Metall. Mater. Trans. A. 1990;21:421-30.

[2] Lathabai S, Lloyd PG. The effect of scandium on the microstructure, mechanical properties and weldability of a cast Al–Mg alloy. Acta Mater. 2002;50:4275-92.

[3] Karnesky RA, van Dalen ME, Dunand DC, Seidman DN. Effects of substituting rare-earth elements for scandium in a precipitation-strengthened Al–0.08 at. %Sc alloy. Scri. Mater. 2006;55:437-40.

[4] Dalen ME, Dunand DC, Seidman DN. Nanoscale precipitation and mechanical properties of Al-0.06 at.% Sc alloys microalloyed with Yb or Gd. J. Mater. Sci. 2006;41:7814-23.

[5] Tuan NQ, Pinto AMP, Puga H, Rocha LA, Barbosa J. Effects of substituting ytterbium for scandium on the microstructure and age-hardening behaviour of Al–Sc alloy. Mater. Sci. Eng. A. 2014;601:70-7.

CHAPTER 5 – GRAIN REFINEMENT OF Al-Mg-Sc ALLOYS

The work presented in this chapter was based on the paper accepted for publication: **N.Q. Tuan**, H. Puga, J. Barbosa, A.M.P. Pinto, "Grain refinement of Al-Mg-Sc alloy by ultrasonic treatment", Metals and Materials International (will be published in Vol.21 & No.1. (Jan, 2015))

Chapter 5 - Grain refinement of Al–Mg–Sc alloys

Introduction

In foundry practice of aluminium alloys, several processes have been applied to achieve a fine, equiaxed and uniform grain microstructure. Grain refinement plays an important role to enhance mechanical properties as toughness, fracture resistance, fatigue strength and isotropic behaviour of the cast alloys. Two methods are usually used for microstructure refinement: chemical and physical techniques with particular emphasis to first. There are three major mechanisms for grain refinement during solidification process those are heterogeneous nucleation, restricting the grain growth and breaking the solidified crystals.

The chemical method is widely applied in industry by grain refiner inoculation [1-4]. Through adding grain refiners as Al–Ti or Al–Ti–B master alloys, the particles of $TiAl_3$, TiB_2 phases in the molten alloy will act as nuclei, promoting heterogeneous nucleation, nucleating solid particles during solidification [3]. However, only 1% of the refiner particles are active for nucleation of solid grain [1,3]. The rest of them contaminate the casting alloy and have detrimental effects on the final microstructure and mechanical properties.

Another approach to achieve grain refinement is some kind of physical method that may promote nucleation, obtaining grain multiplication by dendrite fragmentation under mechanical force or external physical field without further chemical addition [5]. Dramatic grain refinement has been obtained in Al–10 wt% Mg and AA7449 alloys by applying intensive melt shearing above liquidus temperature [6,7]. Other techniques have been successfully applied for grain refinement, such as mechanical stirring, electromagnetic stirring [8], and gas bubbling [9,10]. However those techniques are time consuming, can promote low fluidity and are high costly.

During the last years an effort has been done to develop reliable ultrasonic techniques to control the microstructure of several engineering alloys, with particular emphasis to Al and Mg based ones, to overtake the problems associated to traditional refinement techniques. Khalifa *et al.* [11] and Jian *et al.* [12] demonstrated that it is possible to obtain non dendritic and globular grains of primary α–Al phase smaller than 100 μm by supplying acoustic energy to molten AlSi7Mg, isothermally and during solidification, respectively. Ultrasonic vibration can also be used to refine hypereutectic Al–Si alloys, as demonstrated by Feng *et al.* [13], who obtained equiaxed, α–Al crystals of around 40 μm and homogeneously distributed primary Si phase with average size of 180 μm in AlSi23 alloy.

Puga *et al.* [14,15] studied the influence of ultrasonic power and treatment temperature on the microstructure and mechanical properties of a AlSi9Cu3 alloy by applying ultrasound to the melt during the first stages of solidification. The results showed that ultrasound promoted the formation of refined globular structures and globular α–Al grain sizes decreased with increasing of treatment temperature and electric power. Moreover, uniform distribution of fine particles of the β–Al5FeSi intermetallic phase was also obtained. Ultrasonic treated alloys showed better mechanical properties in comparison with non-ultrasonic treated alloys.

It is important to notice that until now the capability of ultrasound as microstructure refinement technique of metallic alloys has been evaluated for a very narrow range of alloys. Most of the studies have been directed to magnesium alloys [16-20] and aluminium-silicon alloys [11-15,21-23]. Besides, in foundry practice cast alloys must not be poured at low temperature because consequent low fluidity often leads to premature solidification, cold shuts and incomplete castings. On the other hand, high pouring temperatures usually promote grain coarsening, oxide formation and gas porosity. Ultrasonic treatment is a potential process to obtain grain refinement within a wide temperature range, decreasing or even eliminating the traditional defects associated to high or low refining and pouring temperatures.

Al–Mg–Sc alloys have received a lot of attention due to their excellent mechanical behaviour [24-26]. However, there are no available studies concerning grain refinement of these alloys. Almost studies of Al–Mg–Sc alloys concentrated on strengthening mechanism with Al_3Sc precipitates and effect of Mg on it. Grain refinement and its mechanism of Al–Mg–Sc alloys, especially with hypoeutectic composition of Sc (the content of Sc is lower than 0.55 wt%) have not been studied. In this chapter, the role of Mg and Sc as well as the influence of pouring temperature on grain refinement of Al–1Mg–0.3Sc (wt%) was presented. In another work, the effect of ultrasonic treatment on grain refinement of Al–1Mg–0.3Sc alloy at a wide range of pouring temperatures was evaluated. The microstructures of Al–1Mg–0.3Sc alloy at various pouring temperatures with ultrasonic treatment were evaluated. The mechanism of grain refinement was proposed and understood.

5.1 Results and discussion

5.1.1 Grain refinement of Al–Mg–Sc alloys without ultrasonic treatment

5.1.1.1 Grain refinement results

i) Effect of Mg and Sc on grain refinement of Al–Mg–Sc alloys

Figure 5.1 shows the optical micrographs of Al–1Mg, Al–0.3Sc, Al–4Mg, Al–1Mg–0.3Sc, and Al–4Mg–0.3Sc alloys cast at 700 ± 5 °C. It is clear that the microstructure of

Al–4Mg, Al–1Mg–0.3Sc and Al–4Mg–0.3Sc alloys have a uniform, equiaxed and finer grain size in comparison with Al–1Mg and Al–0.3Sc alloys.

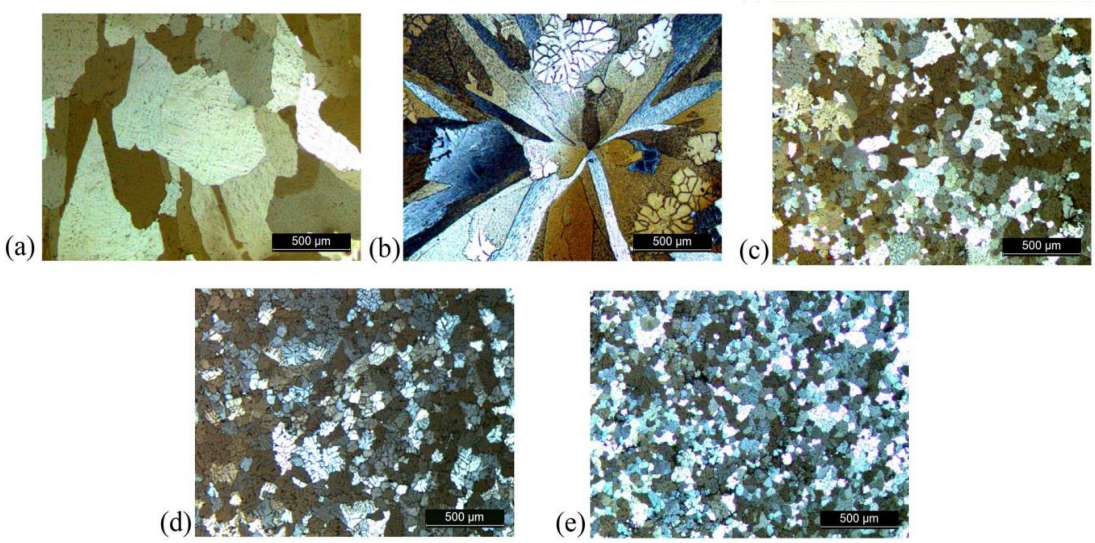

Figure 5.1. Optical micrographs of as-cast alloys cast at 700 °C : (a) Al–1Mg, (b) Al–0.3Sc, (c) Al–4Mg, (d) Al–1Mg–0.3Sc, (e) Al–4Mg–0.3Sc.

Figure 5.2 presents the average grain sizes of those as-cast alloys. The average grain size of the Al–1Mg alloy is 439 ± 21 μm and it decreases to 95 ± 2μm in the Al–4Mg alloy. The average grain size of the Al–0.3Sc alloy is 410 ± 15 μm and it decreases to 103 ± 2 and 56 ± 1 μm in Al–1Mg–0.3Sc and Al–4Mg–0.3Sc alloys, respectively. Besides, it can also be inferred that the grain size of Al–1Mg can be significantly reduced by adding a small content of Sc (0.3 wt% in this case). In fact, according to Figures 5.1(a) and 1(d), the average grain size of Al–1Mg alloy decreases from 439 ± 21 μm to 103 ± 2 μm in Al–1Mg–0.3Sc alloy.

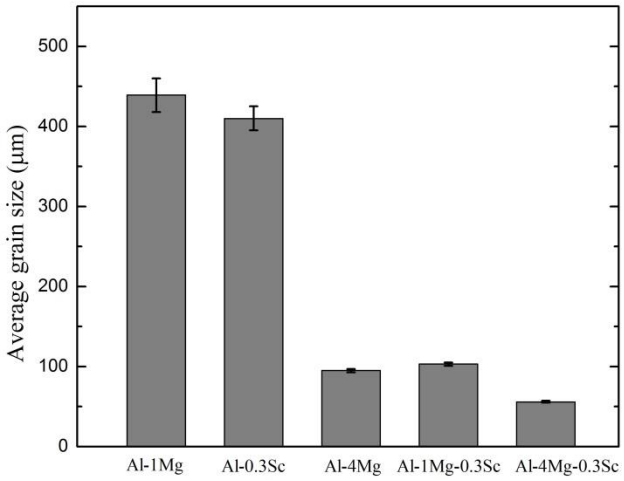

Figure 5.2. Average grain size and hardness of Al–1Mg, Al–0.3Sc, Al–4Mg, Al–1Mg–0.3Sc, Al–4Mg–0.3Sc as-cast alloys cast at 700 °C.

ii) Effect of pouring temperature on grain refinement of Al–1Mg–0.3Sc alloy

Figure 5.3 shows the optical micrographs of as-cast Al–1Mg–0.3Sc alloys without ultrasonic treatment poured at 800 and 770 °C ± 5 °C. The microstructure exhibits columnar zones (present in the centre of the samples) with elongated grains and dendritic features and the outer chill zones (present in the border of samples) with finer and more equiaxed grains. The average grain size of Al–1Mg–0.3Sc samples poured at 800 and 770 °C ± 5 °C is 487 ± 20 and 394 ± 14 µm. The different morphology of coarse grains in the different zones can be explained by the different solidification rate and interfacial temperature gradient [27]. In the chill zone, under the large supercooling that occurs as soon as the molten alloy contacts the cold mould wall a large number of nuclei forms and grow as equiaxed shaped grains. After pouring, the temperature gradient at the mould walls decreases and the grains in the chill zone grow dendritically side by side in the direction of the heat flow which is perpendicular to the mould walls. They stop growing when they meet grains growing out from the opposite wall. This process leads to the formation of elongated grains and creates the columnar zone.

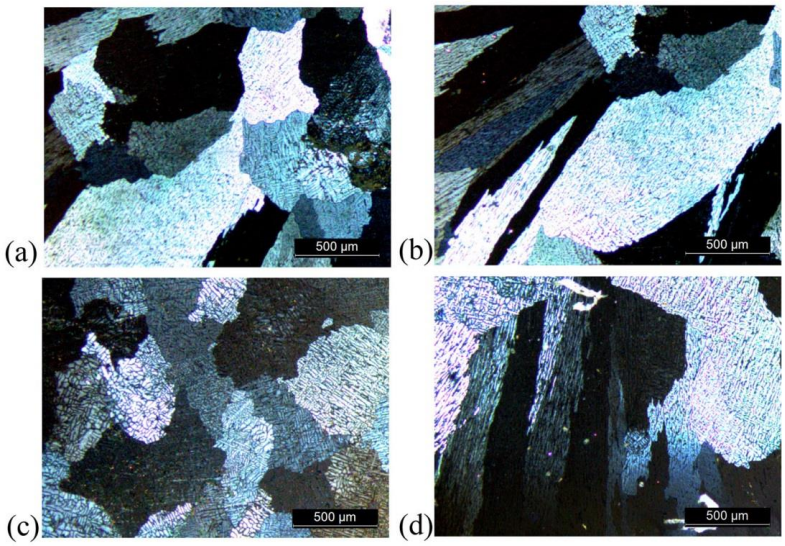

Figure 5.3. Optical micrographs of Al–1Mg–0.3Sc alloy cast at pouring temperatures: (a–b) 800 °C, (c–d) 770 °C: (a), (c) in the border of samples; (b), (d) in the centre of samples.

Figure 5.4 shows the optical micrographs of as-cast Al–1Mg–0.3Sc alloys without ultrasonic treatment poured at 740, 720 and 700 °C ± 5 °C. It is evident that grain size gradually decreases with decreasing of pouring temperature. The average grain size of Al–1Mg–0.3Sc samples poured at 740, 720, and 700 °C are at 269 ± 8, 197 ± 5 and 103 ± 2 µm, respectively. It is evident to conclude that the pouring temperature has a strong influence on the grain size of the Al–1Mg–0.3Sc alloy.

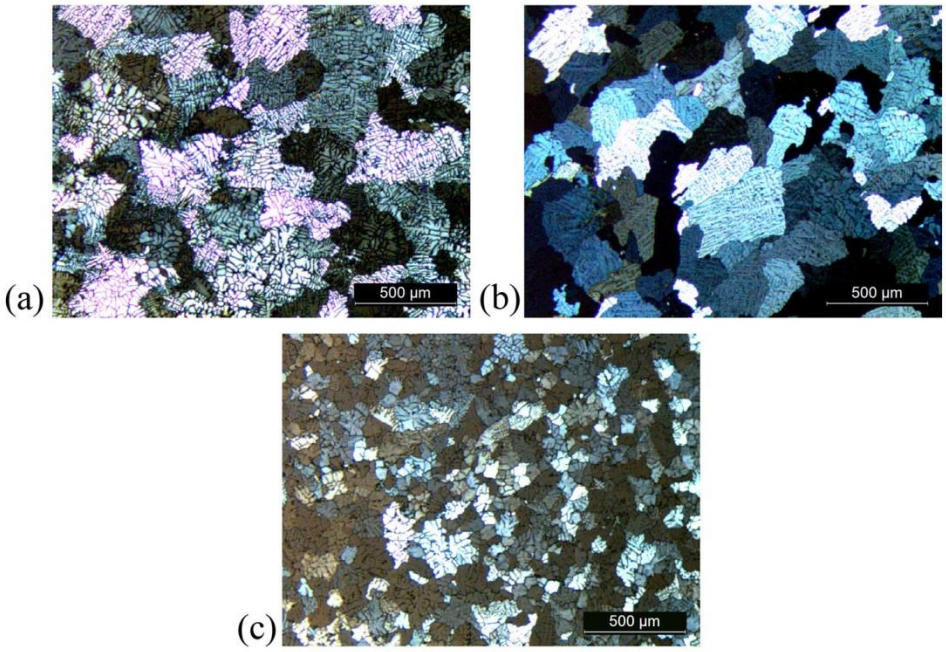

Figure 5.4. Optical micrographs of Al–1Mg–0.3Sc alloy cast at pouring temperatures: (a) 740 ◦C, (b) 720 ◦C, (c) 700 ◦C.

The grain size distribution of Al–1Mg–0.3Sc alloy poured at 800, 770, 740, 720 and 700 ± 5 ◦C is illustrated in Figure 5.5. The grain size of those samples is within the range of 200–1000, 200–800, 100–500, 50–400, and 50–270 μm, respectively. It is evident that the most fine and uniform equiaxed grains were achieved on the sample cast at 700 ◦C.

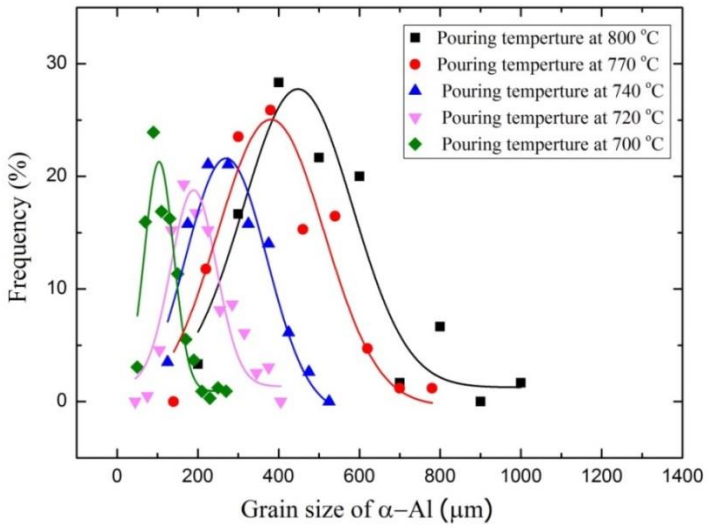

Figure 5.5. Grain size distribution of Al–1Mg–0.3Sc cast samples for different pouring temperatures.

5.1.1.2 Grain refinement mechanism

i) Nucleation mechanism

According to research reviews of Murty *et al.* [28] it is easily perceptible that grain refinement is very far from fully understood and is still object of discord between researchers. According to Li *et al.* [29] $MgAl_2O_4$ particles that form in Al–Mg melt can act as potential sites for heterogeneous nucleation of α–Al grains. $MgAl_2O_4$ oxide has a perfect lattice matching with α–Al at the {1 1 1} plane that promotes high potency for heterogeneous nucleation. In this experiment, when the melt was heated up to 800 °C, $MgAl_2O_4$ oxide formed due to the high affinity of Mg with oxygen. The oxidation process was followed by two consecutive steps: $Mg + 1/2O_2 \rightarrow MgO$, and then $MgO + 2Al + 3/2O_2 \rightarrow MgAl_2O_4$. $MgAl_2O_4$ is present as oxide films in Al–Mg alloy with low Mg content and as dispersed discrete particles in alloys with high content of Mg [29]. This is the reason why Al–1Mg and Al–4Mg present so different microstructures (Figures 5.1(a) and 5.1(c)) even having been processed on the same conditions. The higher density of $MgAl_2O_4$ particles in the melt due to the higher content of Mg in Al–4Mg alloy promotes more nuclei sites for α–Al nucleation, leading to a more refined and homogeneous microstructure with smaller grain size.

The much lower average grain size of Al–1Mg–0.3Sc in comparison with Al–1Mg and Al–0.3Sc alloys suggested that grain refinement was achieved in aluminium alloys containing both Sc and Mg. The theory proposed by Johnsson *et al.* [30] described the influence of nucleants and segregating solutes on grain refinement. Solute elements like Sc, Mg, Si, Cu and Fe segregate to the nucleant/melt interface and restrict the growth of dendrites, so there is more time for nucleation to occur [28,30]. Moreover, segregating elements would lead to constitutional undercooling in front of the interface. This constitutionally undercooled zone activates the nucleant agent in front of the interface. In case of Al–1Mg–0.3Sc alloy, the nucleant particles could be $MgAl_2O_4$ oxide or impurity particles. Segregating Sc can lead to form Al_3Sc that has $L1_2$ structure, a small lattice parameter mismatch and fully coherent with α–Al at elevated temperatures [31]. This characteristic makes Al_3Sc an ideal nucleating agent for grain refinement of Al alloys. In addition, Alexander Pisch *et al.* [32] indicated that the eutectic composition of Sc decreases with increasing Mg content in the Al–Mg–Sc alloy. This characteristic facilitates the formation of Al_3Sc. The increasing of nucleant potency and segregating potency due to the existence of both Sc and Mg improves grain refinement in Al–1Mg–0.3Sc alloy. The finest grain size observed in the microstructure of Al–4Mg–0.3Sc alloy could be understood through combination of those mechanisms.

Figure 5.6 shows the SEM micrographs and EDS spectra of Al–0.3Sc alloy cast at 700 ◦C. Intermetallic particles containing Al, Sc, Si, and Fe in this alloy exhibit a rod-like shape, which cannot act as nuclei sites for α–Al nucleation.

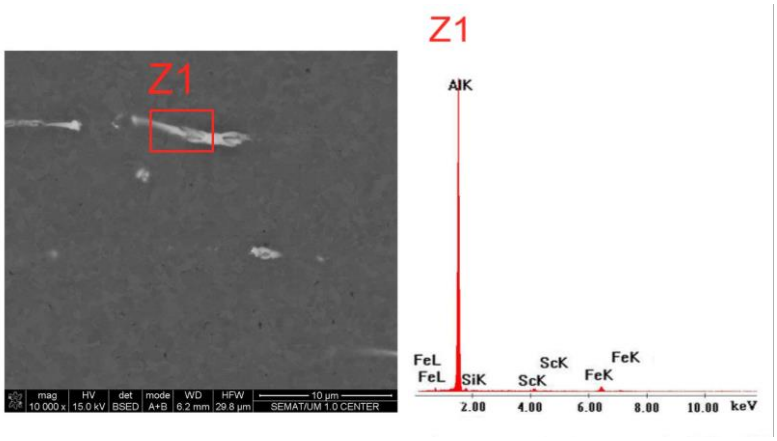

Figure 5.6. SEM micrograph and EDS spectra of intermetallic phase in Al–0.3Sc alloy cast at 700 ◦C.

Figure 5.7 presents the SEM micrograph and EDS spectra of Al–1Mg –0.3Sc alloy cast at 700 ◦C. Oxide nucleus (Z2), intermetallic nucleus containing Al, Mg, Sc, Si, Fe, and Cu (Z1) and intermetallic nucleus containing Al, Mg, Sc, Si, and Fe (Z3) were detected in the microstructure of this alloy.

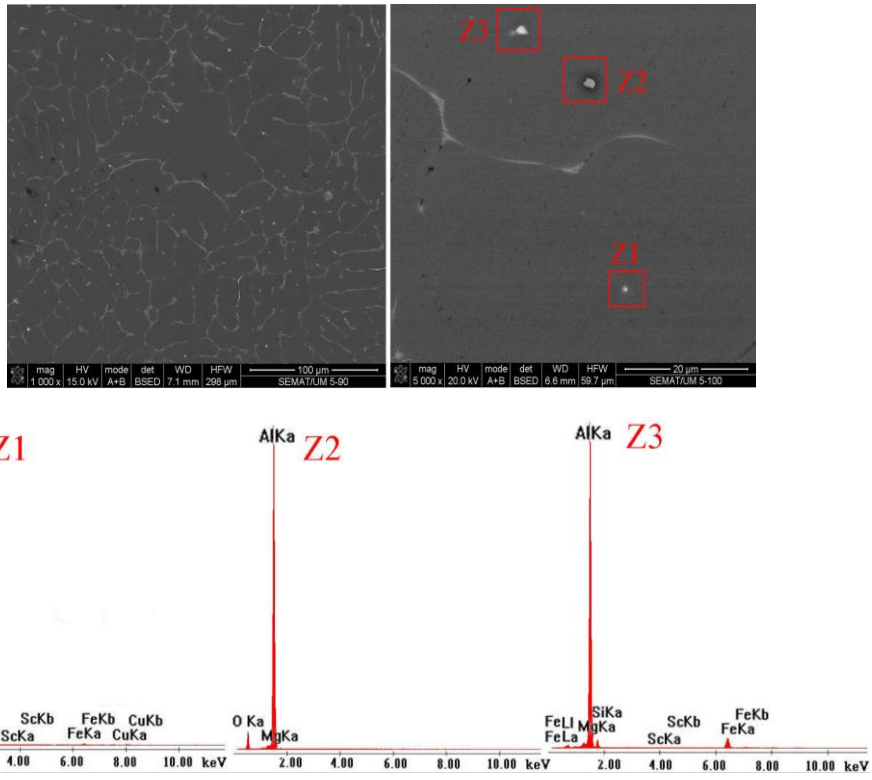

Figure 5.7. SEM micrograph and EDS spectra of intermetallic phases in Al–1Mg–0.3Sc alloy cast at 700 ◦C.

Figure 5.8 shows the SEM micrograph and EDS spectra of Al–4Mg–0.3Sc alloy cast at 700 ◦C. Oxide nucleus (Z1 particle) was detected in this micrograph.

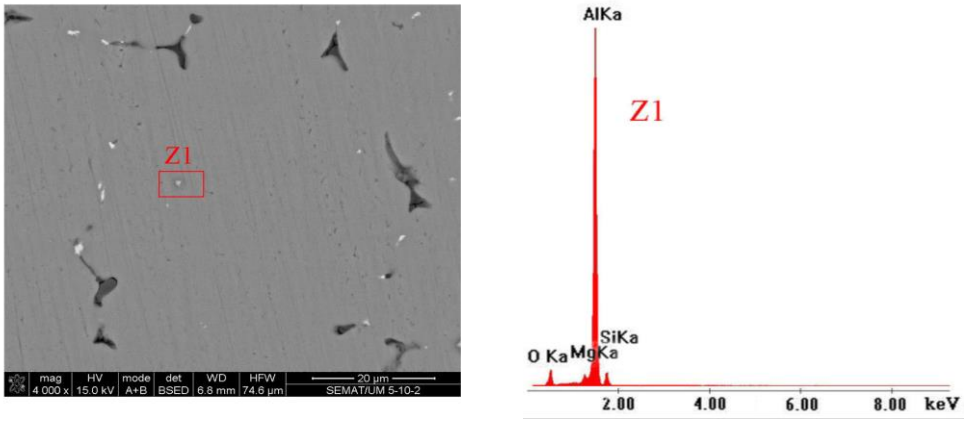

Figure 5.8. SEM micrograph and EDS spectrum of oxide nucleus in Al–4Mg–0.3Sc alloy cast at 700 °C.

ii) Effect of pouring temperature on grain refinement in Al–1Mg–0.3Sc alloy

When the alloy is melted and poured at high temperature, the melt is quite homogeneous and consequently reduces the segregating potency of solute elements. The constitutional undercooling in front of the nucleant/melt interface will not happen and Al_3Sc cannot form. The low segregating potency and nucleant potency result in very coarse grains in the microstructure of as-cast alloy. At lower pouring temperature, the segregating potency and nucleant potency are higher that leads to better refining effect promoting the development of finer and more homogeneous equiaxed grains in the microstructure of as-cast alloy. Figure 5.9 shows the SEM micrograph and EDS spectra of Al–1Mg –0.3Sc alloy cast at 770 °C. Almost second phase particles are intermetallic phase of Al, Mg, and Fe with a rod-like morphology. Those particles cannot act as heterogeneous nuclei sites to form α–Al grain.

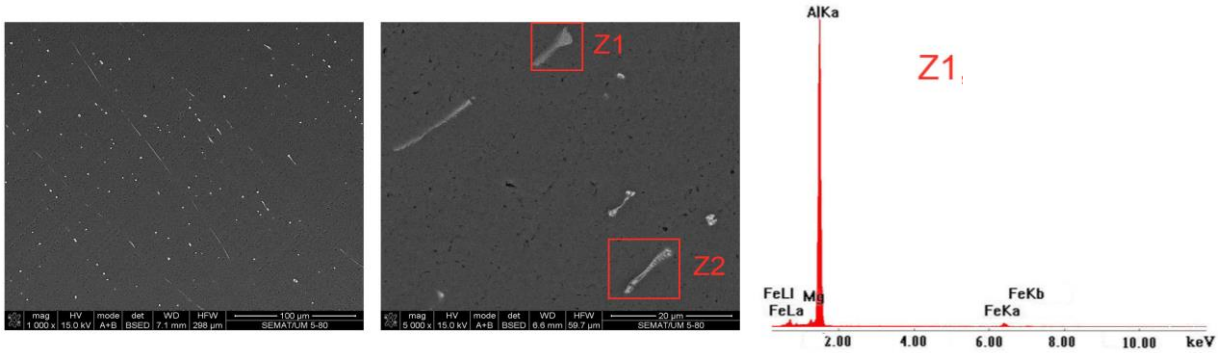

Figure 5.9. SEM micrograph and EDS spectra of intermetallic phase (Z1) in Al–1Mg–0.3Sc alloy cast at 770 °C.

The mechanism of grain refinement that bases on heterogeneous nucleation above liquidus and dendrite growth restriction was proposed. In general, $MgAl_2O_4$ oxide and Al_3Sc are the main possibilities of nuclei site for α–Al nucleation. Figure 5.10 sketches the mechanisms of α–Al nucleation that probably happen during solidification of those alloys.

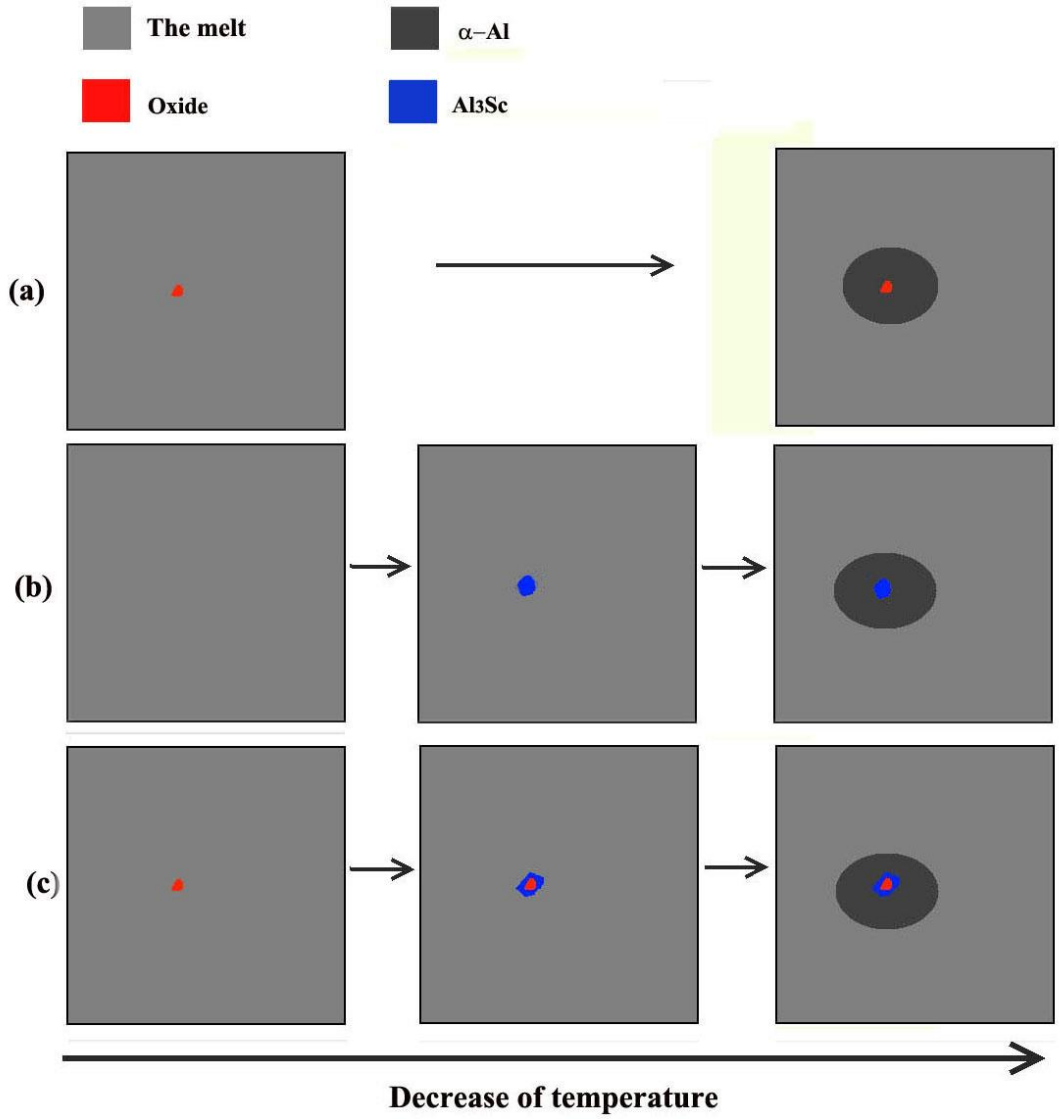

Figure 5.10. Schematic of α–Al nucleation on (a) oxides, (b) Al_3Sc, and (c) Al_3Sc nucleated on oxide particles.

5.1.2 Grain refinement of Al–Mg–Sc alloys with ultrasonic treatment

5.1.2.1 Effect of ultrasonic treatment at various temperatures on grain size of Al–1Mg–0.3Sc alloy

Figure 5.11 and 5.12 show the optical micrographs and the grain size distribution of Al–1Mg–0.3Sc cast samples with ultrasonic treatment at the temperatures of 800, 770, 740, 720, and 700 ± 5 °C.

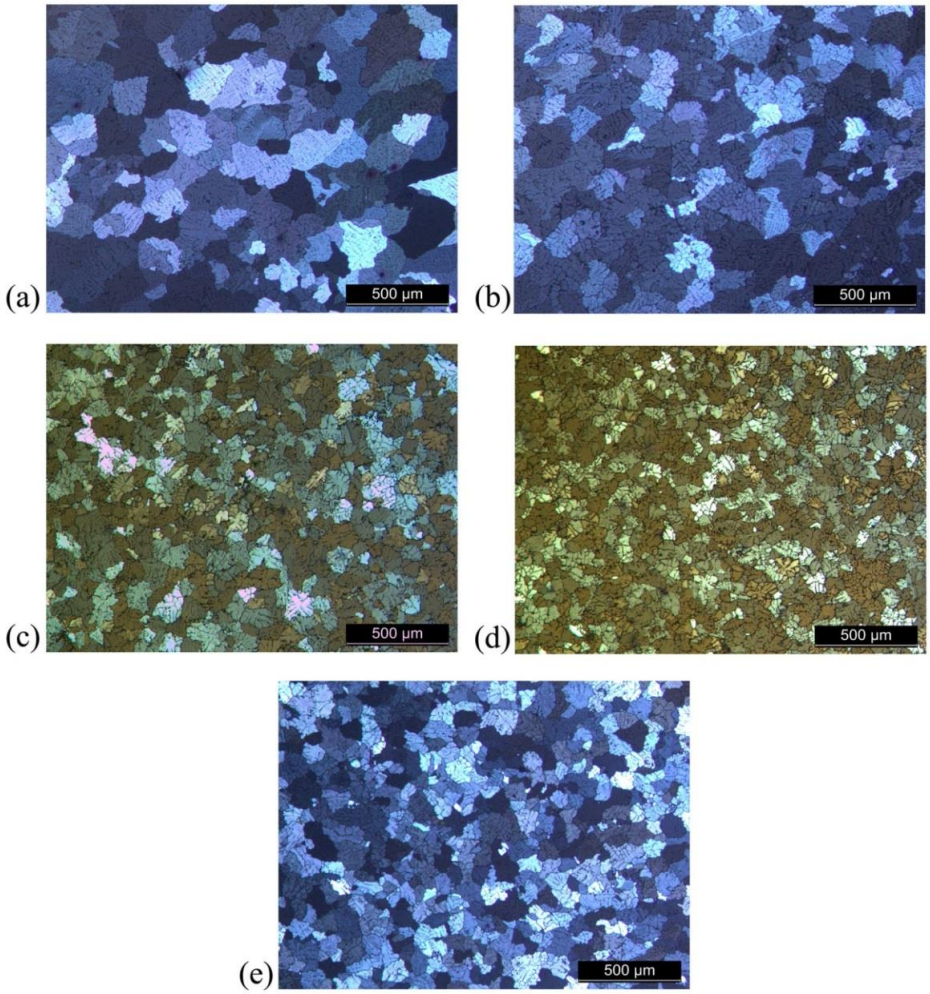

Figure 5.11. Optical micrographs of Al–1Mg–0.3Sc alloy ultrasonic treated at different temperatures: (a) 800 ◦C, (b) 770 ◦C, (c) 740 ◦C, (d) 720 ◦C, (e) 700 ◦C.

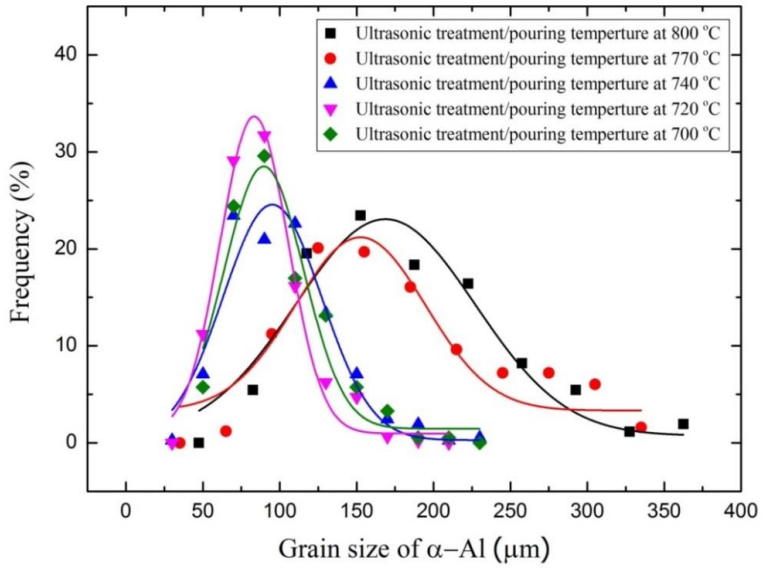

Figure 5.12. Grain size distribution of Al–1Mg–0.3Sc samples ultrasonic treated at different temperatures.

It is obvious that the impact of ultrasonic treatment on grain refinement depends on the treatment temperature. The influence of ultrasonic treatment on grain refinement is most effective within the temperature range of 700–740 °C. The average grain size of cast samples is 98 ± 2, 83 ± 1, 93 ± 2 μm for 740, 720, and 700 °C ultrasonic treatment temperatures, respectively. When the alloy was treated by ultrasonic vibration at 770 and 800 °C, the grains tend to be larger, with average size of 166 ± 4 and 169 ± 4 μm, respectively. At the temperature of 720 °C, the grains are finer and more uniform than at any other treatment temperature.

The quantitative results of the average grain size of Al–1Mg–0.3Sc alloys are summarized and presented in Figure 5.13 to compare the grain size of alloys with and without ultrasonic treatment. The strong refinement effect of ultrasound is quite clear, especially if the treatment is conducted within the temperature range 700–740 °C.

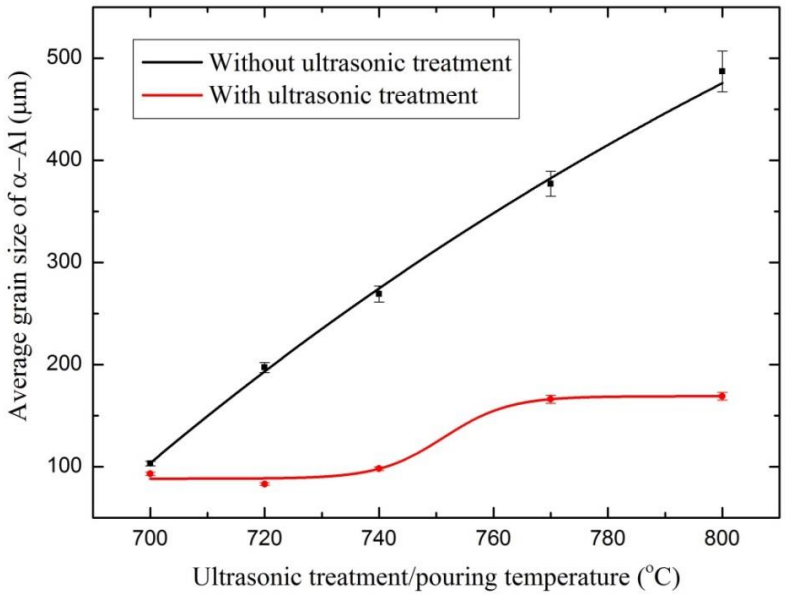

Figure 5.13. Effect of ultrasonic treatment on the average grain size of Al–1Mg–0.3Sc alloys.

Figure 5.14 shows the grain size distribution of the most refined samples with and without ultrasonic treatment. It is evident that ultrasonic vibration not only decreases the average grain size but also homogenizes grain size distribution, as can be inferred by the higher frequency of grains with less than 100 μm. These results suggest that ultrasonic treatment can be applied to foundry practice of the Al–1Mg–0.3Sc alloy at a wide range of temperatures ensuring both fluidity of the melt and grain refinement.

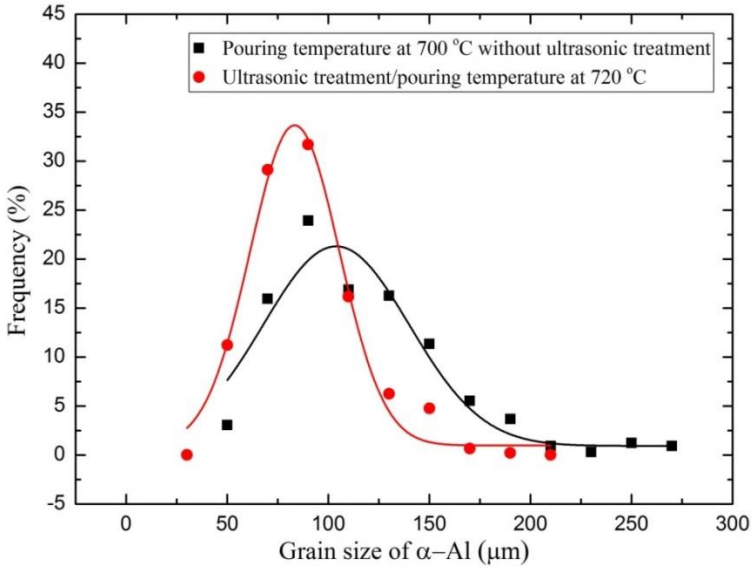

Figure 5.14. Effect of ultrasonic treatment temperature on grain size distribution of Al–1Mg–0.3Sc cast alloy.

5.1.2.2 Grain refinement mechanism

We propose that cavitation-enhanced heterogeneous nucleation is the main mechanism of grain refinement by ultrasonic treatment in Al–1Mg–0.3Sc alloy. When the ultrasonic treatment was applied directly into the melt, a large number of cavitation bubbles were formed throughout the melt. These cavitation bubbles grow and the bubbles temperature decreases due to the expansion of the gas inside them. At critical size of bubbles, they will collapse and generate the pressure pulse. The increase of the local pressure in the melt leads to transiently increase of the melting point of the alloy according to the Clausius-Clapeyron equation. The decrease of bubble temperature and the increase of melting point lead to high localized undercooling at the bubble/melt interface. As a consequence, a large number of nuclei are formed at the surface of existing bubbles. These bubbles will collapse and disperse nuclei into the melt. Through acoustic streaming, the nuclei are homogeneously distributed throughout the melt. Moreover, the cavitation phenomenon cleans the surfaces of nuclei, improves their wettability and consequently increases the nucleant potency.

High ultrasonic treatment temperatures will shorten the life time of cavitation bubbles and decrease undercooling in the melt. Therefore, the number of nuclei formed in the melt will decrease which results in less grain refinement. This mechanism explains the increase in average grain size when the ultrasonic treatment temperature increases from 720 to 800 ◦C. The slightly higher grain size of the alloy treated at 700 ◦C in comparison with 720 ◦C can be explained by a decrease in melt fluidity. The lower fluidity of the melt reduces the dispersion of nuclei that results in less grain refinement.

5.2 Conclusions

5.2.1 Grain refinement of Al–Mg–Sc alloys without ultrasonic treatment

- The average grain size of Al–Mg alloy remarkably decreases from 439 ± 21 to 95 ± 2 μm when the content of Mg increases from 1 to 4 wt% at the pouring temperature of 700 °C.
- The average grain size of Al–1Mg sharply decreases from 439 ± 21 μm to 103 ± 2 μm by adding 0.3 wt% of Sc.
- The pouring temperature has a strong effect on the microstructure of Al–1Mg–0.3Sc alloy. Lower pouring temperature leads to smaller grain size and more homogeneous microstructure in this alloy. The fine equiaxed grains in microstructure can be achieved at pouring temperature range from 680–710 °C.
- The mechanism of grain refinement that bases on heterogeneous nucleation above liquidus and dendrite growth restriction by segregating solute elements was proposed. $MgAl_2O4$ oxide and Al_3Sc possibly act as nuclei sites for α–Al nucleation.

5.2.2 Grain refinement of Al–Mg–Sc alloys with ultrasonic treatment

- Ultrasonic vibration proved to be a potential grain refinement technique of Al–1Mg–0.3Sc. Significant grain refinement was obtained by applying ultrasonic treatment within the temperature range from 700 to 740 °C. This fact makes more flexible to decide the pouring temperature in the foundry practice of this kind of alloy. The best grain refinement and uniform grain size are obtained by ultrasonic treatment at 720 °C.
- Grain refinement of Al–1Mg–0.3Sc alloy by ultrasonic treatment can be explained by the cavitation-enhanced heterogeneous nucleation mechanism.

References

[1] Cantor B, O'Reily K (ed). Solidification and casting. IOP Publishing Ltd; 2003.

[2] Greer AL, Cooper PS, Meredith MW, Schneider W, Schumacher P, Spittle JA, et al. Grain Refinement of Aluminium Alloys by Inoculation. Adv. Eng. Mater. 2003;5:81-91.

[3] Greer AL, Bunn AM, Tronche A, Evans PV, Bristow DJ. Modelling of inoculation of metallic melts: application to grain refinement of aluminium by Al–Ti–B. Acta Mater. 2000;48:2823-35.

[4] Mohanty PS, Gruzleski JE. Mechanism of grain refinement in aluminium. Acta Metall. et Mater. 1995;43:2001-12.

[5] Das A, Liu G, Fan Z. Investigation on the microstructural refinement of an Mg–6 wt% Zn alloy. Mater. Sci. Eng. A. 2006;419:349-56.

[6] Haghayeghi R, Zoqui EJ, Eskin DG, Bahai H. Grain refinement of an Al–10% Mg alloy by intensive shearing in the liquid state. J. Alloys Compd. 2009;485:807-11.

[7] Haghayeghi R, Nastac L. On microstructural refinement of an AA7449 aluminium alloy through shearing above liquidus temperature. Mater. Lett. 2011;65:3230-3.

[8] Nafisi S, Emadi D, Shehata MT, Ghomashchi R. Effects of electromagnetic stirring and superheat on the microstructural characteristics of Al–Si–Fe alloy. Mater. Sci. Eng. A. 2006;432:71-83.

[9] Wannasin J, Canyook R, Wisutmethangoon S, Flemings MC. Grain refinement behavior of an aluminum alloy by inoculation and dynamic nucleation. Acta Mater. 2013;61:3897-903.

[10] Wannasin J, Martinez RA, Flemings MC. Grain refinement of an aluminum alloy by introducing gas bubbles during solidification. Scri. Mater. 2006;55:115-8.

[11] Khalifa W, Tsunekawa Y, Okumiya M. Effect of ultrasonic melt treatment on microstructure of A356 aluminium cast alloys. Int. J.Cast Met. Res. 2008;21:129-34.

[12] Jian X, Xu H, Meek TT, Han Q. Effect of power ultrasound on solidification of aluminum A356 alloy. Mater. Lett. 2005;59:190-3.

[13] Feng HK, Yu SR, Li YL, Gong LY. Effect of ultrasonic treatment on microstructures of hypereutectic Al–Si alloy. J.Mater. Process. Technol. 2008;208:330-5.

[14] Puga H, Barbosa J, Costa S, Ribeiro S, Pinto AMP, Prokic M. Influence of indirect ultrasonic vibration on the microstructure and mechanical behavior of Al–Si–Cu alloy. Mater. Sci. Eng. A. 2013;560:589-95.

[15] Puga H, Costa S, Barbosa J, Ribeiro S, Prokic M. Influence of ultrasonic melt treatment on microstructure and mechanical properties of AlSi9Cu3 alloy. J. Mater. Process. Technol. 2011;211:1729-35.

[16] Liu X, Osawa Y, Takamori S, Mukai T. Microstructure and mechanical properties of AZ91 alloy produced with ultrasonic vibration. Mater. Sci. Eng. A. 2008;487:120-3.

[17] Gao D, Li Z, Han Q, Zhai Q. Effect of ultrasonic power on microstructure and mechanical properties of AZ91 alloy. Mater. Sci. Eng. A. 2009;502:2-5.

[18] Qian M, Ramirez A, Das A, StJohn DH. The effect of solute on ultrasonic grain refinement of magnesium alloys. J. Cryst. Growth. 2010;312:2267-72.

[19] Ramirez A, Qian M, Davis B, Wilks T, StJohn DH. Potency of high-intensity ultrasonic treatment for grain refinement of magnesium alloys. Scri. Mater. 2008;59:19-22.

[20] Khosro Aghayani M, Niroumand B. Effects of ultrasonic treatment on microstructure and tensile strength of AZ91 magnesium alloy. J. Alloys Compd. 2011;509:114-22.

[21] Jian X, Meek TT, Han Q. Refinement of eutectic silicon phase of aluminum A356 alloy using high-intensity ultrasonic vibration. Scri. Mater. 2006;54:893-6.

[22] Zhang S, Zhao Y, Cheng X, Chen G, Dai Q. High-energy ultrasonic field effects on the microstructure and mechanical behaviors of A356 alloy. J. Alloys Compd. 2009;470:168-72.

[23] Yu SR, Feng HK, Li YL, Gong LY. Study on the properties of Al–23%Si alloy treated by ultrasonic wave. J. Alloys Compd. 2009;484:360-4.

[24] Marquis EA, Seidman DN. Coarsening kinetics of nanoscale Al3Sc precipitates in an Al–Mg–Sc alloy. Acta Mater. 2005;53:4259-68.

[25] Lathabai S, Lloyd PG. The effect of scandium on the microstructure, mechanical properties and weldability of a cast Al–Mg alloy. Acta Mater. 2002;50:4275-92.

[26] Sawtell R, Jensen C. Mechanical properties and microstructures of Al-Mg-Sc alloys. MTA. 1990;21:421-30.

[27] Abbaschian R, Abbaschian L, Reed-Hill RE. Physical Metallurgy Principles: Cengage Learning; 2008.

[28] Murty BS, Kori SA, Chakraborty M. Grain refinement of aluminium and its alloys by heterogeneous nucleation and alloying. Int. Mater. Rev. 2002;47:3-29.

[29] Li HT, Wang Y, Fan Z. Mechanisms of enhanced heterogeneous nucleation during solidification in binary Al–Mg alloys. Acta Mater. 2012;60:1528-37.

[30] Johnsson M, Backerud L, Sigworth G. Study of the mechanism of grain refinement of aluminum after additions of Ti- and B-containing master alloys. Metall and Mat Trans A. 1993;24:481-91.

[31] Harada Y, Dunand DC. Microstructure of Al3Sc with ternary transition-metal additions. Mater. Sci. Eng. A. 2002;329–331:686-95.

[32] Pisch A, Gröbner J, Schmid-Fetzer R. Application of computational thermochemistry to Al and Mg alloy processing with Sc additions. Mater. Sci. Eng. A. 2000;289:123-9.

CHAPTER 6: THE EFFECT OF SUBSTITUTING Yb FOR Sc ON CORROSION BEHAVIOUR OF HEAT TREATED Al–Sc AND Al–Mg–Sc ALLOYS

Chapter 6: The effect of substituting ytterbium for scandium and aged-hardening heat treatment on corrosion behaviour of Al–Sc and Al–Mg–Sc alloys

Introduction

Sc–containing Al alloys are potentially to apply in saltwater environment due to a good corrosion resistance. However, almost works have been focused on microstructure and mechanical properties while limited research is focused on corrosion behaviour of Sc–containing Al alloys. The effect of Sc on corrosion behaviour has been investigated in various Al alloys [1-15], pure Al [1], Al–Zn alloys [12,14], Al–Mg alloys [2-4], Al–Zn–Mg alloys [5-7,15], and Al–Cu–Li–Mg–Ag alloys [15]. These researches indicated that Sc has a positive effect on the corrosion properties of Al alloys. The results of corrosion rates and passivation current density indicated that the addition of Sc enhances the corrosion resistance of Al alloys [1,2,5]. The electrochemical properties of coarse Al_3Sc particle were investigated by Cavanaugh *et al.* [8] where the influence of these particles on the initiation and propagation of pitting corrosion in Al–2.05 wt% Sc alloy exposed to dilute chloride solution was evaluated. The authors reported that Al_3Sc is slightly cathodic to the α–Al matrix and spontaneously passivates with a low self-dissolution rate in dilute chloride solution. Al_3Sc showed slower oxygen reduction reaction kinetics than other dispersoid intermetallic phases as Al_3Zr, Al_6Mn and Al_3Ti. Ganiev [1] and Vyazovikina [15] proposed that the passive film in Sc–containing Al alloys consists of duplex layer of scandium oxide and aluminium oxide. Sc_2O_3 layer was formed by the presence of oxygen in the solution, deposited and accumulated on the surface of alloys. In comparison with the less defective Al_2O_3 layer, the duplex layer in Sc–containing Al alloys has more protective property. As a consequence, the corrosion resistance in these alloys was improved.

Another results for $Al_3Sc_xZr_{1-x}$ phases in Al–Zn–Mg–Cu alloys was shown by Wloka *et al.* [7]. The authors indicated that these coarse particles disturb the grain structure near the particle/matrix interface and initiate localized corrosion. Moreover, mass loss measurements showed that the addition of scandium increases the mass loss during the initial period. Ahmad and Aleem [16] studied the effect of Sc on mechanical properties and corrosion resistance of Al–2.5 Mg alloys doped with Sc and Zr. The authors reported that the homogeneous coherent nano $Al(Sc_{1-x}Zr_x)$ precipitates increase the passivation tendency and improve the corrosion resistance of alloys. It was also suggested that the formation of protective Sc_2O_3 reinforced Al_2O_3 films that enhanced the passivity of Al–Mg–Sc alloys. The film is very coherent with the matrix due to the coherency of the nano-precipitates without any discontinuities at the oxide/electrolyte interface. However, experimental proofs are needed to confirm this hypothesis.

To the best of our knowledge there was no research showing details of corrosion behaviour and its mechanisms of Sc–containing Al alloys.

In the present work, the corrosion behaviour of Al–0.28Sc and Al–0.24Sc–0.07Yb, Al–4Mg, Al–4Mg–0.3Sc and Al–4Mg–0.24Sc–0.06Yb alloys in 3.5 wt% of sodium chloride was investigated by immersion and potentiodynamic polarisation studies. The effect of the addition of Sc and Yb, impurity intermetallic phases, and heat treatment on corrosion behaviour of these alloys was studied.

6.1 Results and discussion

6.1.1 Effects of substituting ytterbium for scandium on corrosion behaviour of Al–Sc alloy

6.1.1.1 Impurity intermetallic particles

The morphologies of intermetallic particles in Al–0.28Sc and Al–0.24Sc–0.07Yb alloys were observed and the representative SEM images are given in Fig. 6.1. Chemical compositions of selected intermetallic particles were determined by EDS and the results are listed in Table 6.1. It can be seen that the intermetallic particles with rod-like and rounded shapes are uniformly distributed throughout the matrix in both Al–0.28Sc and Al–0.24Sc–0.07Yb alloys. The size range of rod-like particles is 7–15 μm in length whereas the size range of rounded particles is 1–3 μm. Two intermetallic phases were detected in Al–0.28Sc alloy: Al–Sc–Si–Fe (particles marked as “A1” and “A2”) and Al–Fe (particle marked as “A3”) containing intermetallic phases. Al–Sc–Yb–Si–Fe–Cu (particles marked as “B1”, “B2”, and “B3”), Al–Sc–Yb–Fe–Cu (particle marked as “B4”) containing intermetallic phases were observed in Al–0.24Sc–0.07Yb alloy. The age-hardening heat treatment did not affect significantly these intermetallic particles, thus they were also detected in heat treated samples of both alloys.

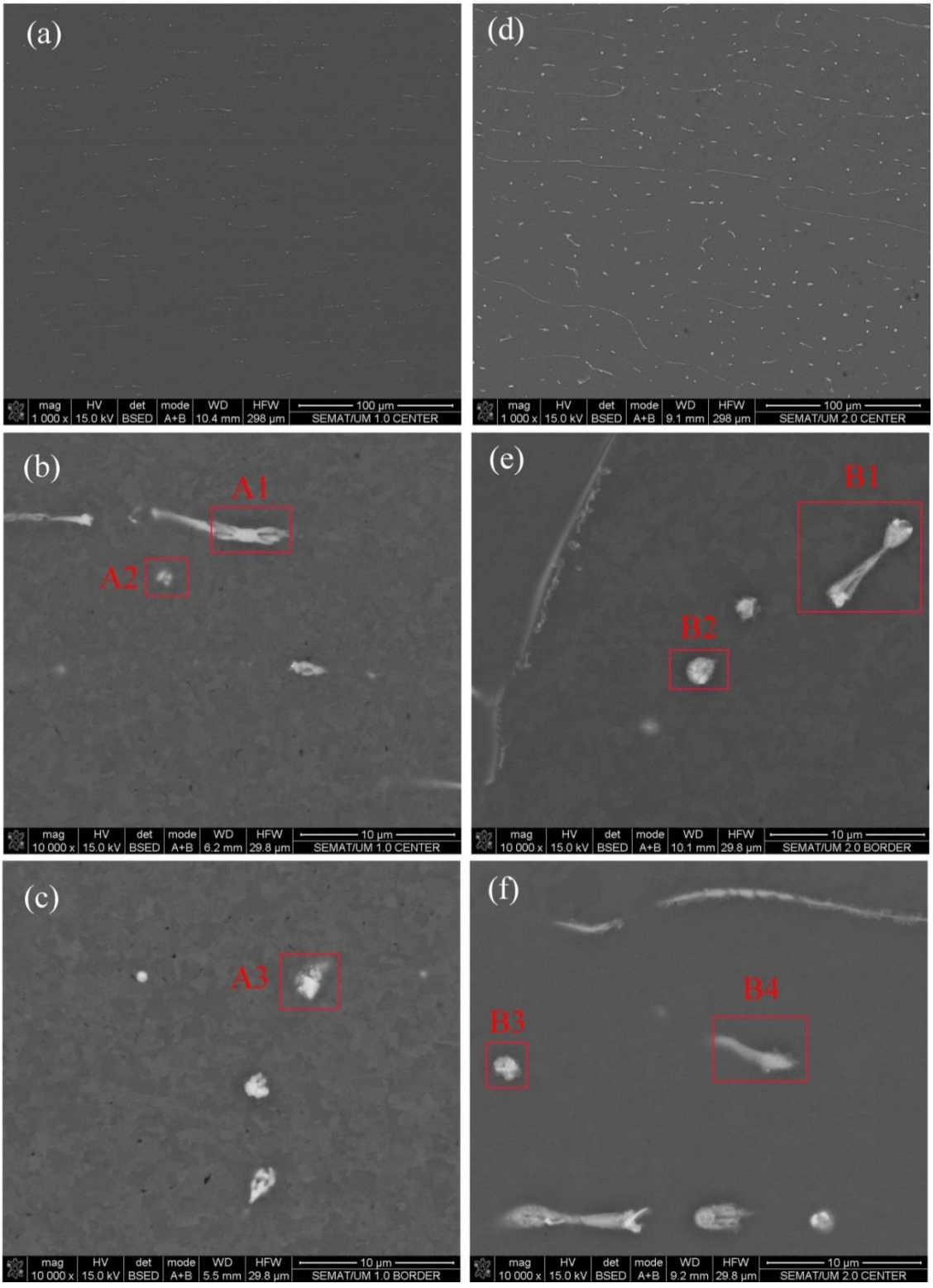

Figure 6.1. SEM micrographs of Al–0.28Sc alloy (a–b–c) and Al–0.24Sc–0.07Yb alloy (d–e–f).

Table 6.1. Chemical compositions of intermetallic particles in Al–0.28Sc and Al–0.24Sc–0.07Yb alloys

Intermetallic Particle		Al (wt%)	Sc (wt%)	Yb (wt%)	Fe (wt%)	Si (wt%)	Cu (wt%)
Al–0.28Sc	A1	87.31	1.97	-	8.06	2.67	-
	A2	89.92	1.31	-	7.49	1.28	-
	A3	91.9	-	-	8.1	-	-
Al–0.24Sc–0.07Yb	B1	78.28	0.67	5.24	9.7	2.33	3.77
	B2	79.27	0.8	4.0	10.14	2.93	2.86
	B3	76.76	1.31	6.64	9.01	3.94	2.35
	B4	83.36	0.55	3.27	9.97	-	2.86

6.1.1.2 Corrosion test

i) Immersion tests

Fig. 6.2 shows the evolution of the OCP with immersion time for Al–0.28Sc and Al–0.24Sc–0.07Yb alloys (as-cast and heat treated samples) in 3.5 wt% NaCl solution.

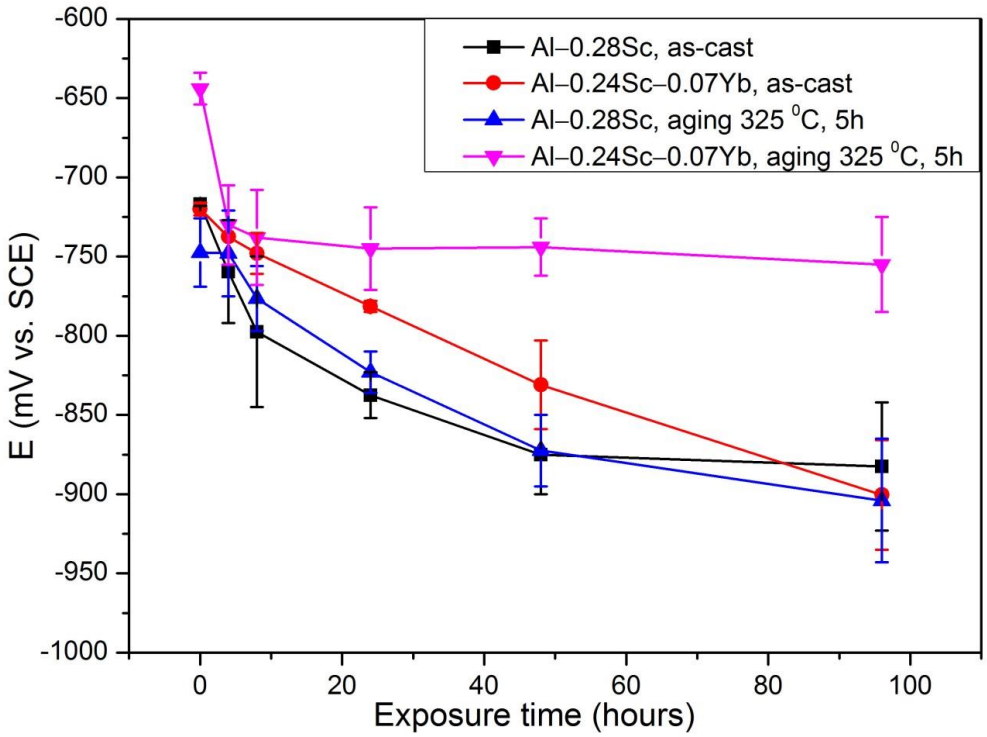

Figure 6.2. Evolution of OCP with time for Al–0.28Sc and Al–0.24Sc–0.07Yb alloys (as-cast and heat treated samples).

After exposing all samples to 3.5 wt% NaCl solution the OCP starts to decrease as a consequence of the initiation of pits. After 4 days of immersion, the OCP of Al–0.28Sc (as-cast and heat treated samples)

and Al–0.24Sc–0.07Yb (as-cast sample) were measured as –883 ± 41, –901 ± 35, and –904 ± 39 mV vs. SCE, respectively. There was no significant difference between these values suggesting the similarity in thermodynamic tendency of these alloys to electrochemical oxidation in 3.5 wt% NaCl solution. The OCP of Al–0.24Sc–0.07Yb heat treated sample stabilized quickly at –755 ± 30 mV vs. SCE after 4 hours of immersion. The OCP of Al–0.24Sc–0.07Yb heat treated sample is more noble (shift to positive value) than that of other samples. It indicated that the addition of Yb and age-hardening heat treatment decreases the susceptibility to corrosion in Al–Sc alloy.

Fig. 6.3 shows the representative SEM micrographs of Al–0.28Sc as-cast and heat treated samples exposed for 4 days in 3.5 wt% NaCl solution. Chemical compositions of three selected intermetallic particles were determined by EDS and listed in Table 6.2. The particles marked as "C1" contain Al and Fe, the particle "C2" contains Al, Sc, and Fe, and the particle "C4" contain Al, Sc, Fe, and Si. The dissolution of the matrix surrounding these Fe–containing intermetallic phases was observed. These particles are more noble in comparison with the matrix that can act as cathodes that may cause galvanic coupling with the surrounding matrix as well as an increase on pH due to hydroxyl ions forming during oxygen reduction reaction [17,18]. As a consequence, the dissolution of the matrix at the periphery of these particles may occur. The composition in the grain boundary (the area marked as "C3") was also analyzed. Fe and Sc segregated on the grain boundary and promoted a slight dissolution of the matrix at these sites. Previous studies have demonstrated that Fe-containing intermetallic particles (such as Al_6Fe, Al_3Fe and $Al_{12}Fe_3Si_2$, etc...) can act as cathodes compared to the matrix and promote the preferential dissolution of the surrounding matrix [17-25]. The corrosion product still remained after cleaning the surface of Al–0.28Sc as-cast sample (Fig. 6.3(c)) that was detected as $Al(OH)_3$ [3]. Many pit cavities were observed in the microstructure of Al–0.28Sc heat treated sample. The presence of Al_3Sc nano-precipitates in Al–0.28Sc heat treated sample can accelerate the pitting propagation and therefore increase the pit growth rate and number of pit cavities.

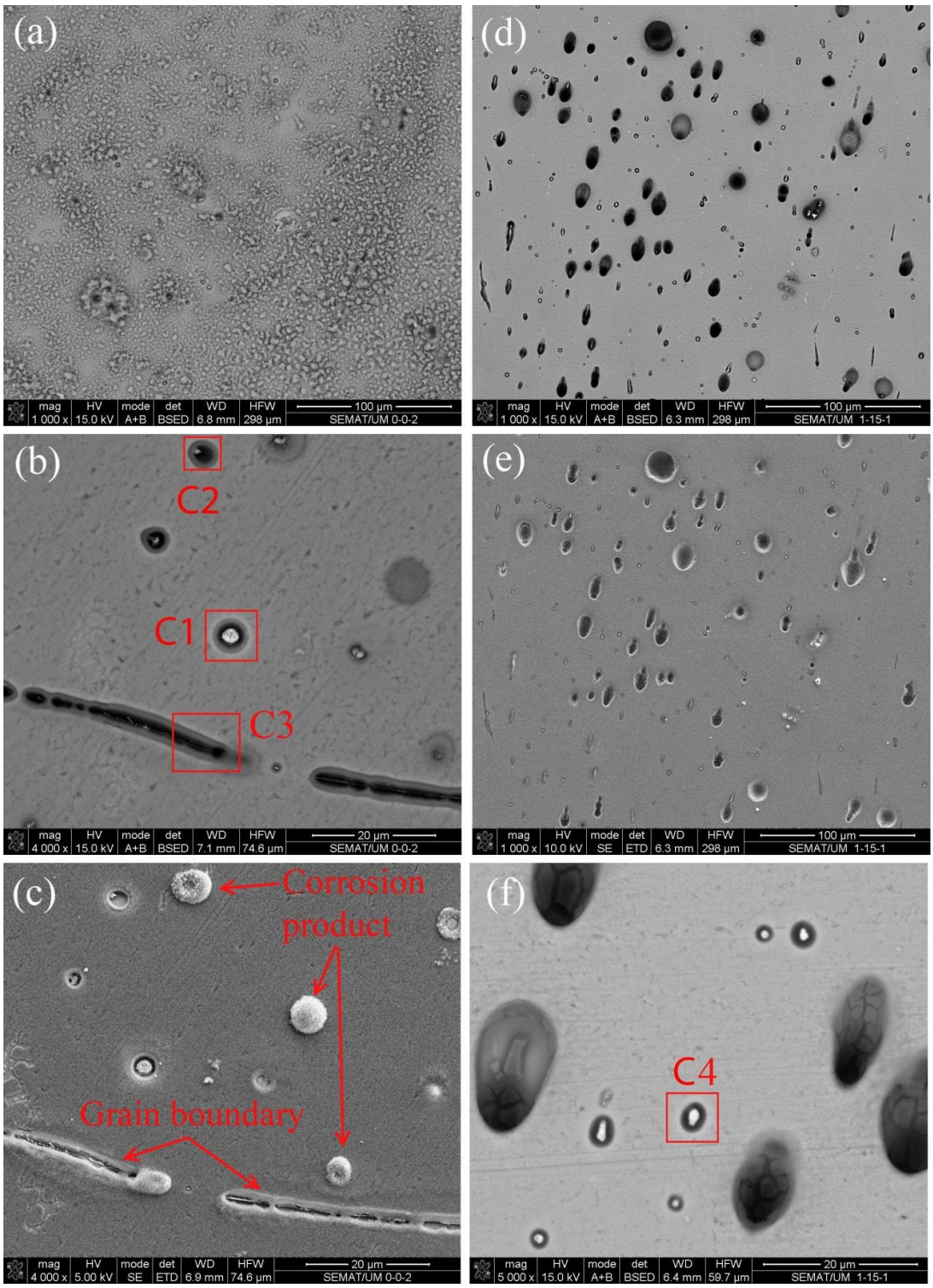

Figure 6.3. SEM micrographs of Al–0.28Sc alloy after immersion in 3.5 wt% NaCl solution for 4 days: (a–b–c) as-cast samples; (d–e–f) heat treated samples; (a–b–d–f) BSE images and (c–e) SE image.

Table 6.2. Chemical compositions of intermetallic particles in Al–0.28Sc alloy after immersion in a 3.5 wt% NaCl solution for 4 days

Particle		Al	Sc	Fe	Si	O
C1	wt%	78.77	-	3.69	-	17.54
	at%	71.52	-	1.62	-	26.86
C2	wt%	82.17	0.67	0.98	-	16.18
	at%	74.47	0.36	0.43	-	24.74
C3	wt%	72.71	1.27	1.75	-	24.27
	at%	63.09	0.66	0.73	-	35.52
C4	wt%	74.15	0.72	7.53	1.49	16.10
	at%	69.37	0.41	3.41	1.34	25.47

Fig. 6.4 shows SEM micrographs taken on Al–0.24Sc–0.07Yb as-cast and heat treated samples exposed for 4 days in 3.5 wt% NaCl solution at OCP. Chemical compositions of the particles labelled as "D1" (Al–Sc–Fe–Si intermetallic phase), "D2" (Al–Sc–Yb–Fe–Si intermetallic phase), "D3" (Al–Sc–Yb–Fe intermetallic phase), "D4" (Al–Sc–Fe intermetallic phase) and "C5" (grain boundary containing Al–Sc–Fe) after EDS analysis were given in Table 6.3. The dissolution of the matrix was observed clearly in the vicinity of the particles "D1", "D2" and slightly at the periphery of the particles "D3", "D4", and "D5". Some pit cavities present in the microstructure of Al–0.24Sc–0.07Yb heat treated sample. It can be seen the corrosion product ($Al(OH)_3$) deposited in the vicinity of pit cavities. In comparison with Al–0.28Sc heat treated sample, the number of pit cavities in the Al–0.24Sc–0.07Yb heat treated sample was much lower.

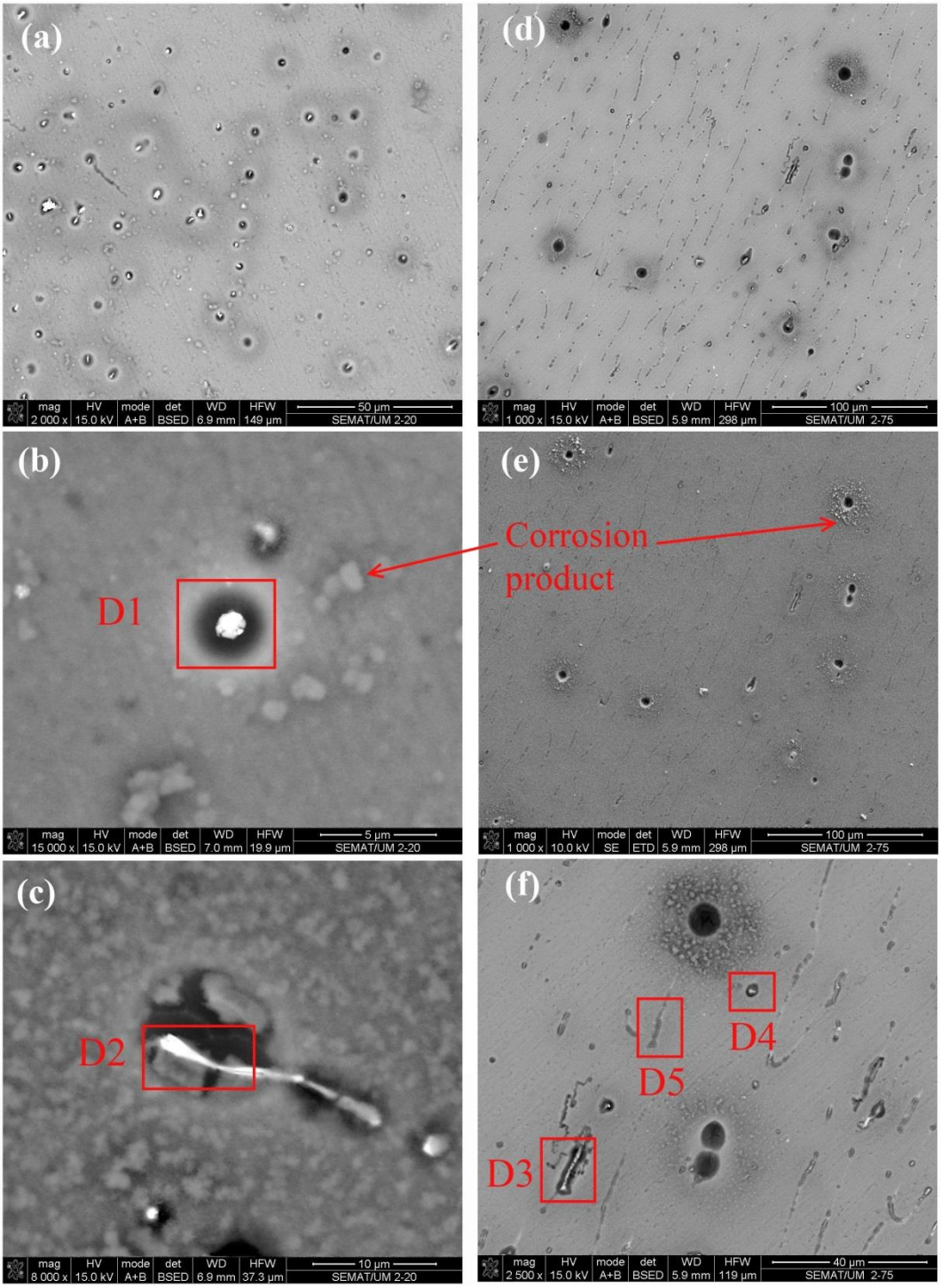

Figure 6.4. SEM micrographs of Al–0.24Sc–0.07Yb alloy after immersion in 3.5 wt% NaCl solution for 4 days: (a–b–c) as-cast samples; (d–e–f) heat treated samples.

Table 6.3. Chemical compositions of intermetallic particles in Al–0.24Sc–0.07Yb alloy after immersion in a 3.5 wt% NaCl solution for 4 days

Particle		Al	Sc	Yb	Fe	Si	O
D1	wt%	76.32	0.99	-	10.57	1.28	10.84
	at%	75.16	0.59	-	5.03	1.21	18.01
D2	wt%	53.60	1.52	13.16	4.39	3.22	24.10
	at%	52.24	0.89	2.01	2.07	3.03	39.76
D3	wt%	65.57	0.53	5.46	4.44	-	24.00
	at%	59.96	0.29	0.78	1.96	-	37.01
D4	wt%	67.80	0.60	-	6.34	-	25.26
	at%	57.57	0.32	-	2.69	-	37.42
D5	wt%	81.05	0.49	-	1.97	-	16.49
	at%	73.61	0.27	-	0.87	-	25.26

ii) Potentiodynamic polarization behaviour

Representative potentiodynamic polarization curves of Al–0.28Sc and Al–0.24Sc–0.07Yb alloys (as-cast and heat treated samples) in 3.5 wt% NaCl solution are shown in the Fig. 6.5. Corrosion potential ($E_{(i=0)}$), corrosion current density (i_{corr}) and pitting potential (E_p) are listed in Table 6.4.

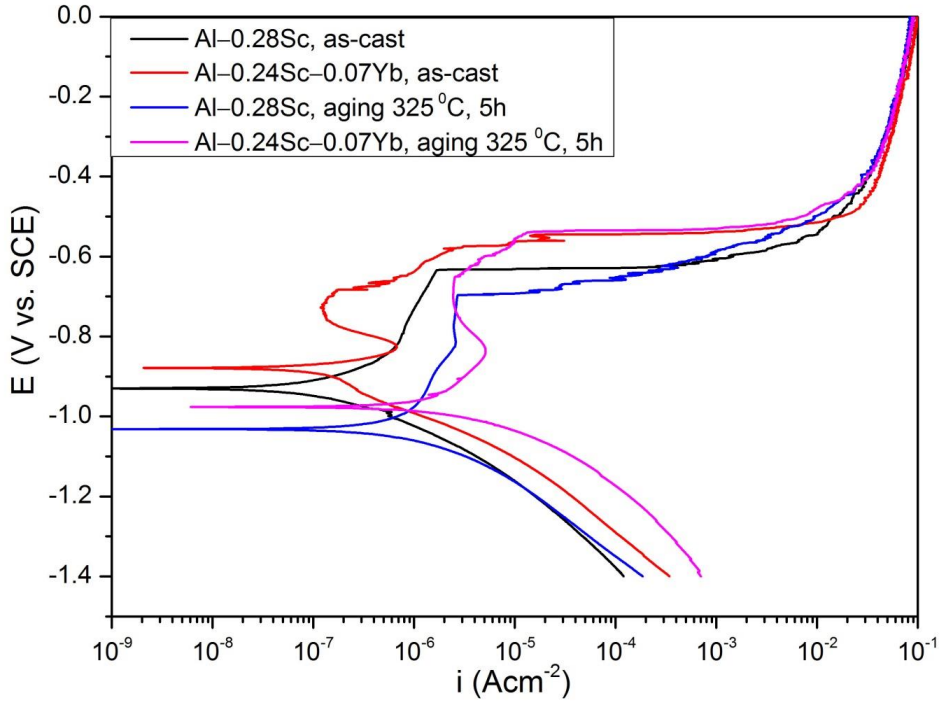

Figure 6.5. Potentiodynamic polarization curves obtained in 3.5 wt% NaCl solution for Al–0.28Sc and Al–0.24Sc–0.07Yb alloys (as-cast and heat treated samples).

Table 6.4. Summary of results of potentiodynamic polarization

Alloys	$E_{(i=0)}$ (mV)	i_{corr} (μAcm^{-2})	E_{pit} (mV)
Al-0.3Sc, as-cast	-956 ± 30	0.296 ± 0.139	-632 ± 42
Al-0.3Sc, aging325 °C, 5h	-1038 ± 8	1.913 ± 0.596	-679 ± 33
Al-0.24Sc-0.06Yb, as-cast	-884 ± 6	0.110 ± 0.02	-565 ± 24
Al-0.24Sc-0.06Yb, aging325 °C, 5h	-982 ± 9	3.281 ± 0.968	-521 ± 19

It can be seen that after the addition of Yb, the corrosion potential ($E_{i=0}$) of Al–0.24Sc–0.07Yb as-cast and heat treated samples were more positive than Al–0.28Sc as-cast and heat treated samples. It indicates that Al–0.24Sc–0.07Yb alloy presents lower tendency to corrosion in 3.5 wt% NaCl solution than Al–0.28Sc alloy. Yb addition and age-hardening heat treatment had strong effect on the polarization behavior in the anodic domain of Al–Sc alloy. The polarization curve in the anodic domain of Al–0.28Sc as-cast sample show the active corrosion followed by induced pitting. Al–0.28Sc heat treated samples presented active corrosion and passivation followed by induced pitting. On the other hand, Al–0.24Sc–0.07Yb as-cast and heat treated samples exhibited an active region due to metal oxidation with the increasing of current density as applied potential increases. Then, the current density tends to decrease with the increasing of applied potential to reach the passive current density. In the heat treated sample, the passive region was observed before a localized breakdown of passivity due to transpassive dissolution and pitting corrosion. At pitting potential, the current density rapidly increases. The pitting potentials of Al–0.28Sc as cast and heat treated samples are -632 ± 42 and -679 ± 33 mV vs. SCE, respectively. The pitting potentials of Al–0.24Sc–0.07Yb as cast and heat treated samples are -565 ± 24 and -521 ± 19 mV vs. SCE, respectively. The pitting potentials of Al–0.24Sc–0.07Yb alloy (both as-cast and heat treated samples) were more positive than that of Al–0.28Sc alloy. Thus, it can be stated that the addition of Yb improved the resistance to pitting corrosion of Al–0.28Sc alloy.

After age-hardening heat treatment, the corrosion potentials of Al–0.28Sc and Al–0.24Sc–0.07Yb alloys moved to negative direction and the corrosion current density increased significantly. The presence of Al_3Sc or $Al_3(Sc,Yb)$ precipitates can increase the susceptibility to corrosion and corrosion rate of these alloys. However, the passive plateau was clearly observed in the polarization curve of heat treated samples for both alloys. It is suggested that the age-hardening heat treatment enhances the passivation tendency of Al–0.28Sc and Al–0.24Sc–0.07Yb alloys during exposure to 3.5 wt% NaCl solution. This result is supported by the hypothesis proposed by Ahmad and Aleem [16]. The existence of a high

number density of nano–sized Al_3Sc or $Al_3(Sc,Yb)$ precipitates, which fully coherent with the matrix, leads to improvement of the passivity of heat treated samples.

Pitting corrosion in aluminium alloys is a complex process that depends on many factors such as temperature, pH, solution or the characteristics of microstructure and passive layer [26]. In this section, the pitting corrosion mechanisms in Al–0.28Sc and Al–0.24Sc–0.07Yb alloys exposure to 3.5 wt% NaCl solution were proposed. Aluminium alloys are susceptible to pitting corrosion due to the presence of intermetallic phases more noble than the matrix [20,21,23,27,28]. These particles can act as cathodes and cause the preferential dissolution of the surrounding matrix. In addition, the reduction reaction of water and oxygen leads to increase the local pH. The presence of OH^- ion can dissolve the protective oxide layer and promotes the formation of pits in the vicinity of these intermetallic particles (localized alkaline corrosion). Besides, the adsorption of aggressive Cl^- ion into the defective sites of the passive layer can trigger the pitting process [29]. Figure 6.6(a) shows the schematic view of the proposed corrosion process due to the presence of intermetallic phase and Cl^- ions aggression into the defective sites. The first image exhibits the cross-section of sample before immersion containing the intermetallic phases and a thin oxide layer. The second image shows cathodic and anodic possible reactions of corrosion process in the sample during exposure to the NaCl solution. The anodic reactions are the oxidation of Al and Sc and consequently lead to the preferential dissolution of the matrix. The cathodic reactions are water and oxygen reductions that cause the localized alkaline medium. The third image shows the pits at the periphery of intermetallic particles and a cavity in the sample after immersion. The surface of sample in the vicinity of intermetallic particles and cavities is covered by corrosion production depositions. Besides, the localized alkaline corrosion could completely occur in the surrounding matrix of the intermetallic particles and cause a cavity due to the detachment of these particles [29]. The schematic of this hypothesis is shown in Figure 6.6 (b).

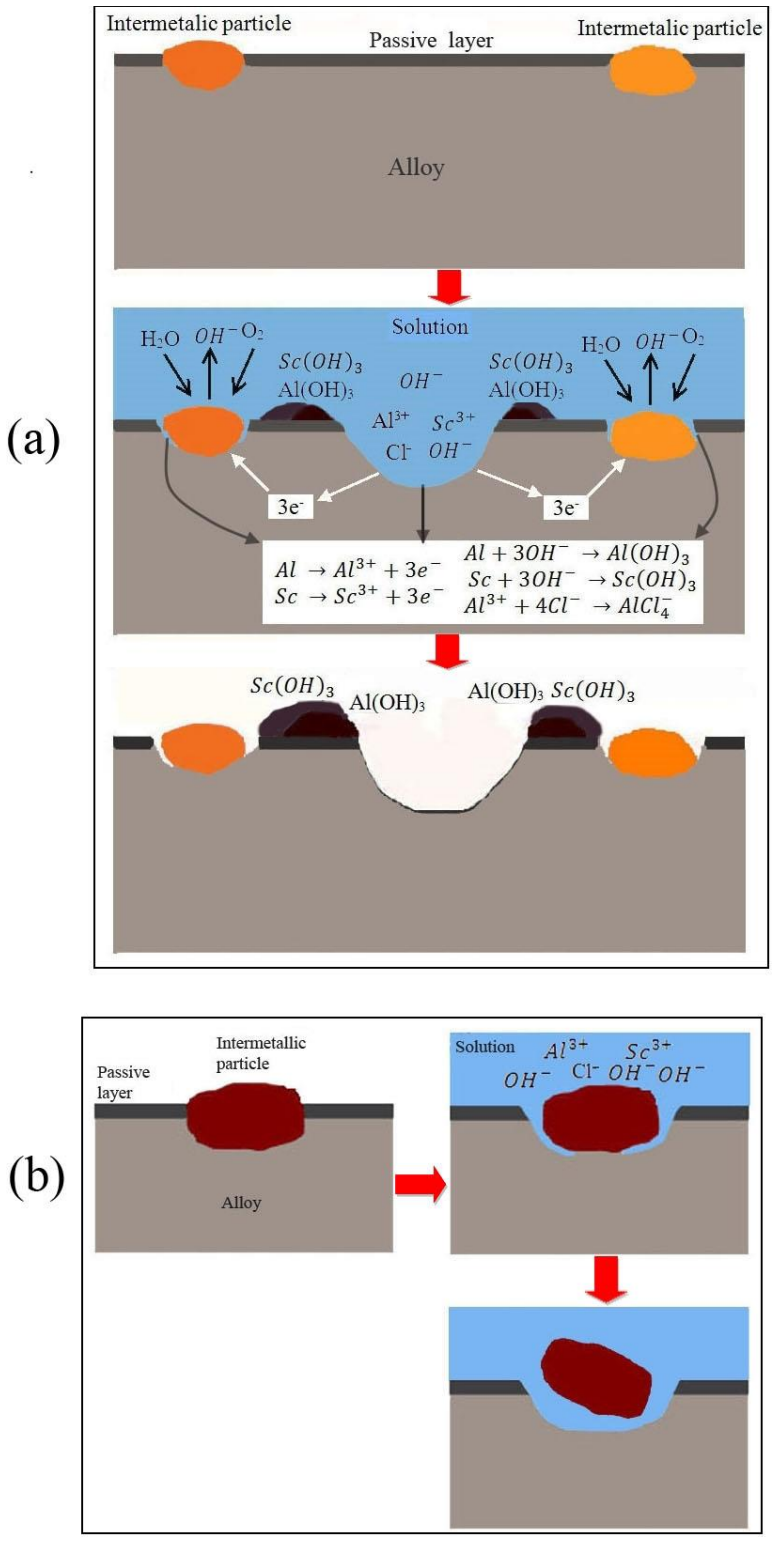

Figure 6.6. (a) Schematic view of the corrosion process: sample before immersion, corrosion reactions in the NaCl solution, and sample after exposure to the solution; (b) Schematic view of the cavity formation by localized alkaline corrosion.

6.1.2 The effect of Sc and Yb microalloying additions and aged-hardening heat treatment on corrosion behaviour of Al–Mg alloys

6.1.2.1 Impurity intermetallic particles

Iron, copper and silicon are common impurities in aluminium alloys. Intermetallic particles could be formed by alloying elements and those impurity elements play a crucial role in localized corrosion of Al alloys. Before exposure of samples to the 3.5 wt% NaCl solution, their microstructure was characterized by SEM and EDS. The morphologies and chemical elements of intermetallic particles were observed and analysed. Fig. 6.7 shows the SEM micrographs and EDS spectra of Al–4Mg alloy. Two second phase intermetallic particles were detected: bright particles (particle marked as "Z1") with needle-like shape contain Al, Mg, Si, and Fe and Chinese script dark particles (particle marked as "Z2") contain Mg, Al, and Si.

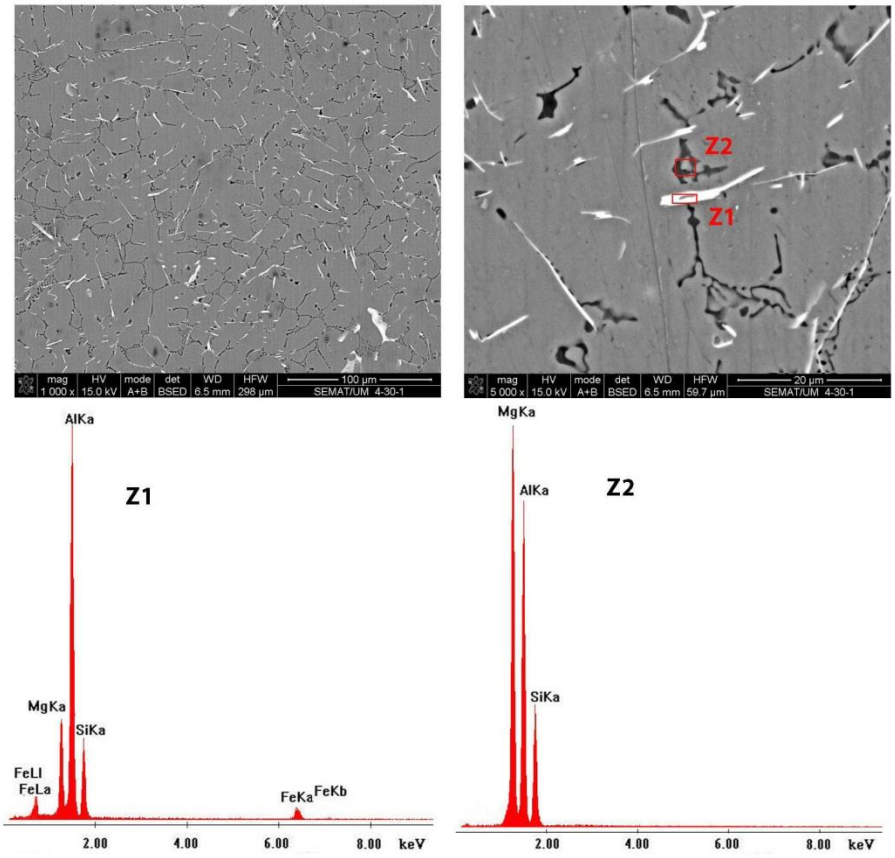

Figure 6.7. SEM micrographs and EDS spectra of intermetallic phases in Al–4Mg alloy.

Chinese script dark particles were observed in the grain boundaries. Fig. 6.8 and Fig. 6.9 exhibit the SEM micrographs and EDS spectra of Al–4Mg–0.3Sc and Al–4Mg–0.24Sc–0.06Yb alloys, respectively. The size of the impurity intermetallic particles dramatically decreased to 0.5–4 μm when adding Sc and Yb to Al–4Mg alloy. Three types of second-phase particles with different chemical compositions were detected in Al–4Mg–0.3Sc alloy: Al–Mg–Si–Fe (particle marked as "Z3"), Al–Mg–Sc–Si–Fe (particle marked as "Z4") containing intermetallic particle and oxide particle (particle marked as "Z5"). Oxide

particle could be $MgAl_2O_4$ that was formed during casting due to the high affinity of Mg with oxygen [30]. Another intermetallic particle containing Al, Mg, Sc, Si, Fe, and Yb ("Z6" particle) was observed in Al–4Mg–0.24Sc–0.06Yb alloy. These intermetallic phases were also detected in the microstructures of heat treated alloys because these phases are generally unaffected by heat treatment.

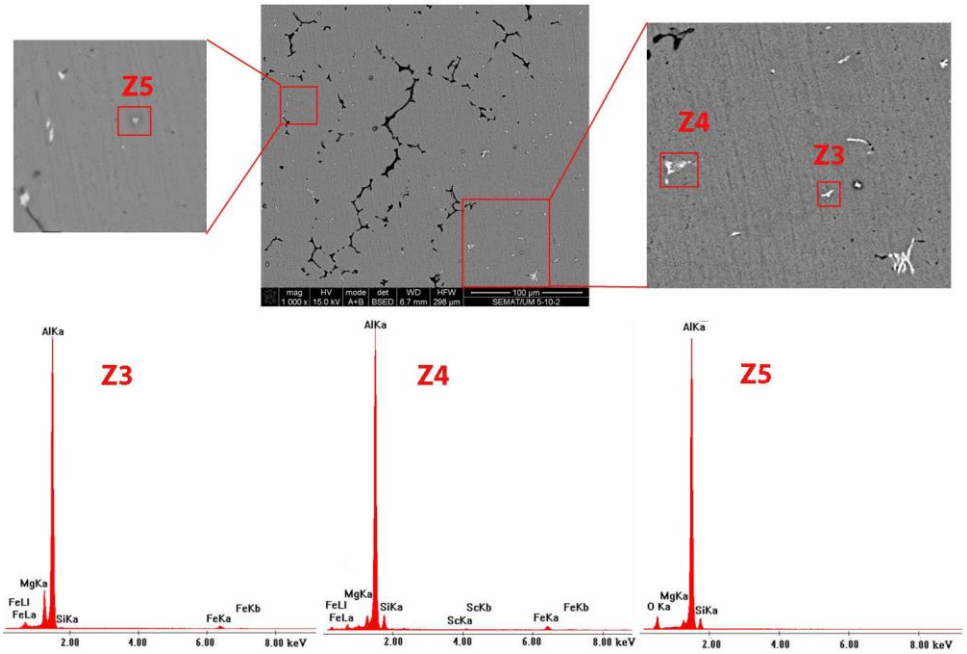

Figure 6.8. SEM micrographs and EDS spectra of intermetallic phases in Al–4Mg–0.3Sc alloy.

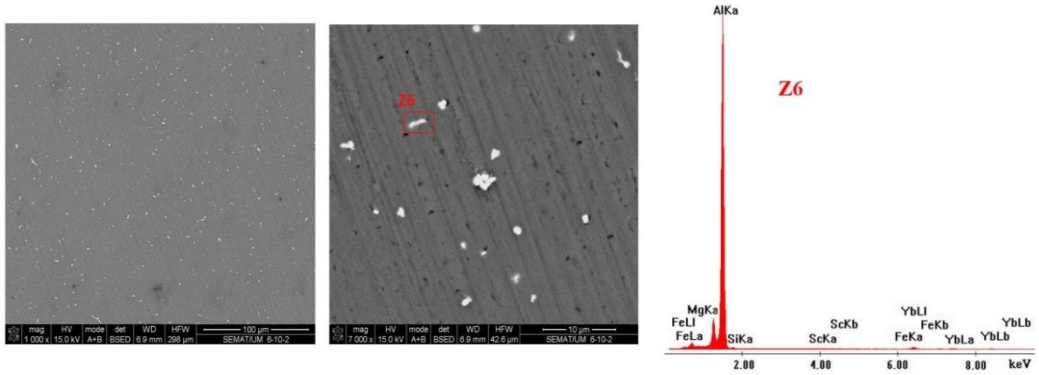

Figure 6.9. SEM micrographs and EDS spectra of intermetallic phases in Al–4Mg–0.24Sc–0.06Yb alloy.

6.1.2.2 Corrosion tests

i) Immersion tests

The OCP indicates the thermodynamic tendency of a material to electrochemical oxidation in a corrosive environment. During immersion, the nature of the sample surface changes due to oxidation or passive film formation and consequently alters the OCP of sample. The OCP will stabilize around a stationary value after a period of immersion. Fig. 6.10 shows the evolution of the OCP with time for Al–4Mg, Al–4Mg–0.3Sc and Al–4Mg–0.24Sc–0.06Yb alloys (as-cast and heat treated samples) immersed in3.5 wt% NaCl solution.

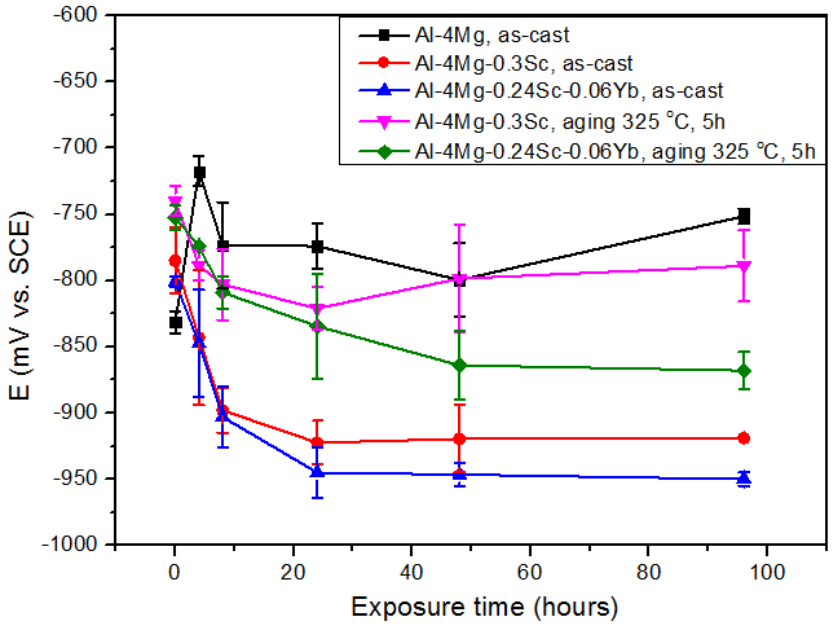

Figure 6.10. Evolution of OCP values with time for Al–4Mg, Al–4Mg–0.3Sc and Al–4Mg–0.24Sc–0.06Yb alloys (as-cast and heat treated samples).

In the beginning period of immersion, the OCP values presented large oscillations. Over longer periods of exposure, the OCP decreased and reached relatively stable values. The OCP becomes less and less noble can be explained by the initiation of pitting. Al alloys tend to pitting corrosion in presence of chlorides ions at a pH close to neutrality. The passive film dissolves to form Al^{3+} and reduces its protection ability. The OCP decreases with the increase of the dissolution rate. The OCP of Al–4Mg, Al–4Mg–0.3Sc and Al–4Mg–0.24Sc–0.06Yb as-cast samples stabilized at –774 ± 33, –923 ± 17, and –945 ± 19 mV vs. SCE after 8, 24, and 24 hours of immersion, respectively. The OCP of Al–4Mg–0.3Sc and Al–4Mg–0.24Sc–0.06Yb heat treated samples stabilized at –789 ± 27 and –864 ± 26 mV vs. SCE after 48 hours of immersion, respectively. It can be seen that the OCP of Al–4Mg became less noble (more negative) by adding Sc and Yb. This indicated that Al–4Mg–0.3Sc and Al–4Mg–0.24Sc–0.06Yb as-cast alloy have a higher susceptibility to corrosion in comparison with Al–4Mg alloy. However, the OCP of Al–4Mg–0.3Sc and Al–4Mg–0.24Sc–0.06Yb heat treated alloys was more positive than the as-cast

alloys, indicating higher tendency to corrosion in heat treated alloys than as-cast alloys. The presence of high number density of Al_3Sc precipitates as a result of age-hardening heat treatment increases the cathodic reactivity of the surface, thereby increasing the OCP of heat treated alloys.

Fig. 6.11 shows representative SEM micrographs at the corroded surfaces taken on Al–4Mg sample exposed for 4 days in 3.5 wt% NaCl solution at OCP.

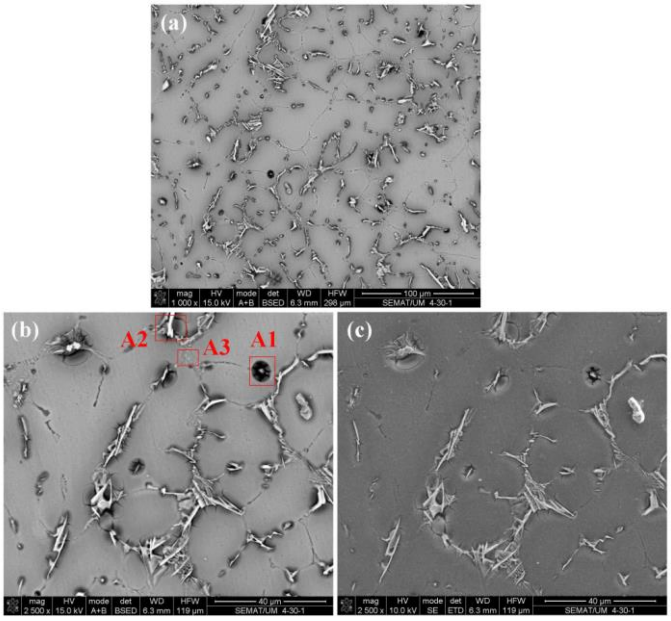

Figure 6.11. SEM micrographs of Al–4Mg alloy after immersion in 3.5 wt% NaCl solution for 4 days: (a–b) BSE images and (c) SE image.

Chemical compositions of three selected intermetallic particles were determined by EDS and the results are given in Table 6.5.

Table 6.5. Chemical compositions of intermetallic particles in Al–4Mg alloy after immersion in 3.5 wt% NaCl solution for 4 days

Particle		Al	Mg	Fe	Si	O
A1	wt%	61.04	2.76	6.44	17.72	12.04
	at%	58.39	2.93	2.98	16.28	19.42
A2	wt%	59.28	1.21	16.17	12.84	10.50
	at%	60.19	1.37	7.93	12.53	17.98
A3	wt%	68.86	10.11	-	8.37	12.66
	at%	62.91	10.25	-	7.34	19.51

The particles labelled as “A1” and “A2” contain Al, Mg, Fe, and Si whereas the particle labelled as “A3” contain Al, Mg, and Si. It is evident to observe the dissolution of the matrix at the periphery of the

Al–Mg–Fe–Si containing particles. These particles are nobler than the matrix thus can act as cathodes and support oxygen reduction to form hydroxyl ions. The galvanic coupling between the noble particles and the surrounding matrix was established. Furthermore, it has been reported that a local pH at these particles can increase and promotes grooving of the surrounding matrix by alkaline dissolution [17,18]. On the other hand, corrosion was not observed in the vicinities of the Al–Mg–Si containing particles. Birbilis and Buchheit [18] reported a survey of corrosion potentials and electrochemical characteristics for intermetallic particles commonly present in high-strength aluminium-based alloys. Corrosion potentials of Mg–containing intermetallic phases are between corrosion potential of pure Al (–823 mV vs. SCE in 0.1 M NaCl solution) and pure Mg (–1586 mV vs. SCE in 0.1 M NaCl solution). According to Birbilis and Buchheit, corrosion potentials of Mg–containing intermetallic phases are more negative than Al matrix and other intermetallic phases. Therefore, these phases are active to the matrix and can act as anode leading to dissolution or Mg dealloying when exposed in NaCl solution. This mechanism has also been confirmed by some previous researches [28,31,32]. However different Mg–containing intermetallic phases show the different phenomena due to the different dissolution rates and the presence of noble elements.

Mg–containing intermetallic phases with high self-dissolution rates lead to an anodic dissolution at high rates. The local alkalization appears and can dissolve the Al matrix in the vicinity of intermetallic particles [28]. In the Mg–containing intermetallic particle with a noble elemental such as Al_2CuMg, Mg and Al selectively dissolve and the dealloying particle remnant can act as cathode. The peripheral pits around the particle occur due to the alkaline dissolution or galvanic corrosion [28]. In the present study, the Al–Mg–Si containing particles in Al–4Mg alloy are not any case listed above. We proposed that Al–Mg–Si containing phase has a low self-dissolution rate. Therefore, there is no preferential dissolution of the matrix surrounding Al–Mg–Si containing particles.

Fig. 6.12 shows representative SEM micrographs taken on Al–4Mg–0.3Sc as-cast and heat treated samples exposed for 4 days in 3.5 wt% NaCl solution at OCP. Two intermetallic phases were detected. The Al–Mg–Sc–Si–Fe containing intermetallic particle labelled as “B1”, “B2”, “B4” and Al–Mg–Sc–Fe containing intermetallic particle labelled as “B3”. Both phases are Fe–containing intermetallic phases. The Al–Mg–Fe–Si containing intermetallic phase was not detected on the samples.

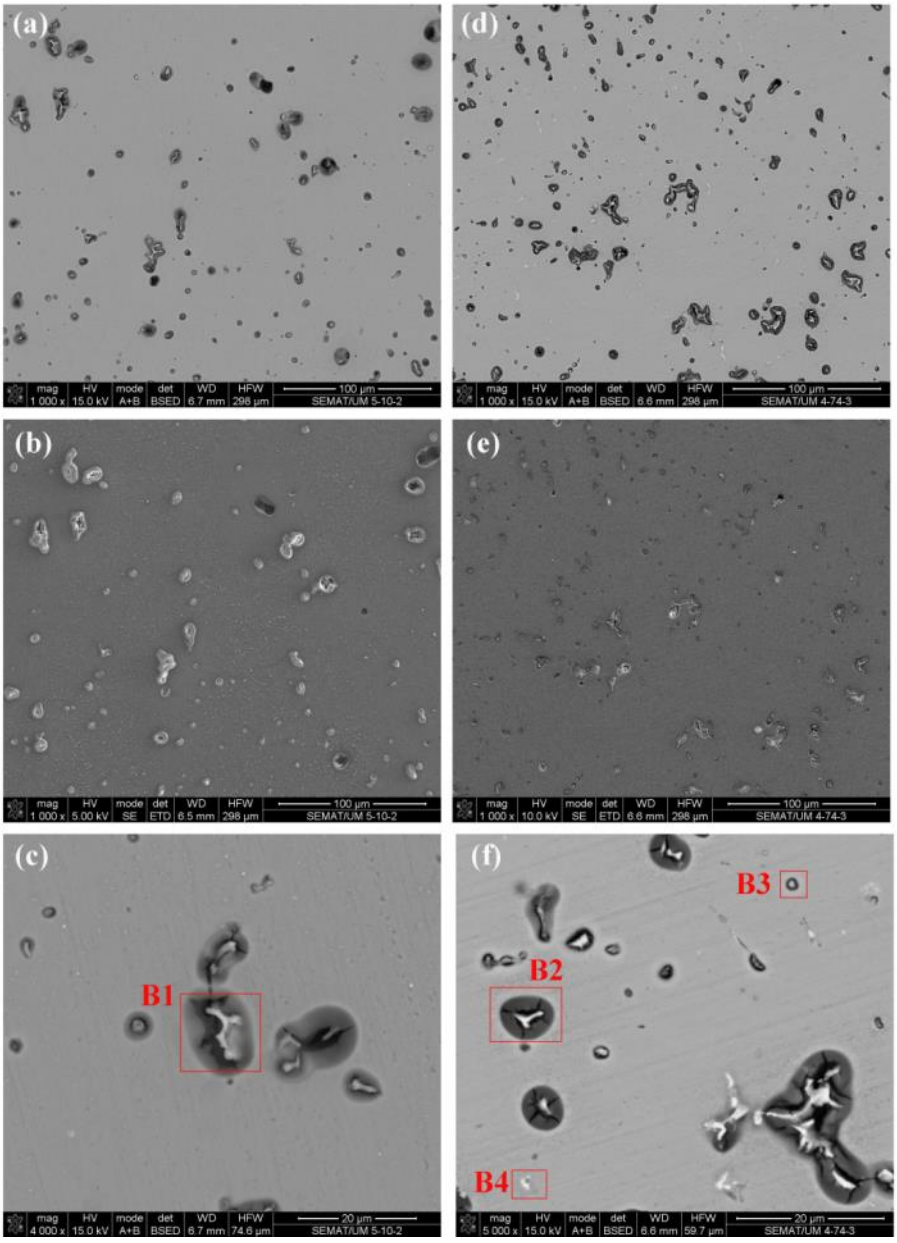

Figure 6.12. SEM micrographs of Al–4Mg–0.3Sc alloy after immersion in 3.5 wt% NaCl solution for 4 days: (a–b–c) as-cast samples; (d–e–f) heat treated samples; (a–c–d–f) BSE images and (b–e) SE image.

Chemical compositions of these intermetallic particles were determined by EDS and the results are listed in Table 6.6. It can be observed that the matrix dissolved heavily in the vicinity of the particles "B1" and "B2". A slight anodic dissolution of the matrix at the periphery of the particle "B3" was observed. No preferential dissolution of the matrix was detected around the particle "B4". Table 6.6. shows that the Mg content in these intermetallic particles increases gradually from the particles "B1" and "B2" to "B3" and maximum in the particle "B4". The presence of Mg in the Fe–containing intermetallic phases can reduce both anodic and cathodic rates, thus, the high content of Mg makes the Fe–containing intermetallic particle less noble to the matrix.

Table 6.6. Chemical compositions of intermetallic particles in Al–4Mg–0.3Sc alloy after immersion in 3.5 wt% NaCl solution for 4 days

Particle		Al	Mg	Sc	Fe	Si	O
B1	wt%	42.1	2.73	0.95	17.32	1.35	35.54
	at%	36.52	2.62	0.49	7.26	1.12	51.99
B2	wt%	58.17	1.72	0.83	14.12	1.11	24.04
	at%	53.36	1.76	0.45	6.26	0.98	37.19
B3	wt%	69.20	3.54	0.39	9.12	-	17.75
	at%	64.25	3.65	0.22	4.09	-	27.80
B4	wt%	74.83	5.63	0.56	10.46	1.18	7.34
	at%	74.84	6.25	0.33	5.06	1.13	12.39

Fig. 6.13 shows representative SEM micrographs taken on Al–4Mg–0.24Sc–0.06Yb as-cast and heat treated samples exposed for 4 days in 3.5 wt% NaCl solution at OCP.

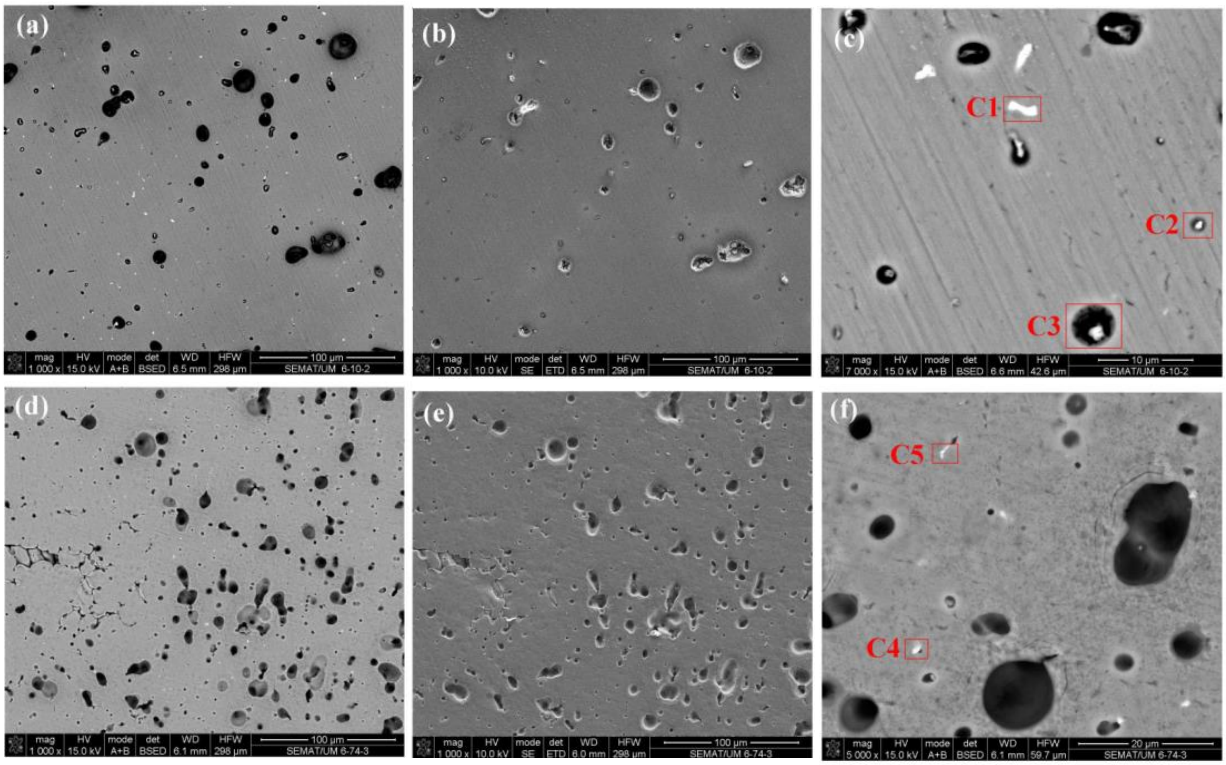

Figure 6.13. SEM micrographs of Al–4Mg–0.24Sc–0.06Yb alloy after immersion in 3.5 wt% NaCl solution for 4 days: (a–b–c) as-cast samples; (d–e–f) heat treated samples; (a–c–d–f) BSE images and (b–e) SE image.

Chemical compositions of the particles labelled as “C1” and “C4” (Al–Mg–Sc–Yb intermetallic phase), “C2” (Al–Mg–Sc–Yb–Fe–Si intermetallic phase), “C3” (Al–Mg–Sc–Fe–Si intermetallic phase), and “C5”

(Al–Mg–Sc–Yb–Fe intermetallic phase) and the results are given in Table 6.7. It can be seen that the Yb–containing intermetallic phases did not lead to corrosion in the vicinity of their particles ("C1", "C4", and "C5") or a slight dissolution of the surrounding matrix was observed ("C2"). However, the high content of Fe in the particle "C3" (Al–Mg–Sc–Fe–Si intermetallic phase) promote heavily dissolution of the matrix in the vicinity of this particle. The pitting cavities were observed in both as-cast and heat treated samples of Al–4Mg–0.24Sc–0.06Yb alloy. The number of pitting cavities was significantly increased in heat treated sample.

Table 6.7. Chemical compositions of intermetallic particles in Al–4Mg–0.24Sc–0.06Yb alloy after immersion in 3.5 wt% NaCl solution for 4 days

Particle		Al	Mg	Sc	Yb	Fe	Si	O
C1	wt%	71.77	14.08	0.41	10.55	-	-	3.19
	at%	75.81	16.51	0.26	1.74	-	-	5.68
C2	wt%	74.40	4.08	0.41	9.04	1.19	0.38	10.5
	at%	74.98	4.56	0.25	1.42	0.58	0.37	17.84
C3	wt%	60.85	4.06	0.53	-	12.16	0.65	21.76
	at%	55.90	4.14	0.29	-	5.39	0.57	33.70
C4	wt%	71.50	10.74	0.36	15.49	-	-	1.91
	at%	80.09	13.35	0.24	2.71	-	-	3.61
C5	wt%	78.29	4.92	0.45	12.19	2.42	-	1.73
	at%	86.98	6.07	0.30	2.11	1.30	-	3.24

ii) Potenciodynamic polarization behaviour

Representative potentiodynamic polarization curves of Al–4Mg, Al–4Mg–0.3Sc and Al–4Mg–0.24Sc–0.06Yb alloys (as-cast and heat treated samples) in 3.5 wt% NaCl solution are shown in the Fig. 6.15 and corrosion potential ($E_{(i=0)}$), corrosion current density (i_{corr}), and pitting potential (E_p) are listed in the Table 6.8.

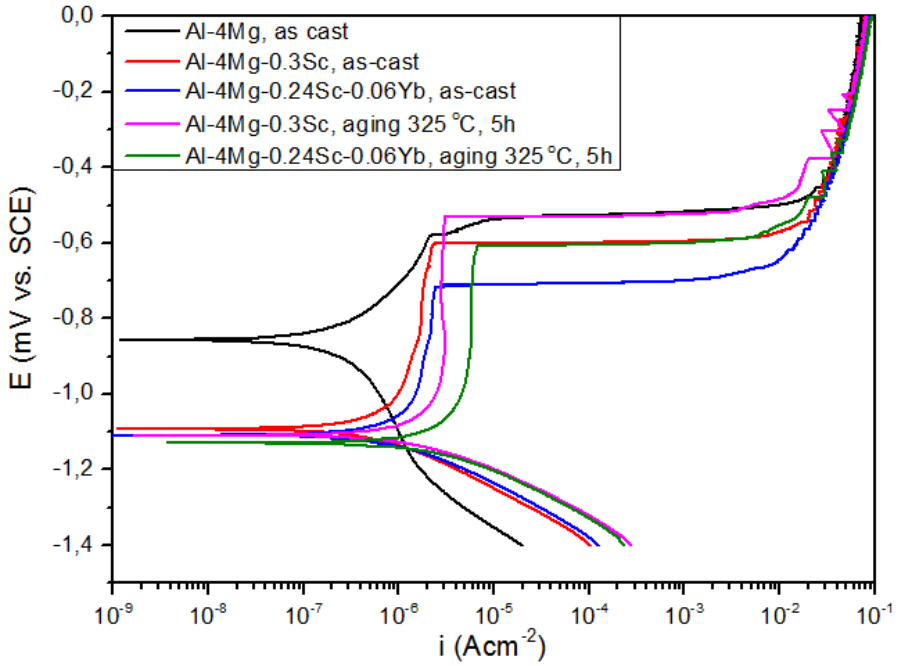

Figure 6.14. Potentiodynamic polarization curves obtained in 3.5 wt% NaCl solution for Al–4Mg, Al–4Mg–0.3Sc and Al–4Mg–0.24Sc–0.06Yb alloys (as-cast and heat treated samples).

Table 6.8. Summary of results of potentiodynamic polarization

Alloys	$E_{(i=0)}$ (mV)	i_{corr} (μAcm^{-2})	E_{pit} (mV)
Al–4Mg, as-cast	-851 ± 17	1.99 ± 0.83	-530 ± 45
Al–4Mg–0.3Sc, as-cast	-1100 ± 33	1.9 ± 0.61	-643 ± 57
Al–4Mg–0.3Sc, aging 325 °C, 5h	-1110 ± 7	3.06 ± 0.55	-527 ± 52
Al–4Mg–0.24Sc–0.06Yb, as-cast	-1123 ± 13	1.68 ± 0.33	-670 ± 52
Al–4Mg–0.24Sc–0.06Yb, aging 325 °C, 5h	-1125 ± 9	4.29 ± 0.50	-591 ± 29

It can be seen that corrosion potential of Al–4Mg alloy is more positive than Al–4Mg–0.3Sc and Al–4Mg–0.24Sc–0.06Yb alloys (as-cast and heat treated samples). The addition of Sc and Yb increased the corrosion tendency of Al–4Mg alloy in 3.5 wt% NaCl solution. The heat treatment did not change the corrosion potential of Al–4Mg–0.3Sc and Al–4Mg–0.24Sc–0.06Yb alloys significantly. It is known that Sc is electrochemically active in both solid solution and the Al_3Sc intermetallic form [33]. This characteristic can promote the active dissolution of alloys. The presence of new impurity intermetallic phases in Al–4Mg–0.3Sc and Al–4Mg–0.24Sc–0.06Yb alloys also plays an important role by increasing the corrosion tendency. The cathodic current density increased significantly by the addition of Sc and Yb to Al–4Mg alloy and by the heat treatment of Al–4Mg–0.3Sc and Al–4Mg–0.24Sc–0.06Yb alloys, whereas, the corrosion current density was not significantly affected by the addition of Sc and Yb.

However, the heat treatment increased the corrosion current density of Al–4Mg–0.3Sc and Al–4Mg–0.24Sc–0.06Yb alloys. Faraday's law indicated that the electrochemical corrosion rate is proportional with the corrosion current density. Thus, the corrosion rate of Al–4Mg–0.3Sc and Al–4Mg–0.24Sc–0.06Yb alloys was increased after heat treatment. The highest corrosion current density was observed in the Al–4Mg–0.24Sc–0.06Yb heat treated sample. This value is in accordance with the high amount of pits that was observed in the SEM micrographs of Al–4Mg–0.24Sc–0.06Yb heat treated sample after immersion for 4 days in 3.5 wt% NaCl solution (Fig. 6.13(d) and Fig. 6.13(e)).

The polarization curve in the anodic domain of as-cast Al–4Mg alloy shows the active corrosion followed by induced pitting where a passive plateau was not observed. The polarization curves of Al–4Mg–0.3Sc and Al–4Mg–0.24Sc–0.06Yb alloys (as-cast and heat treated samples) show a spontaneous passivation before a distinctly breakdown by pitting corrosion. The dissolution in a neutral solution is given by [28]:

$$Al \rightarrow Al^{3+} + 3e^{-} \quad (1)$$

$$Mg \rightarrow Mg^{2+} + 2e^{-} \quad (2)$$

$$Sc \rightarrow Sc^{3+} + 3e^{-} \quad (3)$$

$$Al + 3OH^{-} \rightarrow Al(OH)_3 \quad (4)$$

$$Sc + 3OH^{-} \rightarrow Sc(OH)_3 \quad (5)$$

And the cathodic reactions are given by:

$$2H_2O + 2e^{-} \rightarrow H_2 \uparrow + 2OH^{-} \quad (6)$$

$$O_2 + 2H_2O + 4e^{-} \rightarrow 4OH^{-} \quad (7)$$

In Al–4Mg alloy, the films of bayerite and boehmite ($Al_2O_3.3H_2O$, $Al_2O_3.H_2O$) can be formed but it is not stable and easy to breakdown by the presence of large impurity intermetallic particles (Fig. 6.7). In Al–4Mg–0.3Sc and Al–4Mg–0.24Sc–0.06Yb alloys, hydrated Sc_2O_3 is accumulated to form the duplex film with bayerite and boehmite [1,9,16,33]. This duplex film is less defective and more stable than bayerite and boehmite films. Therefore it enhances the passivity of Al–4Mg–0.3Sc and Al–4Mg–0.24Sc–0.06Yb alloys.

In comparison with the as-cast samples, the passive domain of the heat treated samples dramatically increased. It indicated that the passive film formed in the heat treated samples is more stable than the as-cast samples. This behaviour can explain by the more noble OCP values of the heat treated samples in comparison with the as-cast samples (Section 6.2.2.2(a)). The pitting potentials of Al–4Mg, Al–4Mg–0.3Sc, and Al–4Mg–0.24Sc–0.06Yb as-cast samples are −530 ± 45, −643 ± 57, and −670 ± 52 mV vs. SCE, respectively. The values for Al–4Mg–0.3Sc and Al–4Mg–0.24Sc–0.06Yb heat treated samples are

−527 ± 52 and −591 ± 29 mV vs. SCE, respectively. The pitting potential of Al–4Mg alloy decreased with the addition of Sc and continues decreasing with adding Yb. However, the pitting potentials of Al–4Mg–0.3Sc and Al–4Mg–0.24Sc–0.06Yb alloys after heat treatment shifted to more positive values and are close to the value of Al–4Mg alloy. Thus, the addition of Sc and Yb to Al–4Mg tended to increase the pitting corrosion tendency, whereas heat treatment lead to an improvement of the resistance to pitting corrosion of Al–4Mg–0.3Sc and Al–4Mg–0.24Sc–0.06Yb alloys. After heat treatment, a high number density (as high as 10^{22} m^{3}) of nano–sized Al_3Sc or $Al_3(Sc,Yb)$ precipitates that fully coherent with the matrix were formed [34]. The duplex film of Sc_2O_3 reinforced Al_2O_3 is formed throughout the samples even on the precipitates sites. This passive film formed on the precipitates also coherent with the matrix. It was observed that the nano–sized precipitates did not introduce any discontinuities in the passive film. It is well known that the localized corrosion will attack at the interface between intermetallic particles and matrix. These intermetallic particles must be noble and cathodic to the matrix. In Al–4Mg–0.3Sc and Al–4Mg–0.24Sc–0.06Yb alloys, these intermetallic particles are Fe–containing intermetallic phases (Section 6.2.2.2(a)). Cavanaugh *et al.* [8] indicated that Al_3Sc precipitates are inert to corrosion and slightly cathodic to the Al matrix. The presence of high number density of nano–sized Al_3Sc or $Al_3(Sc,Yb)$ precipitates around the Fe–containing intermetallic particles can increase the electrochemical compatibility of Fe–containing intermetallic particles with the matrix. As a consequence, it reduces the tendency to pitting corrosion in heat treated samples.

Finally, it can be seen that in comparison with Al–4Mg–0.3Sc and Al–4Mg–0.24Sc–0.06Yb as-cast samples, the heat treated samples have more stable passive film, higher pitting corrosion resistance but higher corrosion rate and pit growth rate. It can be acceptable according to the findings of Frankel *et al.* [35] where it has been indicated that the passive film does not play a fundamental role in pitting, it has a low contribution in pit growth resistance and pit growth depends on events occurring within pits.

6.2 Conclusions

The corrosion behaviour of Al–0.28Sc and Al–0.24Sc–0.07Yb, Al–4Mg, Al–4Mg–0.3Sc and Al–4Mg–0.24Sc–0.06Yb alloys in 3.5 wt% of NaCl solution was investigated by immersion and potentiodynamic polarisation analysis. Base on the results obtained from the present research, the following conclusions can be drawn:

a) For Al–0.28Sc and Al–0.24Sc–0.07Yb alloys:
   - The OCP evolution of these alloys during immersion in 3.5 wt% NaCl showed the lowest corrosion tendency in Al–0.24Sc–0.07Yb heat treated alloy.
   - The presence of Fe–containing intermetallic phases in these alloy promoted pitting corrosion.
   - The presence of a high number density of fully coherent nano–sized Al_3Sc or $Al_3(Sc,Yb)$ precipitates in heat treated alloy enhanced the passivity of these alloys.

b) For Al–4Mg, Al–4Mg–0.3Sc and Al–4Mg–0.24Sc–0.06Yb alloys:
   - The addition of Sc and Yb to Al–4Mg alloy reduced the size and changed the morphology of impurity intermetallic particles. The Fe–containing intermetallic particles are cathodic with respect to the matrix and can act as pitting initiation sites.
   - The high content of Mg makes the Fe–containing intermetallic particle less noble to the matrix. Yb–containing intermetallic particles did not show any dissolution of the matrix at the periphery of these particles.
   - The addition of Sc and Yb can decrease the susceptibility to corrosion of the heat treated Al–4Mg–0.3Sc and Al–4Mg–0.24Sc–0.06Yb alloys.
   - The active dissolution and pitting are dominant corrosion mechanisms in Al–4Mg alloy. More stable passive plateau and less susceptibility to pitting corrosion was observed in the polarization curves of Al–4Mg–0.3Sc and Al–4Mg–0.24Sc–0.06Yb alloys after heat treatment.

References

[1] Ganiev IN. High-Temperature and Electrochemical Corrosion of Aluminum-Scandium Alloys. Prot. Met. 1995;31:543-6.

[2] Sinyavskii VS, Val'kov VD, Titkova EV. The Effect of Scandium and Zirconium Additions on Corrosion Properties of Al-Mg Alloys. Prot.Met. 1998;34: 549-55.

[3] Ahmad Z, Ul-Hamid A, B.J A-A. The corrosion behavior of scandium alloyed Al 5052 in neutral sodium chloride solution. Corros. Sci. 2001;43:1227-43.

[4] Ahmad Z. Effect of Scandium Doping on The Corrosion Resistance and Mechanical Behavior of Al-3Mg Alloy in Neutral Chloride Solutions. Mater. Sci. Appl. 2011;02:244-50.

[5] Wu Y-L, Li C, Froes FH, Alvarez A. Microalloying of Sc, Ni, and Ce in an advanced Al-Zn-Mg-Cu alloy. Metall. Mater. Trans. A. 1999;30:1017-24.

[6] Deng Y, Yin Z, Zhao K, Duan J, Hu J, He Z. Effects of Sc and Zr microalloying additions and aging time at 120°C on the corrosion behaviour of an Al–Zn–Mg alloy. Corros. Sci. 2012;65:288-98.

[7] Wloka J, Virtanen S. Influence of scandium on the pitting behaviour of Al–Zn–Mg–Cu alloys. Acta Mater. 2007;55:6666-72.

[8] Cavanaugh MK, Birbilis N, Buchheit RG, Bovard F. Investigating localized corrosion susceptibility arising from Sc containing intermetallic Al3Sc in high strength Al-alloys. Scri. Mater. 2007;56:995-8.

[9] Neubert V, Smola B, Stulíková I, Bakkar A, Reuter J. Microstructure, mechanical properties and corrosion behaviour of dilute Al–Sc–Zr alloy prepared by powder metallurgy. Mater. Sci. Eng. A. 2007;464:358-64.

[10] Sinyavskii VS, Val'kov VD, Titkova EV. The effect of scandium and zirconium additions on corrosion properties of Al-Mg alloys. Prot.Met. 1998;34:549-55.

[11] Kharina GV, Kochergin VP. Corrosion-electrochemical behavior of Al-Zn-rem alloys in the presence of polyvanadate-ions. Prot.Met. 2001;37:575-9.

[12] Kharina GV, Kochergin VP. Corrosion of alloys of aluminum with zinc and rare earth metals in sodium metavanadate solutions. Prot.Met. 1996;32:134-6.

[13] Ganiev IN. Corrosion-Electrochemical Behavior of Special-Purity Aluminum and Its AK1 Alloy Alloyed with Scandium. Russ. J. Appl. Chem. 2004;77:925-9.

[14] Kharina GV, Kuznetsov MV, Kochergin VP. Mechanism and kinetics of anodic dissolution of aluminum and its alloys with zinc and rare-earths in a sodium polyvanadate solution. Russ. J. Electrochem. 1998;34:482-5.

[15] Vyazovikina NV. The effect of scandium on the corrosion resistance of aluminum and its alloys in 3% NaCl solution. Prot. Met. 1999;35:448-53.

[16] Ahmad Z, Aleem BJA. Effect of nano Al (Scx−1Zrx) precipitates on the mechanical and corrosion behavior of Al-2.5 Mg alloys. Mater. Corros. 2011;62:335-45.

[17] Szklarska-Smialowska Z. Pitting corrosion of aluminum. Corrosion Science. 1999;41:1743-67.

[18] Birbilis N, Buchheit RG. Electrochemical Characteristics of Intermetallic Phases in Aluminum Alloys. J. Electrochem. Soc. 2005;152:B140.

[19] Chemin A, Marques D, Bisanha L, Motheo AdJ, Bose Filho WW, Ruchert COF. Influence of Al7Cu2Fe intermetallic particles on the localized corrosion of high strength aluminum alloys. Mater. Des. 2014;53:118-23.

[20] Birbilis N, Cavanaugh MK, Buchheit RG. Electrochemical behavior and localized corrosion associated with Al7Cu2Fe particles in aluminum alloy 7075-T651. Corros. Sci. 2006;48:4202-15.

[21] Aballe A, Bethencourt M, Botana FJ, Cano MJ, Marcos M. Localized alkaline corrosion of alloy AA5083 in neutral 3.5% NaCl solution. Corros. Sci. 2001;43:1657-74.

[22] Park JO, Paik CH, Huang YH, Alkire RC. Influence of Fe-Rich Intermetallic Inclusions on Pit Initiation on Aluminum Alloys in Aerated NaCl. J. Electrochem. Soc. 1999;146:517-23.

[23] Nisacioglu K. Electrochemical Behavior of Aluminum-Base Intermetallics Containing Iron. J. Electrochem. Soc. 1990;137:69-77.

[24] Ambat R, Davenport AJ, Scamans GM, Afseth A. Effect of iron-containing intermetallic particles on the corrosion behaviour of aluminium. Corros. Sci. 2006;48:3455-71.

[25] Ezuber H, El-Houd A, El-Shawesh F. A study on the corrosion behavior of aluminum alloys in seawater. Mater. Des. 2008;29:801-5.

[26] Smialowska ZS. Pitting Corrosion of Metals. National Association of Corrosion Engineers; Houston. 1986, p.3.

[27] Grilli R, Baker MA, Castle JE, Dunn B, Watts JF. Localized corrosion of a 2219 aluminium alloy exposed to a 3.5% NaCl solution. Corros. Sci. 2010;52:2855-66.

[28] Zhu D, van Ooij WJ. Corrosion protection of AA 2024-T3 by bis-[3-(triethoxysilyl)propyl]tetrasulfide in neutral sodium chloride solution. Part 1: corrosion of AA 2024-T3. Corros. Sci. 2003;45:2163-75.

[29] Hans-Henning S. Mechanisms of Pitting Corrosion. Corrosion Mechanisms in Theory and Practice: CRC Press; 2002. p. 243-85.

[30] Li HT, Wang Y, Fan Z. Mechanisms of enhanced heterogeneous nucleation during solidification in binary Al–Mg alloys. Acta Mater. 2012;60:1528-37.

[31] Buchheit RG, Grant RP, Hlava PF, McKenzie B, Zender GL. Local dissolution phenomena associated with S phase (Al2CuMg) particles in aluminum alloy 2024-T3. J. Electrochem. Soc. 1997;144:2621.

[32] Shao M, Fu Y, Hu R, Lin C. A study on pitting corrosion of aluminum alloy 2024-T3 by scanning microreference electrode technique. Mater. Sci. Eng. A. 2003;344:323-7.

[33] Vyazovikina NV. The Effect of Scandium on the Corrosion Resistance of Aluminum and its Alloys in 3% NaCl Solution. Prot. Met. 1999;35 448-53.

[34] Marquis EA, Seidman DN. Nanoscale structural evolution of Al3Sc precipitates in Al(Sc) alloys. Acta Mater. 2001;49:1909-19.

[35] Frankel GS. On the Pitting Resistance of Sputter-Deposited Aluminum Alloys. J. Electrochem. Soc. 1993;140:2192.

CHAPTER 7: FINAL CONCLUSIONS AND FUTURE WORK

Chapter 7: Final Conclusions and Future Work

7.1 Final Conclusions

The Al–Sc and Al–Mg-Sc alloys with microalloying additions of Yb were investigated. The effects of substituting Yb for Sc on the microstructure and on the mechanical properties of Al–Sc alloy were studied by using SEM, TEM, HRTEM and Vickers hardness. The ageing behaviour, precipitate morphologies, precipitate coarsening and precipitation hardening of these alloys were investigated. The grain refinement in Al–Mg–Sc alloys with and without ultrasonic treatment at various pouring temperatures and the corrosion behaviour in 3.5 wt% of NaCl solution were also investigated.

The results showed the similarities of microstructure, hardness and aging behaviour of Al–0.24Sc–0.07Yb and Al–4Mg–0.24Sc–0.06Yb alloys in comparison with Al–0.28Sc and Al–4Mg–0.3Sc alloys were shown in this investigation, respectively. The hardness values of both alloys aged without homogenization treatment are significantly higher than those of alloys aged after homogenization treatment. The approximately spheroidal Al_3Sc and $Al_3(Sc,Yb)$ precipitates were uniformly distributed throughout the α–Al matrix. The precipitates remain fully coherent with α–Al matrix even after aging at high temperature for long time. The maximum hardness was achieved at a precipitate diameter around 4–6 nm. The hardness sharply decreases when the average diameter of precipitate is above 12 nm. The hardness of Al–4Mg–0.3Sc and Al–4Mg–0.24Sc–0.06Yb alloys were significantly higher than that of Al–0.28Sc and Al–0.24Sc–0.07Yb alloys at the same aging condition due to the solid solution strengthening of Al–Mg.

Mg, Sc and the pouring temperature have strong effect on the microstructure of Al–Mg–Sc alloy. The average grain size of Al–Mg alloy remarkably decreases from 439 ± 21 to 95 ± 2 μm when the content of Mg increases from 1 to 4 wt% at the pouring temperature of 700 °C. The average grain size of Al–1Mg sharply decreases from 439 ± 21 μm to 103 ± 2 μm by adding 0.3 wt% of Sc. Lower pouring temperature leads to smaller grain size and more homogeneous microstructure. Ultrasonic vibration proved to be a potential grain refinement technique for Al–1Mg–0.3Sc. Significant grain refinement was obtained by applying ultrasonic treatment within the temperature range of 700-740 °C. This fact makes more flexible to determine the pouring temperature in the foundry practice of this kind of alloy. The best grain refinement and uniform grain size are obtained by ultrasonic treatment at 720 °C

Regarding the corrosion behaviour of Al–0.28Sc and Al–0.24Sc–0.07Yb alloys in 3.5 wt% of NaCl solution, the evolution the OCP with time showed the lowest tendency to corrosion in Al–0.24Sc–0.07Yb heat treated alloy. The presence of Fe–containing intermetallic phases in these alloy promote the pitting corrosion. Yb has strong effect on the polarization behaviour of Al–Sc alloys. The addition of Yb decreases the

corrosion tendency and improves the pitting corrosion resistance of this alloy. The presence of a high number density of fully coherent nano–sized Al_3Sc or $Al_3(Sc,Yb)$ precipitates in heat treated alloy enhances the passivity of these alloys.

The immersion and potentiodynamic polarisation properties of Al–4Mg, Al–4Mg–0.3Sc and Al–4Mg–0.24Sc–0.06Yb alloys were also shown in this study. The addition of Sc and Yb to Al–4Mg alloy reduced the size and changed the morphology of impurity intermetallic particles. The Fe–containing intermetallic particles are cathodic with respect to the matrix and can act as pitting initiation sites. The high content of Mg makes the Fe–containing intermetallic particle less noble to the matrix. Yb–containing intermetallic particles did not cause any dissolution of the matrix at the periphery of these particles. The addition of Sc and Yb can decrease the tendency to corrosion of the heat treated Al–4Mg–0.3Sc and Al–4Mg–0.24Sc–0.06Yb alloys. The active dissolution and pitting are dominant corrosion mechanisms in Al–4Mg alloy. While the polarization curves of Al–4Mg–0.3Sc and Al–4Mg–0.24Sc–0.06Yb alloys showed the spontaneous passivation followed by pitting corrosion. More stable passive plateau and less susceptibility to pitting corrosion was observed in the polarization curves of Al–4Mg–0.3Sc and Al–4Mg–0.24Sc–0.06Yb alloys after heat treatment.

7.2 Future work

- This thesis research can be continued to fully understand the precipitate coarsening, precipitation hardening and its mechanism in Al–Sc and Al–Mg–Sc alloys with microalloying additions of Yb. In combination with modeling, the formation of precipitates in these alloys can be simulated.
- To fully understand the grain refinement mechanism by ultrasonic treatment, the size and distribution of cavitation should be investigated with various ultrasonic frequency, power, acoustic radiator position and shape, treatment time, the dynamic of cavitation (bubble growth and collapse), the dynamic interaction between cavitation and the melt during solidification can be studied. Modelling of these processes using the finite element commercial software should be performed.
- The corrosion behaviour of Al–Mg–Sc alloys after ultrasonic treatment can be investigated to clarify the idea about the improvement of corrosion resistance of Al–Mg–Sc alloys by applying ultrasonic treatment.